Stony Brook University

Strategies for Quantitative Neuroimaging with the Rat Conscious Animal PET (RatCAP)

A Dissertation Presented
by

Sudeepti Southekal

to

The Graduate School
in Partial Fulfillment of the
Requirements
for the degree of

Doctor of Philosophy
in

Biomedical Engineering
(Medical Physics)

Stony Brook University

December 2009

Stony Brook University

The Graduate School

Sudeepti Southekal

We, the dissertation committee for the above candidate for the

Doctor of Philosophy degree, hereby recommend

acceptance of this dissertation.

Dr. Paul Vaska – Dissertation Advisor

Scientist, Brookhaven National Laboratory and Asst. Prof. of the BME program

Dr. Gene Gindi – Chairperson of the defense

Assoc. Prof, Departments of Radiology and Electrical Engineering

Dr. David Schlyer – Asst. Prof. of the BME program

Dr. Craig Woody – Senior Physicist, Brookhaven National Laboratory

This dissertation is accepted by the Graduate School.

Lawrence Martin

Dean of the Graduate School

Abstract of the Dissertation

Strategies for Quantitative Neuroimaging with the Rat Conscious Animal PET (RatCAP)

by

Sudeepti Southekal

Doctor of Philosophy
in

Biomedical Engineering
(Medical Physics)

Stony Brook University
2009

Introduction: The strength of small animal Positron Emission Tomography (PET) systems lies in their ability to quantify the physiological status of minute structures in vivo from a sequence of dynamic images. The Rat Conscious Animal PET (RatCAP) is a novel preclinical system developed at Brookhaven National Laboratory to eliminate the confounding effects of anesthesia in rat brain studies by miniaturization and direct attachment of the tomograph to the head of the awake rat. The goal of this dissertation is to explore and evaluate optimized image processing techniques in an effort to realize the full potential of quantitative neuroreceptor imaging with the RatCAP.

Methods: The basis of the RatCAP image reconstruction approach is the Monte Carlo-simulated system response model which faithfully reproduces measured data from the tomograph. The model, with known factors that degrade PET image quality incorporated into it, is used to simulate the probability matrix for iterative reconstruction. This results in images that are corrected for possible reconstruction errors due to system design, positron and photon physics and statistical variability in the data. Additional improvements are realized by corrections for random coincidences and detector efficiency variations integrated into the iterative reconstruction framework.

Validation: The complete RatCAP data processing chain from the design of acquisition protocols to the analysis of imaging results is presented in this work. Phantom studies with known activity distributions have been used to evaluate the image noise variance and bias at each step. Results from dynamic animal studies confirm the feasibility of our approach for standard PET imaging tasks. Finally, some strategies for potential future optimizations are suggested.

Results: The RatCAP reconstructed image resolution is 1.2 mm at the center and under 2 mm throughout the field-of-view. Imaging results show a contrast recovery of >0.9 for hot as well as cold structures. The overall performance of the RatCAP has been shown to be comparable with other preclinical PET systems of its generation, while imaging the subject awake and enabling correlations with behavioral measures for the first time in rat models.

Dedicated to my grandparents, the only people to think I can do no wrong.

Table of contents

List of Figures

List of Tables

Acknowledgments

This dissertation[†] is a tribute to the PET group at BNL, especially the current and former members of the RatCAP team. It has been an honor to contribute towards the successful realization of your PET project! In particular, I wish to express my gratitude to:
Dr. David Schlyer, for introducing me to life in Academia. For discussions about everything from radiotracer kinetics and nanoparticles to refueling airplanes in Alaska and the smell of durian - BNL would be so dull without you!
Dr. Martin Purschke for being a constant source of solutions and support. And for reminding me, with each conversation, how much I have yet to learn about life, science and programming.
Dr. Craig Woody for influencing, then supporting my decision to get a Ph.D. I know I will be grateful for many years to come!
Dr. Jean-François Pratte for your patience in the early days, your belief and encouragement.
Dr. Coco (Sara) Gómez-García for your infinite wisdom and infectious exuberance.
Dr. Sachin Junnarkar for being my go-to guy for electronics questions, Dr. Daniela Schulz and the cNLHs for girl power hours!, Sean Stoll for always being ready to lend a cheerful hand, Dr. Sang-June Park for saying all the right things to curb my impostor syndrome, Dr. Michael Schueller for introducing me to Kaliedagraph. Aarti, Srilalan, Sri Harsha, Do-Hyun and Bosky for being my punching bags and/or providing comic relief. The chemists, postdocs, students and interns who livened up sushi days, happy hours, and even just the typical day at the lab.

Dr. Michael Hadjiagyrou for being the best classroom teacher (and always remembering my name!). Drs. Joanna Fowler and Clint Rubin for being inspiring role models.

Dr. Jorge Chan for creating Cecelia[‡].

I am also extremely grateful for the support of my family and friends, especially my sister, Sahana and brother-in-law, Dr. VJ. Not only for providing me with a comfortable, stress free environment while I wrote this dissertation, but also your encouragement throughout. Thank you Vivek, for allowing me to lean heavily on you every day, all these years. Special thanks are also due to my Stony Brook support system; Varsha, Sameer and Tanuj. And Liv, Sarah, Godfrey, Tejas and Jeremy for fun times! A big thank you to my parents Aroona and Suresh Southekal who patiently, albeit solicitously, stuck by my decision to stay in grad school!

Finally, I emphasize the role of Dr. Paul Vaska in shaping my scientific personality. Thank you for initially taking the time to instill in me your intellectual discipline, and later finding the right balance between leadership and compassion. For pushing for perfection but sometimes pardoning a little less. For hours spent brainstorming at my computer that gave me my new approach to problem-solving (which begins trying to guess how you would tackle it!). For allowing me the luxury of almost blind confidence in your word. I hope you continue to be a source of inspiration and intelligent advice to many researchers, as you have been for all of us. And since the ideas in this work are mostly yours, I hope the outcome has made you proud.

[†] Supported by US Department of Energy (OBER) under Prime Contract No. DE-AC02-98CH10886.

[‡] www.phdcomics.com.

1. Overview

Motivation

A debatable practice in preclinical Positron Emission Tomography (PET) imaging studies is the requirement for anesthesia to prevent animal discomfort and motion. Since PET is a functional technique, anesthesia is considered to be a possible limiting factor [2-4] because it could confound the interpretation of these studies, particularly in the case of the brain. Scientists have explored the use of physical restraints [5, 6] instead of anesthesia, but this approach could cause high levels of stress in the animals and defeat the purpose of the study. The concept of a PET imaging system designed specifically to image the awake animal was developed at Brookhaven National Laboratory (BNL) in 2001. This wearable system, named Rat Conscious Animal PET (RatCAP) [7-10] is a miniaturized, fully 3D PET scanner that is attached to the head of the rat prior to imaging (see Figure 1). A support system has been designed to counterbalance the weight of the tomograph and allow full freedom of motion for the rat during the study. Two prototypes of the system have been successfully used to image the awake animal with little prior conditioning, without a significant increase in stress levels [11]. Thus, this one-of-a-kind tomograph could open up new possibilities including imaging of the rat brain during normal and induced behavior, and is potentially a valuable tool in preclinical neuroimaging.

This dissertation details the optimization of specialized data and image processing methods to realize the full potential of quantitative neuroreceptor imaging with the RatCAP. The small size of the system presents a unique set of advantages as well as challenges for conventional image generation approaches, and a combination of established techniques and novel methods developed specifically for the RatCAP have been implemented.

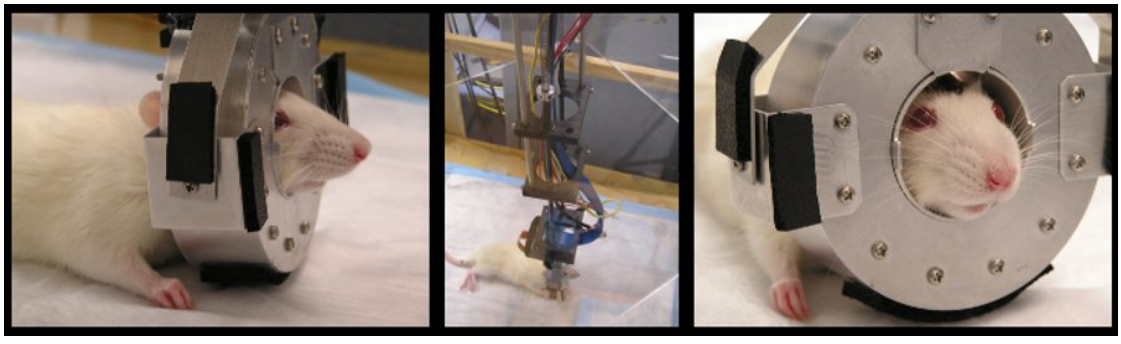

Figure 1 Imaging the awake animal with the RatCAP

Contributions of this dissertation

The RatCAP is a collaborative effort by an interdisciplinary team of scientists from BNL, NY, University of Sherbrooke, QC, Canada and Stonybrook University, NY. The design, testing and validation of the detectors and individual modules (readout chip, signal processing board, data acquisition circuits) was carried out by scientists from the Instrumentation and Physics divisions at BNL. System performance simulations and proof-of-principle reconstruction algorithms were reported in a separate dissertation [12]. The contributions of this dissertation involve system optimization, calibration, data processing and performance measurements for the first working prototype of the RatCAP and all subsequent versions. The image reconstruction approach, enhanced by corrections for factors that degrade the quantitative capability of PET systems, has been optimized, evaluated and standardized for imaging tasks associated with the RatCAP. Using a validated tomograph, image acquisition protocols have been designed for these tasks and the resulting images are presented in this work.

Dissertation outline

This manuscript begins with an introduction to the principles and practices of PET imaging. The remaining topics have been broadly divided into three overall ideas:

1. Pre-reconstruction data processing
2. Image reconstruction
3. Quantitative corrections for physical effects

Section 2 contains a concise literature review for each of the three ideas and Section 3 discusses our efforts to implement and validate some of these techniques for the RatCAP. New ideas devised specifically for the RatCAP are also highlighted in Section 3.

Standard system performance measures such as sensitivity, count rate performance and spatial resolution are reported in Section 4, and a comparison with existing preclinical PET systems is presented to evaluate our approach. The latter part of Section 4 presents a selection of recent imaging results using the current RatCAP prototype and a variety of radiotracers. Section 5 includes a discussion that summarizes the lessons learned from our efforts to maximize the quantitative accuracy of the tomograph in realistic imaging situations. This dissertation is concluded at the end of Section 5 with some recommendations for future optimizations.

2. Quantitative PET Imaging

2.1 Introduction to PET (Positron Emission Tomography)

Positron Emission Tomography (PET) is a nuclear medicine imaging technique to produce a three-dimensional map of functional processes in the body. This functional capability differentiates it from, and supplements, other imaging modalities that mostly provide anatomical information such as Computed Tomography (CT) or Magnetic Resonance Imaging (MRI). A PET study begins with the injection of a trace amount of positron-emitting radionuclide tagged to a biologically relevant molecule into the bloodstream of the subject. A common example is the labeling of glucose analog FDG (2-fluoro-2-deoxy-D-glucose) with the radioactive isotope ^{18}F. As glucose uptake takes place in the body, PET maps the radioactivity distribution, thus providing insight into the functional processes occurring in vivo.

The physics of the process is depicted in Figure 2. The radionuclide undergoes beta decay to produce positrons which disperse their kinetic energy as they traverse through the body. Eventually, they annihilate with electrons and the combined rest energies are emitted in the form of two 511 keV photons traveling in opposite directions. These back-to-back photons are registered by detectors placed around the subject. If both photons are detected within a short time window determined by the time resolution of the system, the event is recorded as a "coincidence". The annihilation event is then assumed to have occurred along the line or tube connecting the two detectors. Advanced mathematical algorithms are used to estimate the locations of these events for all coincidences detected to produce a reconstructed image of the source distribution.

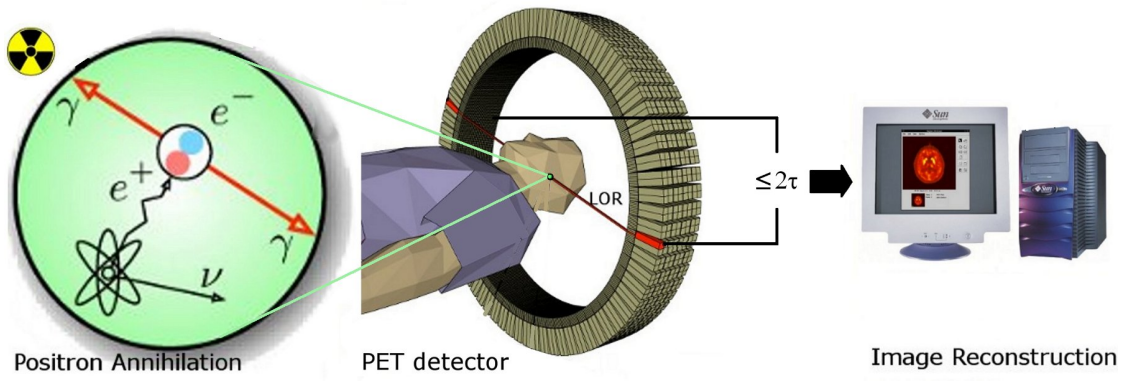

Figure 2 PET schematic
Image modified with permission from original work by Jens Langner [13]

Radioactive isotopes used in PET typically have short half lives (for example, ^{18}F, ^{11}C, ^{15}O, ^{13}N) and they are incorporated into useful compounds such as water, glucose, ammonia or other molecules that bind to receptors or transporters at active sites. Functional parameters (such as the metabolic rate of glucose) are obtained by analyzing the localization of these tracers from a time sequence of images. This ability to quantify physiological activity has earned PET widespread clinical acceptance in the last two decades and the technique has recently made significant inroads into the field of preclinical imaging.

Analysis of functional data

The functional capability of PET studies is enhanced by plotting time vs. activity curves for selected regions (or volumes) of interest as shown in Figure 3. The curve shows that following bolus injection of ^{11}C-Raclopride, the radiotracer enters tissue from arterial blood. When the concentration in blood falls below tissue levels, the tracer begins to clear from the tissue. The two brain tissue regions selected in this curve are the striatum and cerebellum, known to have high and low concentrations of binding sites respectively. Since the presence of a binding site prolongs the retention of the tracer, binding potential is characterized by a ratio of concentrations in these two regions of interest (ROIs). This time-activity curve can be fitted with a kinetic model [14] from which functional parameters can be estimated. Thus, precise interpretation of PET data requires a high degree of accuracy in the estimated image counts within an ROI.

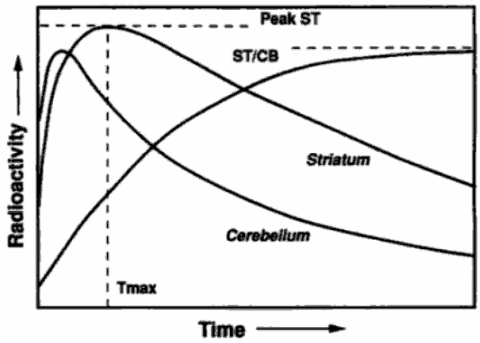

Figure 3 PET data analysis – Typical time-activity curve

Generic curve from [15] showing two regions of interest, the striatum (ST, specific binding) and cerebellum (CB, non-specific binding) varying over time in a ^{11}C-Raclopride study. The binding potential of ^{11}C-Raclopride in this study is calculated from the value of the flat portion of the ST/CB curve when the system is assumed to have reached steady state.

Early history

The idea of Positron Emission Tomography (PET) was born from the discovery of positrons, and subsequently the annihilation reaction, by Anderson [16] in 1932. Positron imaging was first applied in the clinic using opposing single-crystal detectors in 1951 [17]. During the 1960s, spurred by the popularization of artificial (cyclotron-produced)

radioactivity, Brownell and group at Massachusetts General Hospital (MGH) developed multi-crystal arrays [18] which led to the development of the MGH Positron Camera (PC) [19] and its rotating version, PC II [20] which used two banks of 127 Sodium Iodide detectors read out with 72 photomultiplier tubes. Another noteworthy positron imaging system from the 60s was the BNL "head shrinker" [21], known as the first PET ring detector, which consisted of 32 detectors placed around the head of the subject. Positron imaging, however, did not find an immediate application in the clinic, and it was the invention of tomographic reconstruction methods [22] in the 70s that prompted a new era of developments and varied applications for the technology. In the 21st century, further advances in mathematics and computing power as well as detector technology have enabled the evolution of these systems to a point where structures less than 2mm in size can be accurately resolved. While these newer developments will be discussed in greater detail in the relevant sections of this dissertation, this section calls for a comparison of images from then and now to emphasize how far the field has come within a short period of time. Figure 4 compares a few standard PET studies published in the 1970s to similar studies published more recently. While the goals of PET imaging remain largely the same, the approaches towards optimizing the procedures have taken a giant leap forward over the last few years.

Section overview

This section begins with an introduction to the physics of PET and a discussion of probable errors in the idealized PET system described above. Next, the basic components of a PET system will be discussed, keeping in mind requirements to minimize the aforementioned errors. To conclude, the current state-of-art in small animal PET imaging will be presented, and the use of Monte Carlo techniques to simulate PET prototypes will be discussed.

2.1.1 Event types and system requirements

The distribution of the positron decays in the body can be recovered from coincident events detected within the time window by reconstructing them along a line of response (LOR) or tube of response (TOR) that connects the detectors. This "electronic collimation" works under the assumption that single events measured within a time window arise from the same annihilation event and that the annihilation occurs somewhere along the LOR. In reality, however, the estimate of coincidences detected within the window could be corrupted due to certain aspects of the physics of photon interactions in tissue discussed below. Approaches to correct for these effects will be detailed in Section 2.4.

A. Uncertainty in positron decay location

As the positron traverses through matter it loses energy in a series of ionization or inelastic scattering events along a tortuous path before eventually annihilating with an electron. Thus, the location of the annihilation event is not exactly the same as the location of the decay, causing a slight blurring in the spatial resolution of the system. Due to the large

number of seemingly arbitrary interactions, it is difficult to estimate [23] this "**positron range**" based on the positron energy alone, and empirical measurements are made [24] to determine its effect in specific materials.

When the positron and electron finally interact, two photons are produced with energies equivalent to the rest-mass of the positron-electron pair. PET relies on the fact that these two photons are emitted 180° apart, but due to non-zero momentum when the annihilation occurs, this is not strictly true. Photon **noncolinearity** contributes an additional uncertainty to the localization of the decay.

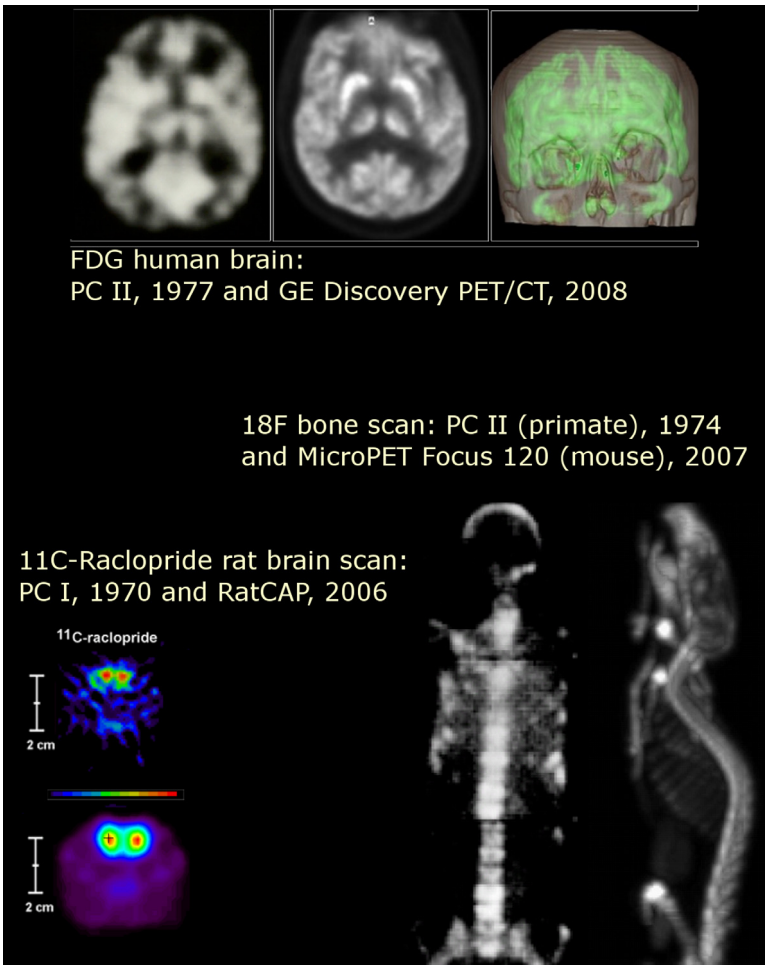

Figure 4 PET Imaging - Then and now

(top) Imaging glucose metabolism in the human brain using the Positron Camera (PC) II and the GE Discovery PET/CT (www.gehealthcare.com).

(bottom, left) Imaging of dopamine receptors in the rat striatum, showing a significant improvement in signal to noise in 2006 compared to 1970.

(bottom, right) Comparison of 18F-Fluoride bone scans in a primate (PC II) and a mouse (microPET Focus 120, [25]. Even though the structures in the mouse skeleton are 10 times smaller, they are resolved more accurately.

Sources of PC I and PC II images: "A history of PET imaging", Brownell, 1999.

Positron range and noncolinearity present practical limits to the spatial resolution that can be achieved in PET and their contributions will be discussed in the context of spatial resolution later in the section.

B. Photon interactions in tissue

At energies of 511 keV, the principle mechanism of photon interaction with tissue is **Compton scatter**. Photoelectric absorption is more relevant at lower energies (for e.g. 80 keV X-ray systems), and pair production takes place at energies > 1MeV. Scatter occurs when the photon interacts with a loosely-bound orbital electron in the material through which it traverses, resulting in an increase in the kinetic energy of the recoil electron and a change in the direction of the photon. The loss of photon energy is given by the formulation in Equation (1) below, obtained from [26]:

$$E' = \frac{E}{1 + (\frac{E}{m_0 c^2})(1 - \cos\theta)} \qquad (1)$$

where m_0c^2 is the rest mass of the electron, E is the incident energy of the photon and θ is the scattering angle. Thus, a large deflection can be caused with a relatively small loss in energy, resulting in the positioning of the coincidence along an incorrect LOR if strict energy discrimination is not applied.

A contrasting effect is the **attenuation** of photons due to absorption by tissue. Apart from the energy of the incident photon, its attenuation depends on the atomic number, Z (or density, ϱ) and the thickness of the tissue (ds) encountered along its path, s. Mathematically, the magnitude of photon attenuation can be expressed by $A = A_0 * \exp(-\int\mu(x,y)ds)$ where A_0 and A are the incident and transmitted photon fluences per unit area and μ is the linear attenuation coefficient, which represents the probability that the photon will undergo an interaction while passing through unit thickness of the tissue.

$$P_{\text{detection}} = e^{-\mu(d1-a)} \cdot e^{-\mu(a-d2)} = e^{-\mu(d1-d2)} = e^{-\mu L} \qquad (2)$$

The probabilities that the two photons from annihilation location a between the detectors d1 and d2 with an LOR length of L will reach the detectors in an attenuating medium, ignoring all other effects, is calculated in Equation (2). Hence, photon attenuation causes an underestimation of true coincidences independent of the location of the decay along the LOR but related to its length.

C. Types of coincident events

The types of events likely to be registered within the coincidence window ±τ are listed below and illustrated in Figure 5. For the remainder of this manuscript, all coincidences

including contaminations detected within the coincidence window will be referred to as the "prompt" coincidences, abbreviated as P. P includes the following:

True coincidences (T) are obtained in the ideal scenario described above, when two unscattered, unattenuated photons originating from the same decay are detected at an acceptable energy within the coincidence resolving time of the circuitry.

Random coincidences (R) are registered when photons from two separate decays happen to be detected within the selected time window for the system. These events are spatially uncorrelated with the distribution of the source and add a relatively uniform background to the image, suppressing contrast and hence affecting quantitation. Random coincidences have a higher probability at high data rates and are given by the formula:

$$r_{ij} = 2\tau s_i s_j \qquad (3)$$

where 2τ is the timing window for the system, typically set to twice the time resolution τ at full width at half maximum (FWHM), r is the rate of random coincidences observed in the line of response connecting detectors i and j, and s_i and s_j are the singles rates at those two detectors. Provided the system dead time is small, this means that the randoms will change roughly in proportion to the square of the activity concentration.

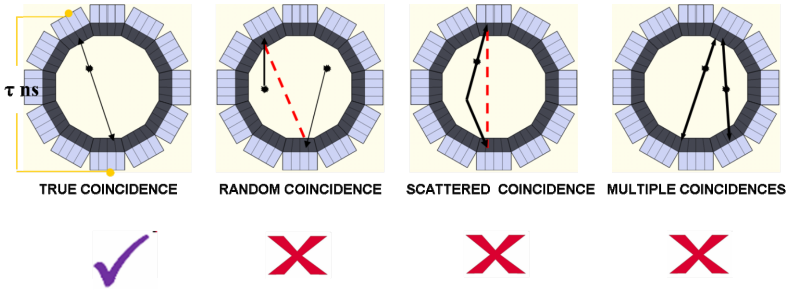

Figure 5 Coincident event types in PET

A **scattered coincidence** (S) is one in which at least one of the detected photons has undergone one or more Compton scattering events prior to being detected. As mentioned earlier, the coincidence is assigned to an incorrect LOR, adding a position-dependent background, decreasing contrast and adding statistical noise. The fraction of scattered events depends on the volume and material of the object being imaged and the geometry of the camera. In some cases, radioactive regions that are outside the field-of-view (FOV) of the tomograph such as other organs, the gantry of the tomograph, or even the patient bed could contribute scattered coincidences.

Multiple coincidences occur when three or more single events are detected within the time window. Due to the ambiguity in deciding which combination of photons is valid, they are typically disregarded. Multiple coincidences, too, are more likely at high rates.

Classic examples of some of the effects discussed above are shown in Figure 7 and Figure 6.

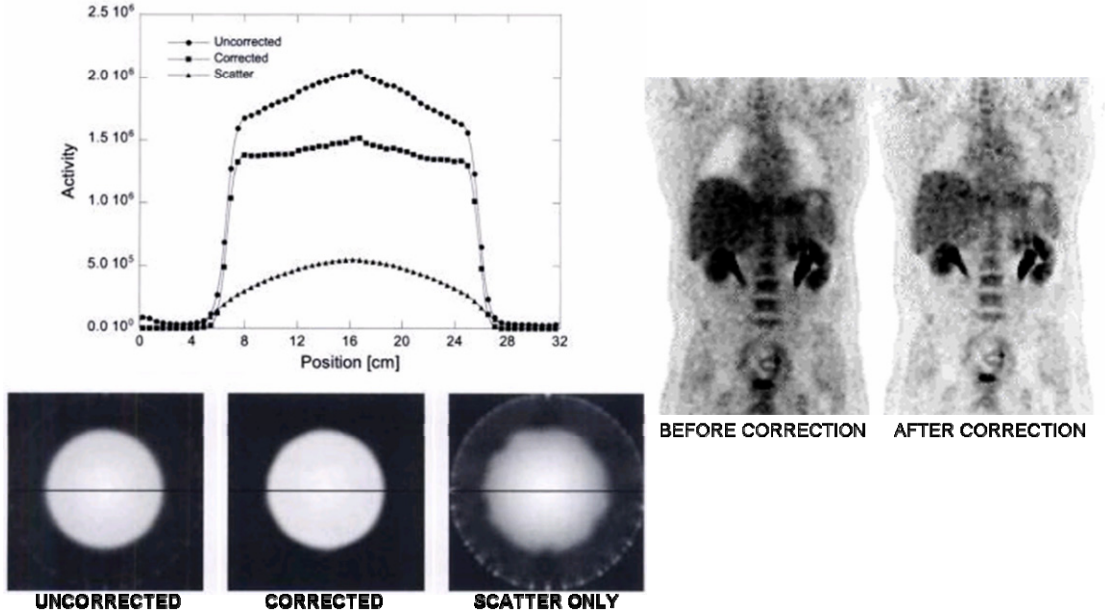

Figure 6 Effect of Scatter correction

(left) Phantom data: Uniform cylindrical phantom shows expected flat profile after correction. Obtained from [27]

(right) Clinical FDG study: Contrast improves after scatter correction to allow lesions, especially in the prostate, to be more clearly visible. Obtained [28]

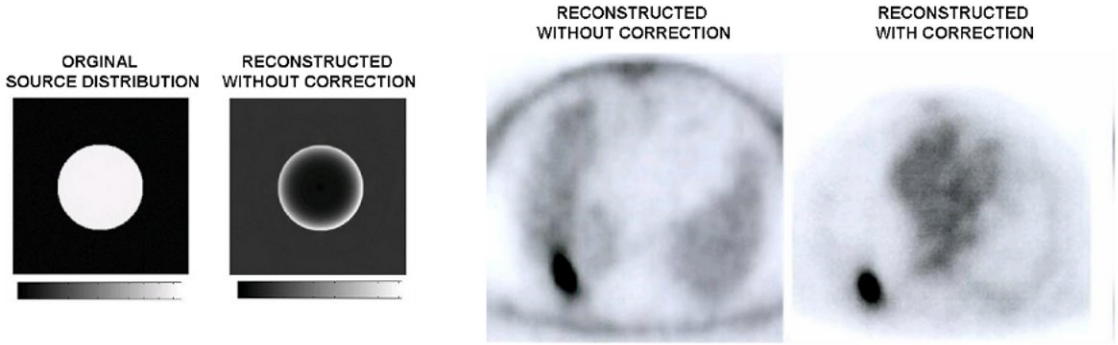

Figure 7 Need for attenuation correction

(left) Simulated data: Uniform cylindrical phantom showing loss of uniformity due to attenuation.

(right) Clinical study showing a slice of the lung with a distortion in lesion size without correction. Also note that skin has more uptake than muscle. Obtained from [29]

D. Signal-to-noise considerations

Taking the above effects into account, Strother [30] derived a figure-of-merit to represent the signal-to-noise ratio (SNR) of a PET system. It is termed the Noise Equivalent Count Rate (NECR) and defined as the count rate which would have resulted in the same SNR in the data in the absence of additive noise (scatter and randoms). The derivation, which also accounts for increased noise due to correction methods, is reproduced below.

Since PET is based on radioactive decay, the detected counts are governed by a Poisson distribution. The counts in each LOR can be modeled as independent random variables with the mean equal to the number of decays along the LOR. Since the variance of the Poisson variable is equal to its mean, if P (or T or R or S) has n counts, its signal-to-noise ratio (SNR) is $n/\sqrt{n}$. To calculate the count rate which would be obtained if there was no error in the trues, the error in the trues (ΔT) is represented as the quadrature sum of the (Poisson) errors $\sqrt{P}$, $\sqrt{R}$ and $\sqrt{S}$ in Equation (4) below.

$$\begin{aligned} & P = T + R + S \quad or \quad T = P - R - S \\ & \Rightarrow \Delta T = \sqrt{(\Delta P)^2 + (\Delta R)^2 + (\Delta S)^2} \\ & \Rightarrow \Delta T^2 = P + k_R f_{fov} R + S = T + (1 + k f_{fov}) R + S \end{aligned} \qquad (4)$$

The factors k and f_{fov} are factors that influence the noise in the random coincidence estimate used for correction and will be discussed in Section **0**. This formulation assumes no additional variance contributed by the scatter estimation method, which is feasible using certain scatter correction approaches [31, 32].

NEC is the count rate at which the signal-to-noise is the same as that which would be obtained without additive noise, and ΔNEC is $\sqrt{NEC}$. Therefore,

$$\frac{NEC}{\sqrt{NEC}} = \frac{T}{\Delta T} \Rightarrow NEC = \frac{T^2}{\Delta T^2}$$

$$NEC = \frac{T^2}{T + (1 + k f_{fov}) R + S} \qquad (5)$$

If R = 0 and S = 0, the NECR is equivalent to the measured trues rate. The NEC is a useful figure of merit to compare the noise performance of dissimilar systems for standard objects and injected doses.

E. PET System Design Requirements

In the light of the issues discussed above, an ideal PET detector system can be described as having the following characteristics:

- High time resolution, allowing the use of a smaller coincidence acceptance window to minimize random coincidences.
- High energy resolution, for maximum scatter rejection.

- High sensitivity to maximize signal-to-noise ratio with low injected doses.
- High spatial resolution to resolve small structures and differentiate closely-spaced ones.
- Equal photon detection efficiency for all detectors.
- Low system dead time for unaffected performance at high count rates.

Meeting the above requirements aids accurate quantitation, thus simplifying PET image analysis.

2.1.2 Components of a PET system

Although the design of a PET detector is not the focus of this work, design choices influence the eventual image output. With this in mind, a brief overview of the key options available for PET detectors and most commonly implemented readout strategies are presented here. Apart from a few novel geometries [33], PET scanners today are composed of radiation detectors arranged in the form of multiple stacked rings, or a block detector arrangement which forms stacked polygonal rings. These systems can be designed to operate in 2D, with axial septa along the ring boundaries to allow only parallel LORs, or 3D with larger axial acceptance angles. 3D imaging allows higher sensitivity; however, this increase in sensitivity also translates to background events.

A. Radiation detectors

The purpose of a radiation detector is to measure the energy deposited by a photon and convert it into an electrical signal. If this energy is deposited in a photoelectric reaction, the photoelectron carries all the energy deposited, resulting in the largest possible signal shown by the photopeak in the energy spectrum of Figure 8. Another possibility is Compton scatter, followed by the possible escape of the scattered photon from the detector volume. This leads to a Compton background up to the maximum possible energy transfer in Equation (1), resulting in the characteristic Compton edge in the energy spectrum. Each photon can interact multiple times, and the integral of the signals detected for each event is proportional to the total energy deposited. This total energy is used to discriminate against photons that have scattered in the object.

There are three types of radiation detectors used in PET, of which scintillation detectors are by far the most common. The other two types are proportional gas chambers [34], inherited from high energy physics applications and solid state detectors like Cadmium zinc telluride (CdZnTe or CZT) which have recently been produced for practical applications [35]. Scintillation detectors, which will be the focus of the remainder of this section, are indirect detectors which convert gamma photons into visible (or UV) light photons, and need to be coupled to photodetectors to convert their output to an electrical signal. The ideal scintillator would have high stopping power (high attenuation coefficient) to maximize the probability of a photoelectric depositions, high light yield (increased counting statistics) for high spatial and energy resolution, a short decay time for high timing resolution and a high degree of homogeneity. A comparison of the properties of commonly used scintillators is in [36]. Until

recently, Bismuth Germanate (BGO) was the most popular scintillation detector used in PET systems due to its excellent stopping power compared to Sodium Iodide (NaI) although NaI provided better light yield. New scintillators such as Lutetium Oxyorthosilicate (LSO) and Gadolinium Oxyorthosilicate (GSO) have been shown to have the desired combination of high light output and high stopping power, along with improved timing, and have become extremely popular especially with small animal PET scanners [37-40]. Also worth mentioning are crystals such as Barium Fluoride (BaF_2) and Lanthanum Bromide ($LaBr_3$) with decay times close to the picosecond range which make them suitable for time-of-flight PET applications [41, 42]

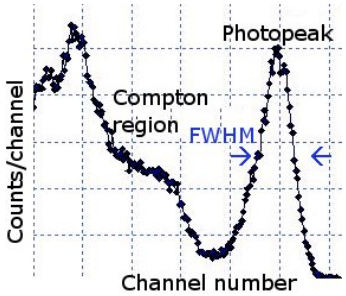

Figure 8 Typical photon energy spectrum measured by a scintillation detector

Photodetectors for these scintillation detectors are required to have high quantum efficiency (high ratio of primary electrons to incident photons) and fast readout (for good timing). Most existing systems use PhotoMultiplier Tubes (PMTs) or solid-state Avalanche PhotoDiodes (APDs), of which APDs have been known to be more efficient within a compact arrangement although they have inferior timing and are more prone to noise. APDs are preferred for high resolution applications [43, 44], but position-sensitive PMTs have also been used to achieve high resolution in addition to good timing [45, 46]. Recently, silicon photomultipliers [47] have shown promise with their superior noise properties and high timing resolution and are being touted as the perfect photodetector for PET applications.

B. Readout strategies

A detector block comprising a closely packed array of small discrete crystals individually coupled to photodetectors would provide the best spatial resolution for a PET system, limited only by the size of the individual detector elements. This is because there is no systematic inaccuracy in the positioning of the interaction since each individual crystal is processed in a separate channel. Small animal PET systems take advantage of the compact efficiency of APDs to implement such a one-to-one coupling scheme [7, 43, 44], but this may not be feasible for PET systems with thousands of detector elements. Another scheme as discussed above is to use crystals coupled to individual channels of a PS-PMT. Alternatively, crystals are grouped together in blocks, with each block coupled to PMT arrays with a lower encoding ratio. The relative light collected within a detector element provides positioning information, and the total light provides energy information. This idea is driven mainly by

cost and practicality, but spatial resolution is compromised. Novel strategies include the use of fiber optic bundles [25] and light guides [48, 49] to transfer light to photodetectors placed further away to maintain the one-to-one encoding without the reduction in packing fraction caused by bulky detectors.

C. Signal processing electronics

Standard electronics provide amplification, shaping and baseline restoration functions prior to coincidence counting. The amplitude of the pulse for each event is proportional to the amount of energy deposited, and selective counting of pulses within an amplitude range is used to discriminate against low-energy (or high-energy) background events. The time of event arrival can be obtained using leading edge triggering, zero crossover timing or constant fraction timing methods that are more effective at reducing time walk [50], discretized using Time-to-Digital Converters (TDCs) or Analog-to-Digital Converters (ADCs). On-circuit logic controllers or offline algorithms are used for coincidence processing. The coincidence time window is selected based on the coincidence time resolution of the system.

D. Impact of detector design on sensitivity and spatial resolution

Sensitivity

Absolute sensitivity in PET is defined as the fraction of positron annihilation events detected as true coincident events. There are obvious benefits to maximizing sensitivity in a PET system; mainly the improvement of SNR leading to the detection of subtle signals in the presence of statistical noise due to limited injected doses. The event rate for the simultaneous detection of two unscattered annihilation photons can be parameterized by the following product [51]:

$$[\text{source activity} * \text{branching fraction}] * \text{geometric efficiency} * \text{object attenuation} * (\text{detector efficiency})^2 \quad (6)$$

The branching fraction is the fraction of positron decays in the radioactive isotope.

The geometric efficiency depends on the solid angle coverage of the detector ring and the packing fraction of the detector elements. Since the axial coverage of a system greatly influences solid angle for detection, sensitivity drops off dramatically as the source is moved away from the center of the FOV (cFOV) axially.

The intrinsic detector efficiency depends on the density and thickness of the detector material, which would determine the probability of photoelectric and Compton interactions.

Spatial Resolution

For structures larger than ~2 mm, spatial resolution in PET depends mainly on the size of the individual detector elements and the geometry of the tomograph. In order to resolve smaller structures, however, the effect of other factors becomes important as well.

Moses and Derenzo [52] have proposed the formula in Equation (7) to calculate the expected reconstructed image resolution at the cFOV of a general PET camera as the quadrature sum of the parameters detailed below:

$$FWHM = 1.25\sqrt{(\frac{d}{2})^2 + b^2 + (0.0022D)^2 + r^2} \qquad (7)$$

d is the size of the individual detector element.

b is the systematic inaccuracy of detector positioning, or encoding error for light sharing designs.

0.0022D is contribution of the positron noncolinearity component to the blurring for a point at the center of the tomograph with diameter D. This number has been determined from empirical measurements showing a Gaussian angular distribution of ~0.5° FWHM for the annihilation photons which translates to a maximum contribution of 0.0022D for a centrally-placed point.

r is the contribution of positron range to blurring. Unlike the other factors, the effect of positron range is shift invariant. It depends on the energy of the positron and properties of the material, which have been determined empirically for medically relevant emitters [53], or estimated using combined analytical calculations and simulations [23]. The consensus is that positron range follows a cusp-like distribution, consisting of a central spike of 0.5 mm FWHM plus tails that extend outward for many millimeters. The effective contribution r in water has been found to be as high as 6 mm for the high energy positrons of ^{82}Rb, but ≤1 mm for ^{18}F and ^{11}C, as shown in Table I. Similar contributions can be expected in tissue.

1.25 accounts for resolution degradation due to tomographic reconstruction.

While it would be straightforward using the formula above to calculate the expected resolution at cFOV, an additional factor to be considered for sources further away from the center is crystal penetration through the angled detectors in the ring geometry. This causes broadening of the LORs and position-dependent resolution degradation due to **parallax errors**. Depth-of-interaction resolving detectors [37, 44] and innovative phoswich designs [54] have used to reduce the impact of these errors. More discussions about these issues will be included in future sections.

Radionuclide	E_{max}	$Range_{mean}$ or 'r'	$Range_{max}$
^{18}F	0.633	0.6	2.4
^{11}C	0.959	1.1	4.1
^{15}O	1.738	2.5	7.3
^{82}Rb	3.4	5.9	14.1

Table I Max and mean positron range in water for commonly-used radionuclides in PET
Data obtained from [55]

Resolution/Sensitivity Tradeoff

Equations (6) and (7) can be used to explain the resolution-sensitivity tradeoff in Table II and will be discussed in detail in Section 2.3. The path towards high sensitivity in PET without compromising resolution is to design high efficiency detectors with depth-of-interaction (DOI) resolution. For the most part, degraded resolution can be recovered considerably using robust reconstruction algorithms that accurately model the blurring components of the system [56]. These will be discussed in detail in Section **2.3**. Stickel and Cherry [57] used Monte Carlo simulations and analytical calculations of blurring to characterize the limits on spatial resolution imposed by positron physics, photon interactions and detector materials. According to their paper, the ultimate intrinsic resolution achievable with current know-how is 0.5 mm using ^{18}F, by 250 μm detector elements placed 8 cm apart. To date, no system has achieved the fundamental spatial resolution potential inherent to PET [58]. The performance of some existing systems is discussed next.

Increase sensitivity by:	**Resolution suffers due to:**
Increasing solid angle coverage ▪ Reducing scanner diameter ▪ Operating in 3D mode	Parallax errors Scattered coincidences
Increasing crystal length	Parallax errors Reduced light collection efficiency
Increase resolution by:	**Sensitivity suffers due to:**
Using high energy and time cuts	Possible loss of trues
Reducing scanner diameter (reducing non colinearity)	Reduced number of detectors
Reducing detector size	Reduced stopping power Lower statistics per detector

Table II Resolution - sensitivity tradeoff in PET

2.1.3 Small animal PET imaging

Purpose

While the reasons to study small animal disease models in vivo using intact living subjects require no justifications, some other benefits of small animal PET imaging are not so obvious. For instance, PET allows these animals to be studied in their natural biological state, with active regulatory and feedback mechanisms. It enables repeated, longitudinal, nondestructive studies on the same animal. There is a large area of ongoing research focused on the development of specific probes to obtain different types of information from these studies. Finally, since PET is already a standard clinical diagnosis tool, discoveries in preclinical PET are more likely to translate to the clinic.

Challenges

Small animal imaging presents a unique set of challenges not just due to higher resolution requirements owing to a factor of 10-20 reduction in organ sizes, but also due to limits on injected dose and considerations of animal comfort. In terms of resolution and sensitivity, the small ring diameter of these systems relative to the object can be an advantage, but also poses problems as shown in Table II. High injected doses improve image SNR, but are impractical due to regulations on radiation dose. Also, high injected doses might be ineffective if the specificity of the radiotracer to the target is low. Non-specific binding of the tracer increases background activity and necessitates good contrast recovery by the imaging system. Randoms and scatter fractions are expected to be low but systems designed to image specific organs could be affected by these from organs outside the FOV. The selection of the ROI (typically done on the reconstructed image using specialized software) is also crucial, since structures that are smaller than the resolution of the system could be underestimated and appear larger than their true size due to the **partial volume** [59] effect.

Current art

Several small animal research prototypes [60-63] [43] have been developed over the last decade that are variations on the same theme of scintillation detectors and position-sensitive photodetectors (a notable exception being [64], which uses a multi-wire proportional chamber) The Siemens microPET [25, 46, 65, 66] line (originally developed at UCLA) is among the pioneers of small animal PET systems, and their tomographs are considered the gold standard even today. Other unique commercial systems are listed below:

- The Siemens Inveon [67] is an upgrade on the microPET Focus [25] with larger detectors and tapered light guides. It boasts of a 1.5mm FWHM spatial resolution at cFOV with 10% sensitivity at 250 keV.
- The General Electric eXplore Vista uses an LSO-GSO phoswich design [68] to obtain a resolution of 1.6 mm at cFOV with a sensitivity of 4% at 250 keV.
- The Philips MOSAIC [49], originally developed at the University of Pennsylvania is composed of a continuous band of 17,000 detector elements that connect to a bank of standard PMTs through an annular diffuser. These models have slightly lower resolution and sensitivity compared to the Siemens and GE systems.
- Gamma-Medica Ideas uses trapezoidal BGO crystals [69, 70] to increase the packing fraction and eliminate gaps between detectors. Their system achieves similar performance to the Siemens Inveon. Gamma-Medica also produces an APD-based dual crystal (LSO/lutetium gadolinium oxyorthosilicate) with pulse shape discrimination to identify the channel that has been hit by the incoming photon. This system has been developed from the LabPET system by the University of Sherbrooke [71] and reports the highest resolution among scintillator-based PET systems in the literature with 0.9 FWHM at cFOV [72].

2.1.4 Monte Carlo applications in PET

Monte Carlo techniques are useful research tools to model statistical processes, and are now being used extensively to simulate the stochastic behavior of radiation detection systems. There are a number of applications for Monte Carlo modeling in PET and SPECT including evaluation of prototype designs and original geometry configurations [40, 73-75], modeling of physical processes such as photon transport in matter (object or detectors) [23, 76, 77] assessment of reconstruction and correction algorithms [78-80] and pharmacokinetic modeling [81]. These random processes can be complicated to model mathematically, and Monte Carlo simulations are a practical solution when empirical measurements are impossible.

The key components of an Monte Carlo package are a random number generator, stored probability distributions for some particles interacting in a few types of materials (based on energy, Z etc) and rules to sample the probability distributions. The distribution of the source and the object is defined by the user, and program tracks particles by sampling the probability distributions as they interact in the object until they are detected or exit a predefined radius undetected. This simple concept is computationally intensive, and has been facilitated by recent advances in computing technology. Even so, a typical simulation requires several billion photons to be simulated and tracked. A variance reduction technique called importance sampling can be employed to accelerate the process which takes advantage of the fact that certain values are more "important" than others, and samples those more frequently. In other words, the algorithm preferentially generates photons with a high probability of detection and weights them by a factor based on the fraction of photons from that voxel (or three-dimensional pixel) that would be detected in a realistic case. A significant gain in computation time is achieved by not tracking the large fraction of photons that escape undetected. At the end of a simulation, a conversion factor is applied that converts #simulated decays to the #real world decays. This is a practical solution for applications which focus on the mean #decays but not its variance.

There are a number of public domain programs available for researchers to explore the potential of Monte Carlo software, most of which were originally developed for high-energy physics applications (MCNP [82], Geant4 [83]). The two packages used for simulating the RatCAP are algorithms developed specifically for PET and SPECT applications, namely The SIMulation System for Emission Tomography (SimSET) [84] and the Geant4 Application for Emission Tomography (GATE) [85]. A detailed description of the use of these packages to generate system response models for the RatCAP will be provided in this article.

Section Conclusion

This section was intended as a concise primer on the principles of PET and basic PET systems. From here on, the focus of this dissertation will be on quantitative PET data and image processing methods.

2.2 Data Organization in PET

The objective of this section is to introduce the terminology used for PET data and present an overview of data organization and representation methods through several sub-topics that address:

1. projection sampling conventions
2. organization of projections into sinograms
3. data acquisition and binning
4. data compression and minimum sampling requirements

The focus will be on 3D tomographs with block-detector based ring geometry and parallel beam sampling, although all types of systems will be touched upon.

Introduction to PET Data

PET data are collected as sums of counts along LORs or TORs connecting coincident detector pairs. For the 3D source distribution f(x), the total counts N in an LOR are known to be randomly distributed according to a Poisson probability distribution function with an expected value modeled as $E[N_{LOR}] \propto \int_{LOR} f(x)dx$.

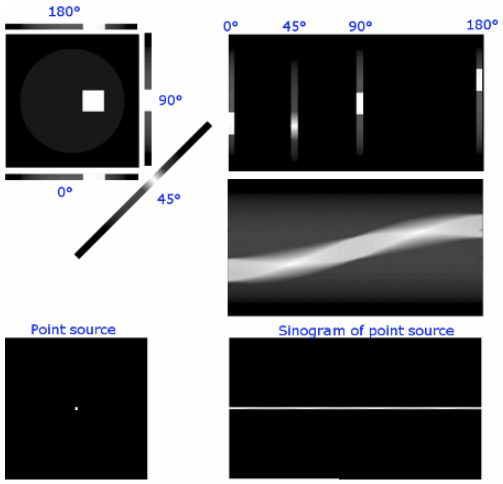

Figure 9 Sinograms - examples

(top) Organization of projections at 0°, 45° and 90° into a sinogram (bottom) Sinogram of a typical point source placed in the central field-of-view

The Sinogram

A sinogram is a 2D array containing an ordered collection of PET projections. Each LOR is represented on the sinogram as a pixel or "bin" as a function of the shortest distance (r) between the LOR and the center of the FOV (cFOV) versus its angle of orientation (ϕ). A collection of LOR sums at a particular angle is termed as the "projection" for that angle.

Assuming the innermost square region in Figure 9 has the maximum level of radiotracer concentration, and the circle represents background counts within the FOV, the projections for this source distribution at 0°, 45°, 90° and 180° are illustrated in the figure. If these projections are collected along a sufficient number of angles and stacked in rows, the complete sinogram shown on the right is obtained. For a centrally-placed point source, the projections at all angles are delta functions, resulting in the sinogram shown at the bottom of Figure 9. The name "sinogram" is derived from the fact that its shape resembles a set of overlapping sine waves, one for each pixel in the image. The distance of the pixel from the cFOV can be determined from the amplitude of the sine wave, and its angle from the phase.

For 3D volumetric PET, a separate sinogram is generated for each of the axial slices, and indexed by the angle this sinogram makes with the z-axis. The coordinate system used henceforth is shown in Figure 10A. The rotated transaxial plane forms an azimuthal angle ϕ around the object, and is at a copolar angle θ with the z-axis. Taking into account the fact that there will be multiple axial planes for every angle θ, sinograms for 3D PET data have 4 dimensions, expressed as (r, ϕ, θ, z).

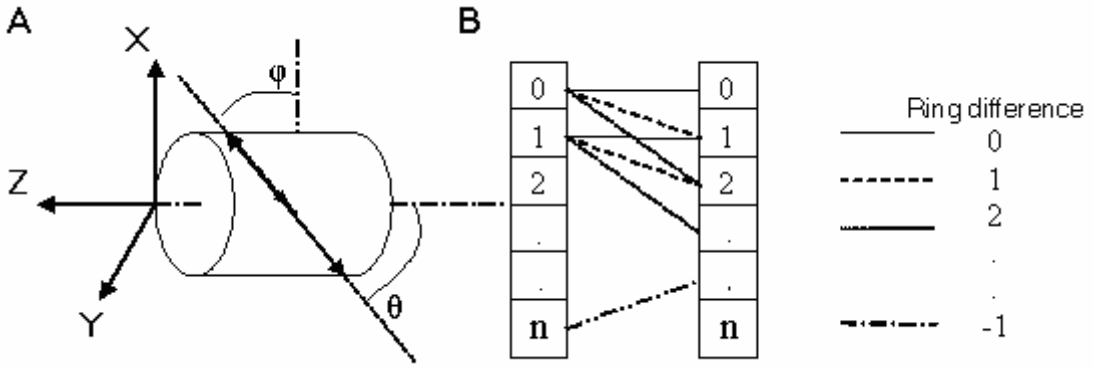

Figure 10 Considerations for 3D sinogram binning
A) Coordinate system B) Illustration of axial cross planes with ring differences of 0, 1, 2 and -1

Data Acquisition and binning

PET data is acquired either directly in the form of a sinogram (histogram), or event-by-event in the form of list. List-mode data can consist of coincident events or single events which are processed for coincidences by separate offline software. Although the entire singles list is typically a few hundred gigabytes for most systems, the advantages of the singles list mode data format is that it allows the parameters of the binning such as time and energy windows to be optimized post-acquisition. Reconstruction methods have also been developed to directly reconstruct list-mode data [86-88] bypassing the use of sinograms since these can be extremely large for 3D systems with multiple detector combinations, as shown later.

The binning procedure for each detected coincidence involves determining the LOR for the detector pair and incrementing the counts in the sinogram pixel associated with that LOR. A non-working detector can be identified by the diagonal streak formed by its LOR combinations from 0° to 180°. If an entire detector block is not working, adjacent streaks will form a wide band. Thus, sinogram is a visually useful arrangement of the LORs in a PET scanner, and aids the experienced user in the detection of errors in the system prior to reconstruction.

Axial data organization and compression

Figure 10B illustrates a cross section along the axial dimension of two opposing block detectors. Each block is made up of n detectors, with a pitch of, say, x mm. A complete ring tomograph made up of these blocks would comprise n_r detector "rings". If a detector within a ring is only allowed to be in coincidence with other detectors on the same ring, shown by the solid line in the illustration, the detected coincidences are called "direct" coincidences. 2D PET imaging systems allow only direct coincidences with a ring difference of 0. For the above illustration, this would result in n_r image planes, each x mm apart. For an improvement in axial sensitivity, higher values of ring differences are allowed by standard PET scanners, called "cross" planes. The maximum possible cross coincidence slices for ring differences from $-(n_r-1)$ to $+(n_r-1)$ is n_r*n_r. In the image, this would result in (n_r) direct planes and (n_r-1) cross planes or $(2n_r-1)$ total planes with a center-to-center spacing of (x/2).

One method to take advantage of the improvement in sensitivity using a larger ring difference without increasing the size of the sinogram by a factor of n is to combine certain cross planes into a single plane. For example, if the plane formed by detectors 0 and 2 in Figure 10B is combined with the direct plane at 1, there will be only a small loss of axial resolution. The term "span" is used to describe the number of allowed axial combinations. If a maximum ring difference of ±7 is allowed, 4 cells can be combined to form an odd plane, and 3 cells to form an even plane. Hence, the sinogram is said to be compressed by a span of 7. Of course this is strictly true only for planes near the cFOV, since all combinations may not exist at the edges. If cross planes are combined in this manner, a plane efficiency correction is necessary to account for variations in the number of LORs contributing to a plane. Even with the maximum ring difference of n-1, planes towards the end of the axial FOV are less sensitive, hence noisier than the central planes. Also, even numbered planes are noisier than their odd counterparts [89]

Transaxial compression

An alternate method to reduce storage size and improve the statistical quality of the sinogram pixels is to combine angular (ϕ) samples. This is achieved by a process called "mashing" which can be applied in certain oversampled systems without compromising

spatial resolution. A mashing factor of 1 means that adjacent rows in a sinogram have been added, and the assumption is that the data was acquired half way between the 2 samples.

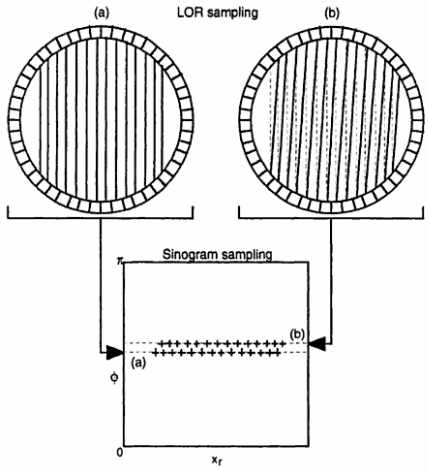

Figure 11 Transaxial sampling.

Diagram obtained from [1]. Adjacent rows in a sinogram have an offset in the transverse sampling pattern

Sampling, Size and Storage Considerations

In PET systems with discrete detectors, the sampling interval is determined by the size and number of detectors forming the ring. With reference to the ring tomograph in Figure 11, assuming there are N_d detectors within a ring, the parallel sampling pattern suggests that the number of angular samples, N_ϕ in the range of $0 \le N_\phi < \pi$ is equal to N_d. The optimal number of transverse samples, $N_{xr} = N_d/2$ but could be limited to half of that for large scanners with relatively small FOVs.

Interleaving

Since ring PET systems are typically undersampled in the linear direction and adequately sampled in the angular direction, the projection data are rearranged by "interleaving" adjacent angular views as shown in Figure 11 to form sinograms with twice the transverse sampling rate and half the angular sampling rate. Although this leads to a slight (negligible) error of $\Delta\phi/4$ in the coordinate of the bin center, this is a widely-accepted convention for a better balance between linear and angular sampling. In addition, researchers [66, 90] have invented systems with a built-in detector motion called "wobble" that increases the number of linear samples and hence the sampling interval.

Sinogram sizes

With interleaving, the number of transaxial samples, $N_{xr} = (N_d/2) + (N_d/2\text{-}1) = N_d\text{-}1$. The number of ϕ-samples, $N_\phi = N_d/2$. Bin sizes are $\sim 2R/N_{xr}$ and π/N_ϕ respectively. In the axial

dimension, there are $n_r * n_r$ possible ring combinations that are indexed by their ring difference (or "segment", given by ring1-ring2) and an average z-coordinate (ring1 + ring2)/2. The bin size here is simply L/n_r Thus, the total size of a fully 3D, uncompressed sinogram with n_r rings and N_d detectors is $(N_d-1) * (N_d/2) * N_{rings} * N_{rings} * nb$ where nb is the number of bytes used for the storage of each bin. A state-of-the-art preclinical scanner, the Concorde Focus [91] consists of 48 rings of 168 contiguous detectors. If uncompressed sinograms were stored, this would result in a sinogram size of 62MB. Dynamic sinograms with 20-30 time frames require gigabytes of storage. Some investigators have devised lossless compression schemes [92] to alleviate this problem, which involve storing a single sinogram with spatial information, supplemented by a compressed "timogram" with the arrival times of each event. Other researches directly reconstruct list-mode coincidence data [86-88] one annihilation event at a time and bypass the sinogram binning step. List-mode reconstructions exploit the redundancy in PET sinograms and have gained popularity over the past few years for systems in which the number of annihilation events detected is expected to be far less than the number of elements in a sinogram.

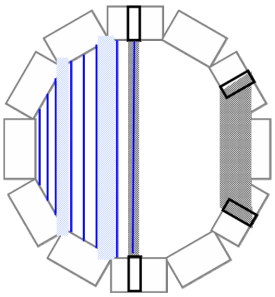

Figure 12 Illustration of sources of sampling errors in a PET sinogram
1) gaps between detectors (blue band) 2) uneven LOR spacing (blue lines) 3) parallax (black).

Sources of error

1. **Gaps between detectors**

Missing projections due to the gaps between detectors complicate the use of analytical reconstruction algorithms which assume complete sampling. The missing projections are shown as blue bands in Figure 12.

2. **Non-Uniform LOR spacing (Need for arc correction)**

For parallel beam sampling, LORs towards the center of the gantry are spaced farther apart than those on the periphery, due to the curved nature of the detector ring as shown by the solid blue lines in Figure 12. Since basic reconstruction algorithms assume even spacing, an "arc correction" needs to be applied to resample the data into a uniform sampling grid. Such a correction is more important for the smaller FOVs of preclinical PET systems, or when the object fills a large fraction of the detector aperture.

3. **Parallax errors**

Another problem that takes on a higher significance for small animal systems compared to clinical systems is that of parallax error due to penetration of the 511 keV

photons in the detectors. This leads to a broadening of the LORs depending on the angle of the coincident detectors, and is illustrated by the black bands in Figure 12. For newer systems that can resolve the depth of the photon interaction (DOI) [37, 44], this problem has been solved to some extent. For systems without DOI capability, researchers try to optimize the design of the system to reduce the parallax effect by i) using large system diameters relative to the imaging FOV, ii) using shorter detectors and compromising detection efficiency for resolution [66], iii) using planar detector arrays instead of cylindrical geometries.[93], iv) use of dual-layer phoswich detector designs[49, 54, 74]. For conventional PET systems, advanced reconstruction algorithms with accurate system response models can be employed to account for parallax.

Section conclusion and minimum sampling requirements

The maximum recoverable spatial frequency is one half the detector size, and can be obtained with uncompressed sinograms that have not been resampled. This may not be feasible for larger systems with millions of LORs, and some undersampling may be necessary. If R_{int} is the intrinsic resolution achievable dictated by detector size and positron physics, the minimum linear sampling requirement to satisfy Nyquist criteria is $\Delta r \leq 0.5 * R_{int} \rightarrow N_r \sim N_d/2$. According to the sampling theorem, angular sampling should be better or equivalent to Δr which means $\Delta\phi \leq R_{int} * 180/(\pi D) \rightarrow N_\phi \geq \pi D/R_{int} \sim N_d/2$.

2.3 PET Image Reconstruction

As described in the previous section, a sinogram is the set of projections (or forward projections) of the source distribution along radial LORs at different angles around the FOV of the tomograph. The source distribution can be reconstructed by distributing the sinogram counts back along the LORs that contributed to them. The line integral model naturally lends itself to PET data, and images can be reconstructed using analytical inversion methods based on a linear relationship between the measured data and the source distribution. This chapter describes such analytical methods, and discusses the improvement in accuracy achieved by iterative techniques that draw on more accurate models of the data and system response.

The reconstruction problem can be reduced to finding the solution to the linear system in equation **(8)** where Y_j (j=1..NLOR) is the measured data or sinogram, Xi (i=1..NVOX) is the source distribution and A is the projection matrix that relates x and Y.

$$Y_j = \sum_{i}^{NVOX} A_{ji} X_i \qquad (8)$$

The selection of the image reconstruction approach is crucial for the accurate reproduction of high count regions where the precision of the reconstruction algorithm limits the resolution as well as low count regions which are dominated by statistical noise. It must be noted that Equation **(8)** represents the mean value of Y but not its statistical variation about the mean. The main goal of the reconstruction approaches discussed in this chapter is to optimize the tradeoff between resolution and noise for quantitatively accurate PET images. The onus is on the reconstruction method to maximize the potential of modern detector technology.

Reconstruction of 3D PET data

3D-PET imaging has been the norm since the early 90s, when advanced mathematical and computing techniques were developed to exploit the benefit of increased sensitivity through the removal of inter-plane septa. Several algorithms for the reconstruction of 3D sinograms exist, but the procedure is computationally intensive due to the considerable increase in the number of lines of response as discussed in Section 2.2. Rebinning methods are often used to resample 3D sinograms back to 2D, followed by reconstruction using a 2D algorithm. The single slice rebinning (SSRB) method was proposed in 1987 [94] wherein the event from an oblique plane is placed in the 2D plane that most closely matches the axial position of the center of the line of response. It is obvious that this is most accurate for events on the central axis of the tomograph, but deteriorates for events at some radial distance from the cFOV. This renders the method unacceptable for tomographs with a large axial extent and acceptance angle. The Multi-Slice Rebinning Algorithm (MSRB) [95] was developed as an improved version of the SSRB, and spreads the counts among all the 2D sinograms

through which the oblique plane traverses. Though more accurate than SSRB, this approach has been shown to be unstable with noisy data. The Fourier rebinning (FORE) [96] approach rebins oblique sinograms based on the relationship of their 2D-FT with the 2D-FTs of in-plane sinograms. It has been shown to outperform SSRB and be more stable than MSRB even in tomographs with large acceptance angles [97]. FORE combined with 2D reconstruction (analytical or iterative) has been shown to be more than an order of magnitude faster than fully 3D reconstruction, and is currently the method of choice for PET systems with impracticable 3D reconstructions due to a large number of LORs [98, 99].
The following sections present an overview on analytical and iterative reconstruction approaches for 2D as well as 3D data, with brief discussions of their strengths and weaknesses.

2.3.1 Analytical reconstruction

The basic idea of back projection is to run the projections back through the image space along the LORs to obtain a rough approximation of the original source distribution. It is described mathematically in equation **(9)** where, for n=1..N projections, $s(r,\phi_n)$ represents the number of counts in the sinogram at projection angle ϕ, radial bin r and a(x,y) represents the reconstructed image.

$$a'(x,y) = \sum_{n=1}^{N} s(r,\phi_n) = \frac{1}{N}\sum_{n=1}^{N} s(x\cos\phi_n + y\sin\phi_n, \phi_n) \qquad \textbf{(9)}$$

It is apparent from the illustration in Figure 13 that a simple back projection of a centered point source would result in a blurred representation of the object because the counts are evenly distributed along their LORs. Increasing the number of projections improves image quality, but the resolution of the final image is not optimal.

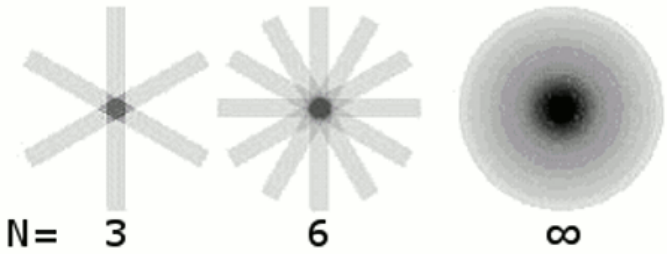

Figure 13 Back Projection: Blurring and star artifacts. From [27]

Taking into account the blurring factor, the relationship between the back projected image a'(x,y) and the true activity distribution a(x,y) can be given by equation **(10)**, where r is the distance from the source. A high pass filter is typically used to eliminate the blurring as discussed below.

$$X'(x,y) = X(x,y) \otimes \frac{1}{r} \qquad (10)$$

A. Direct Fourier Reconstruction Technique

The Filtered Back Projection (FBP) algorithm currently used by PET scanners is based on a combination of the simple back projection discussed above and the Direct Fourier Reconstruction technique (DFRT). The backbone of both approaches is the Fourier Central Section theorem which states that the one-dimensional Fourier transform (1D-FT) of each parallel ray projection profile of an object is equal to a central section of the two-dimensional 2D-Fourier transform (2D-FT) of the object. Thus, every sinogram projection bin contains the data for one line through the 2D-FT of the object at an angle related to the projection angle. DFRT is performed by acquiring projections at multiple angles, taking their 1D-FTs and then finding the inverse Fourier transform of the resulting complete 2D-FT of the object. This process is likened to that of finding the inverse of the Radon transform (sinogram). Since the positioning of the 1D-FTs on the 2D k-space, based on polar angle and interpolation, is a bit complex in its implementation [100], a much simpler approach to reconstruction was devised by combining the two theories above.

B. Filtered Back Projection

FBP is the primary analytical reconstruction algorithm used for ECT data. It not only simplifies the DFRT algorithm, but also accounts for the 1/r blurring factor from Equation **(10)**. The steps involved in FBP are:

1) Compute 1D-FT for each projection.
2) Apply high pass filter to eliminate effects of blurring.
3) Compute the inverse FT (1D) of each filtered FT profile to obtain filtered projections.
4) Perform conventional back projection on the filtered profiles.

This would result in accurate, high resolution, artifact-free reconstructions for ideal data. In practice, the ramp filter used to suppress low frequencies enhances high frequencies, and could therefore amplify statistical noise in the data. Practical reconstruction involves optimization of the filter using modified ramps like the Hann and Hamming filters [101], usually selected based on the object to be reconstructed. In the discrete formulation of this algorithm for PET, the filter needs to be cut-off at a frequency vmax = 1 / 2 x Δr, where Δr is the distance between the samples in the sinogram and v_{max} represents the highest frequency that can be faithfully detected from in the sinogram.

C. 3D analytical reconstruction

If the reconstruction time and computational resources required were not issues of concern, 3D-FBP would be the obvious choice over 2D methods. There is, however, an additional complication to its application to 3D-PET data. Similar to 2D-FBP which is

designed for a complete ring of detectors, its 3D version expects sampling within a complete sphere. The issue of truncated projections arises with cylindrical detectors when a detector in an LOR does not have an associated pair, due to the limited axial FOV. Truncated projections are illustrated in Figure 14 (step 2) and increase in number with larger oblique angles. Only segment 0 (with in-plane coincidences) is free of truncated projections.

The solution to this problem devised by Kinahan and Rogers [103] was to first obtain an initial, noisy estimate of the source distribution using 2D projections (i.e. using only in-plane coincidences). This is forward projected (reprojection step) to estimate the truncated projections. The complete dataset is then reconstructed using 3D-FBP. This algorithm illustrated in Figure 14 is called the 3D ReProjection algorithm (3DRP) and is the gold standard for 3D analytical reconstruction of PET data. Groups have used parallelization techniques or resampling techniques to speed up reconstruction time and make it feasible for clinical applications. However, it is interesting to note that Defrise et al [104] and Matej et al [97] have independently shown for moderate and large angle tomographs respectively, that similar results to 3DRP can be obtained using FORE, but with a significant speed up in processing time.

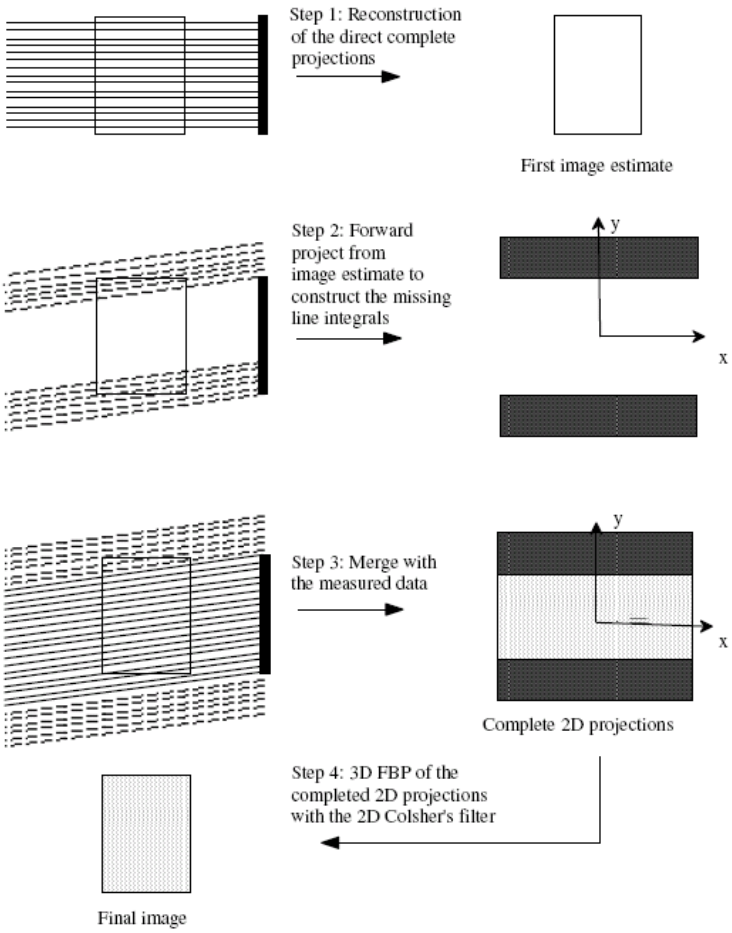

Figure 14 Illustration of the 3DRP algorithm. Obtained from [102]

Limitations

While it has been established that FBP is fast (in 2D) and straightforward to implement, the limitations to its application lie in the very assumptions that simplify it. These include:

- Assumption of adequate linear and angular sampling

Minimum sampling requirements are discussed in Section 2.2 and summarized here:

- Linear sampling requirement to satisfy Nyquist criteria: $\Delta r \leq 0.5 * R_{int} \rightarrow N_r \sim N_d/2$
- Angular sampling requirement to satisfy Nyquist criteria: $\Delta\phi \leq R_{int} * 180/(\pi D) \rightarrow N_\phi \geq \pi D/R_{int} \sim N_d/2$

With recent block detector geometries, gaps between detectors can lead to major sampling artifacts in FBP. Even in ring detector systems composed of individual detectors where the radial and angular sampling is determined by the number of detectors and their width, missing or distorted detector elements due to hardware failures or other such inconsistencies could violate the assumptions of FBP.

- Assumption that the entire object is included in all projections.

If this is not true, data will be inconsistent between projections and FBP will not perform to its maximum capacity.

- Assumption of noiseless data

Statistical noise causes streak artifacts. Filters can be designed with a strong cutoff frequency for high resolution, but this compromises spatial resolution.

These limitations have prompted researchers to explore iterative reconstruction algorithms discussed in the next section.

2.3.2 Iterative reconstruction

Spatial resolution in PET is primarily determined by the size of the detector element. However, as mentioned in the introduction, a combination of other factors such as crystal penetration, positron range, noncolinearity of the photon pair, photon attenuation and scatter and variations in detector pair sensitivities contribute to additional blurring of the point spread function. Some of these effects deviate from the implicit line integral assumption of analytical reconstruction algorithms and render them less suitable for PET systems. Though methods have been developed to correct for these effects in 3DRP and FBP, [105] there are often caveats to their application especially to noisy data. Therefore, another major limiting factor for analytical methods is that they do not account for statistical variability in PET data. Reductions in image noise by methods such as smoothing come at the expense of spatial resolution. For increased sensitivity with small-diameter PET systems, it is optimal to reconstruct a large fraction of the detector aperture, and hence the ill effects of crystal penetration and angled detectors, which complicate FBP, are more pronounced in small animal PET tomographs. The promise of high resolution throughout FOV and improved

noise performance has made iterative reconstruction methods extremely attractive for small animal PET scanners. This section will discuss the approach as well as a few algorithms that have recently gained widespread acceptance in preclinical imaging.

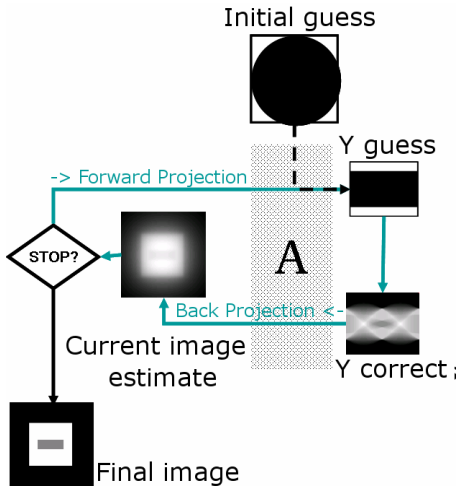

Figure 15 Iterative reconstruction techniques - Illustration of concept

Conceptual Overview

The principle of iterative reconstruction algorithms, illustrated in

Figure 15, is to find a solution to equation (8) using successive estimates. A represents the projection matrix that relates the source distribution to the measured data. An initial estimate for the source distribution or image is required to start the process. This is usually a smooth uniform function. The forward projection of this estimate through A, (Y_{guess}) is compared with the measured data Y. A correction sinogram, $Y_{correct}$ is obtained, which is a subtraction in case of Algebraic Reconstruction Technique (ART) [106] and a ratio in the case of newer algorithms such as MLEM, described in detail later. $Y_{correct}$ is back projected through A and applied (again, as an additive or multiplicative factor) to update the initial estimate. One such pass including a forward and back projection is called an iteration. Successive iterations achieve better results, until a reasonable agreement is obtained between the projection of the image estimate and the measured data.

Components of an iterative reconstruction algorithm

A bare-bones iterative approach that would straightaway outperform FBP would compute forward and back projectors on-the-fly, until a good match is achieved. This idea can be developed further by the incorporation of any knowledge of the system response and statistics of the data into a precomputed model. A standard model-based statistical iterative reconstruction algorithm has the following basic components:

1. The image model or basis function
2. The system response model
3. The statistical model for the data modeled into an objective function
4. The optimization algorithm.

The application of model-based statistical iterative reconstruction algorithms to PET began with the pioneering work by Shepp and Vardi [107] and Lange and Carson [108]. These algorithms and their accelerated versions are still prevalent today.

1. Basis functions

The reconstruction problem is modeled as a linear relationship between the measured data and a set of basis functions which represent the source distribution f(x). Although f(x) is continuous, finite discretized representations are typically used as a simplification. The most common basis elements also used for RatCAP images are contiguous and non-overlapping 3D pixels or voxels. The image value at a voxel represents the total number of positron decays within the area occupied by the voxel. The 3D voxel array is centered on the origin of a 3D Cartesian grid.

Since the reconstruction algorithm itself does not impose any conditions on the choice of basis functions, other quasi-continuous approaches have been proposed. Spherically symmetric, overlapping volume elements called blobs [109] are routinely used by Matej and related groups. The (mostly) band limited response of blobs is expected to produce images without aliasing compared to voxels with high-frequency edges. Provided the parameters to control the shape of the blob are selected correctly, they have shown suppression of noise and better accuracy in slowly varying regions. The resolution (using a specialized reconstruction algorithm [109]) has been shown to be comparable to voxels, and better than approaches that use a voxel basis post-smoothed with a Gaussian filter after reconstruction. Another alternative basis function that attempts to solve the geometry-dependent resolution degradation problem is the use of natural pixels [110] in which the size of the basis element varies naturally according to the sampling pattern of the system. Newer methods have been proposed that have not yet been applied clinically such as wavelets [111]. Four-dimensional reconstruction algorithms that perform spatio-temporal reconstruction use a generalized B-spline basis functions, where the rate function for each voxel is estimated by maximizing the likelihood of arrival times over the control vertices of the spline [112-114].

2. **System response models**

The system response model is used to generate the projection matrix A such that A_{ij} represents the probability that an emission from pixel i will be registered by the jth detector pair. Any linear physical effect (photon attenuation and scatter, positron range etc.) can be modeled into the sensitivity function. The accuracy of the model determines the accuracy of the reconstruction.

The only hindrance to the universal application of model-based iterative algorithms is the computational challenge they present, which is proportional to the number of LORs and the number of voxels. A typical model for a 3D human scanner could have up to 10^{13} elements in the matrix. Though a large fraction of these would be empty, detailed modeling of physical effects reduces the sparseness, thus increasing memory requirements. The optimal projection matrix would optimize the tradeoff between accuracy, required storage and speed.

In some cases, rebinning algorithms are used to reduce the problem to the reconstruction of a set of 2D sinograms, but this results in suboptimal resolution recovery. Alessio et al [56] adjusted their 2D system response functions to account for the blurring caused due to rebinning. Other investigators have made storage practicable by exploiting the inherent symmetries of the system [115] which cause redundancies in the matrix. Though this significantly reduces the storage requirement, the reconstruction algorithm would still demand high computation power. Since no easy solution to the time and matrix storage issues exists, researchers are forced to devise alternative methods to optimize image reconstruction.

System response models used for reconstruction in existing PET systems are based on analytical calculations, empirical measurements, Monte Carlo simulations, or a combination of one or more of the three approaches. A few interesting cases in each category are reviewed below.

i) Analytically estimated system response models

Some PET systems use a simplistic, spatially invariant, "geometric" system response model based on the tubes of response connecting detector pairs. More involved approaches take into account the solid angle subtended by the source and the detectors [116], or the intersection of detector tubes of response [117] with voxels. Detailed system response functions that account for detector blurring can be analytically calculated [57] but concerns regarding the storage of these matrices and the feasibility of the approaches have not been discussed in the literature. Qi, Leahy and colleagues devised a popular factored system model approach [118] which has been adopted by newer systems. The main motivation for their approach was a reduction in the storage size of A by optimizing the use of symmetries, reducing the problem to the product of a few diagonal matrices, precomputing some factors and calculating others on the fly. Switching to their terminology for the remainder of this section, matrix A = P[MxN] where M=NLORS and N=NVOXELS. They factored P as follows:

$$P = P_{det.sens}\, P_{det.blur}\, P_{att}\, P_{geom}\, P_{positron}$$

$P_{det.sens}$ (MxM) is a diagonal matrix of detector efficiencies can be measured directly for a particular system (and is related to the number of detectors and not M which is much larger).

$P_{det.blur}$ (NxN) is the key to the success of this approach and achieves significant time and storage savings. This matrix accounts for the blurring of the point spread function due to factors such as photon pair noncolinearity, inter-crystal scatter and penetration. Since there is

a rotational symmetry in the blurring kernel [119], these need to be computed and stored only for a single projection angle. The kernels are estimated using Monte Carlo simulations.
P_{att} (MXM) is a diagonal matrix containing attenuation factors.
P_{geom} (MxN) is the geometric projection matrix, based purely on solid angle. Since P_{geom} is very sparse, symmetries are used.
$P_{positron}$ (NxN) accounts for blurring due to positron range.

By deconvolving the system response in this manner, they achieved a uniform transaxial resolution of 1mm FWHM within a radius of 4 cm from the cFOV using the microPET R4 [66]with 2 mm detectors and 17 cm ring diameter.

ii) Empirically measured system response models

It is obvious that if the time required for matrix estimation, reconstruction time and memory availability were immaterial, empirical measurements [120, Selivanov, 2000 #209] of point sources stepped through the FOV would produce the most accurate projection matrix. A direct measurement, especially for human size scanners, is no trivial task. The arduous effort of Panin and group to use a combination of direct measurements and modeling has been detailed in [120]. Their matrix acquisition for a small sector that corresponded to the symmetry of 1 block of the clinical Hi-Rez scanner with a 50-cm diameter took 1 week and resulted in 21GB of data after zero-suppression and compression. Despite that, it lacked precision in the sampling of the matrix and made various assumptions. There are a number of additional drawbacks that possibly negate the benefits of this approach, for e.g. accurate positioning of the source would require specialized hardware; effects such as scatter and positron range would require additional separate models.

iii) Monte Carlo-estimated system response models

In theory, Monte Carlo-estimated data [121-123] should be equivalent to measured data provided the system has been modeled accurately. This approach could even offer a few advantages over the direct measurement approach including the flexibility to model complex, non-homogenous objects [124] and inconsistencies among detector sensitivities. Monte Carlo matrices can be decomposed post hoc into their geometric and blurring components which would lead to further understanding of the system response. However, as with empirical models, this is only possible if the system is small enough for simulations within a reasonable amount of time. It also requires a faithful reproduction of the measured data, since inconsistencies between the reconstruction model and the measured data lead to reconstruction errors, even for noiseless data. The focus of this dissertation is the optimization of the Monte Carlo-based reconstruction for quantitatively accurate imaging with the RatCAP as elaborated on in Section 3.

3. Objective functions

One A has been estimated or measured, the reconstruction problem involves finding the image X where $X = A^{-1} \cdot Y$ (from Equation. **(8)**). The direct inversion of A is not feasible for three reasons:

1) Since the system is ill-conditioned, small perturbations in the data cause a high variance in the image, making it unstable.
2) A is very large, and inversion would require high computing power.
3) Direct inversion would not account for statistical noise in the data.

Instead, the data noise model and its expectation are modeled into an objective function Q, which is the probability that x gives rise to observation y. The solution to this is found by successive approximations or iterations of the optimization algorithm. Q is designed such that it is a good fit with the data, and accurately represents the relationship between the measured data and the source distribution. It consists of a data mismatch term, an optional regularization term (for Bayesian approaches, discussed later) and constraints such as non-negativity. Additionally, any prior conditions on the image (with respect to smoothness, for instance) may be incorporated into Q. The reconstructed image is the one that maximizes Q.

Since the detection of events by PET systems is an independent Bernoulli process, sinograms are modeled as a set of independent Poisson variables. For a system with NLOR detector bins, the mean of the data $\hat{Y} = \{\hat{y}_j, j = 1, 2, .., NLOR\}$, is related to the unknown tracer distribution $X = \{x_i, i = 1, 2, \ldots, NVOX\}$ by the following equation:

$$\hat{y}_j = E[y_j] = \sum_{i}^{NVOX} x_i A_{ji} + r_j + s_j \qquad \textbf{(11)}$$

where A is the average probability that an event in voxel i will be detected by LOR j and r and s represent random and scattered events.

Given formula **(11)**, the conditional probability (likelihood function) for the measured data Y, given the source distribution X can be represented by the product of independent Poisson distributions as follows:

$$L(X) = p(Y / X) = \prod_{j} e^{-\hat{y}_j} \frac{\hat{y}_j^{y_j}}{y_j!} \qquad \textbf{(12)}$$

The goal of the reconstruction approach is to maximize equation (12). Since log(L(X)) and L(X) are both monotonic, the log of the likelihood given below can be maximized for ease of implementation.

$$Q = \log(L(X)) = -\sum_{j} \hat{y}_j - y_j \log(\hat{y}_j) + \log(y_j!) \qquad \textbf{(13)}$$

The maximum likelihood estimate is known to be unstable [125] and the resulting images exhibit large variances. An effective remedy to this problem is the use of a "penalty" function that favors smooth images by penalizing rough ones. The penalized likelihood function can be written as:

$$Q = L(X) - \beta R(X)$$

where R is the roughness penalty and β is a variable parameter that controls the noise vs. bias (smoothness) tradeoff. Alternatively, the solution can be maximized over the posterior probability rather than the likelihood. The posterior probability p(X/y) is found through Bayes' theorem by combining the likelihood function p(y/X), with a prior p(X) which reflects a priori knowledge of the source distribution. It can be written as: p(X/y) = p(y/X)p(X) / p(y), and its maximizer is known as the Maximum A Posteriori (MAP) estimate of the image. Taking the log of the above equation and dropping constants, the objective function becomes:

$$Q = L(y / X) + \ln(p(X))$$

Thus, the MAP estimator maximizes the sum of the log likelihood and the log of the prior, and is computationally similar to the penalized ML objective function. Bayesian [119] methods and penalized ML methods [126] both have a regularizing effect on the reconstruction, and the terms are often used interchangeably except in the case where the penalty functions are explicit functions of the data [126]. These approaches employ a variety of techniques [118, 127] [128] to estimate the priors and have been implemented in commercial as well as research systems.

4. Optimization Algorithms

The tracer distribution which maximizes the probability of the measured data is termed as the ML estimate. Only ML algorithms will be discussed in this section, but readers are referred to [129-132] for thorough reviews of other techniques. Maximization is performed by producing a sequence of image estimates which should converge to the correct solution. Other typical requirements are that the algorithm is stable, efficient and has fast monotonic convergence. Though the choice of algorithm does not (or should not) influence the solution, considerations on stopping points and actual implementations of algorithms make the solution slightly dependent on those choices.

The most widely-used iterative algorithms in clinical PET are Maximum Likelihood Expectation Maximization (MLEM) [107, 108] and its accelerated version, Ordered Subsets Expectation Maximization (OSEM) [133]. MLEM is derived below:

The Maximum Likelihood Expectation Maximization Reconstruction Algorithm

Maximizing the log of the likelihood from equation (13) is equivalent to minimizing the negative log of the likelihood. Rearranging equation (13) and substituting from **(8)**, the parameter to be minimized becomes:

$$Q = \sum_{j=1}^{NLOR} \sum_{i=1}^{NVOX} A_{ji} x_i - \sum_{j=1}^{NLOR} (y_j \log(\sum_{i=1}^{NVOX} A_{ji} x_i)) + \log(y_j!) \qquad (14)$$

The minimum of this function is the value of x at which the derivative becomes zero.

$$\frac{\partial Q}{dx} = \sum_{j=1}^{NLOR} A_{ji} - \sum_{j=1}^{NLOR} A_{ji} \frac{y_j}{\sum_{i=1}^{NVOX} A_{ji} x_i} = 0 \qquad (15)$$

This can be solved iteratively using equation **(16)** below:

$$x_i^{n+1} = \frac{x_i^n}{\sum_{j}^{NLOR} A_{ji}} \sum_{j}^{NLOR} A_{ji} \frac{y_j}{\sum_{k}^{NVOX} A_{jk} x_k^n} \qquad (16)$$

The MLEM formula can be broken down as follows:

$$x_i^{n+1} = \frac{x_i^n}{\sum_{j}^{NLOR} A_{ji}} \sum_{j}^{NLOR} A_{ji} \frac{y_j}{\sum_{k}^{NVOX} A_{jk} x_k^n}$$

With the yellow term being the forward projection or the values of y_j that would be measured if Σx_k was the image. This is compared to the actual measured values of y by taking the ratio, which is then back projected as shown in the green term to find the image update values. Another way of looking at this formulation is that each iteration consists of an "E" step, involving the computation of the conditional expectation of the log likelihood, and an "M" step, which is the maximization of this expectation with respect to the image.

EM properties

EM algorithms have properties that are very attractive to ECT systems such as:

- Non-negativity
- Monotonic convergence
- Count rate preservation at every iteration.

However, one of the main drawbacks is that the algorithm requires a large number of iterations to converge to the image that maximizes the log likelihood as shown in Figure 16 (top). The performance is object-dependent, some parts (typically the low frequency components) of the image will converge before others (Figure 16 (bottom)). Methods such as ordered subsets (OS) [133, 134] are used to accelerate E-M steps, but may have problems converging (although convergent OS algorithms [134, 135] have been developed).
Another drawback that will be discussed in the following subsection is the increase in variance (error) with iteration, due to ill conditioning of the matrix [125, 136] also shown in Figure 16 (top).

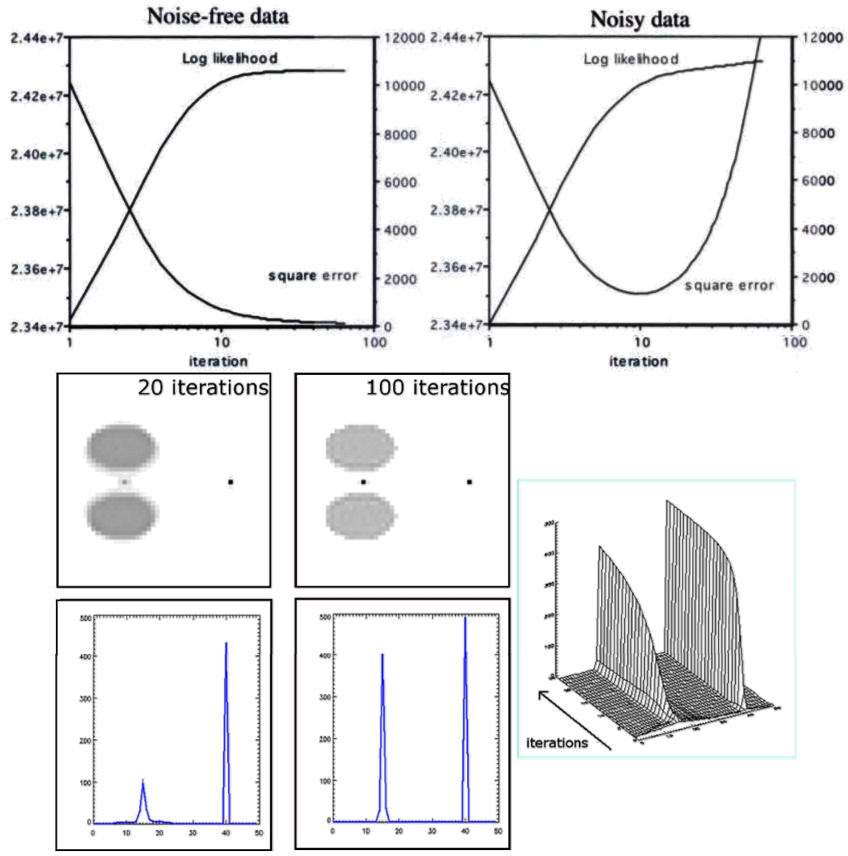

Figure 16 MLEM properties
(top) convergence and noise (center and bottom) non uniform convergence. Obtained for illustrative purposes from [36]

Noise control

The "best fit" of noisy data to an ill-conditioned problem could cause instabilities in the reconstruction. This means that the reconstruction is so sensitive to small perturbations in the data that it produces increasing variance with iterations resulting in checkerboard

artifacts. In practice, the variance of an ML estimate is controlled by starting with a smooth initial estimate and terminating the algorithm before convergence [137]. Since running the algorithm to convergence minimizes the bias, other techniques are ideally used to handle the instability. The choice of basis function, as described above, impacts noise control. Groups reduce image noise variance with the use of sieves [138] or smoothing between iterations [139]. The penalized ML and [126, 140] the technique of reformulating the problem in the Bayesian framework (MAP) [127, 141] to include a priori knowledge of image smoothness are used for regularization. These find the solution that fits best with prior expectations of image smoothness. Stayman and Fessler [128, 141] have shown that indistinguishable noise properties, convergence and resolution properties have been observed by iterating to convergence and then post-smoothing with a Gaussian filter, as compared to MAP.

Section Conclusion

This summary only scratches the surface of what is an impressive amount of literature on the topic of image reconstruction in ECT. Analytical methods are well understood and could be useful to test the expected performance of new tomographs. However, improved system modeling leads to better results with iterative reconstruction methods especially when equally spaced, complete projections are not available. The selection of the individual parameters for iterative reconstruction approaches discussed in this chapter can have a significant impact on image resolution, noise and overall quantitative accuracy.

2.4 Quantitation in PET

PET imaging applications usually have a high quantitative emphasis. Reliable quantification of the signal in the presence of high statistical noise is vital for the analysis of PET data, where errors in reconstructed regions of high as well as low radiotracer uptake may alter the quantification of biological indices such as the binding potential (BP) of radiotracer [142, 143]. Unfortunately, correction methods for image degrading effects are not completely straightforward, and even if accurate estimates the errors are obtained, the issue of noise propagation must also be considered. For each of the solutions discussed in this section, the extent of the problem, approaches to estimate the error as well as the application of the correction will be discussed.

2.4.1 Randoms correction

It can be deduced from Equation (3) that the detection of random coincidences depends only on the singles rates and the width of the time window, which in turn depends on the time resolution of the tomograph. Complete randoms rejection can only be achieved with perfect time resolution. However, even if the exact time of the interaction was available, a time window would still be required to avoid a reduction in sensitivity due to differences in the distance traveled, and hence the time of interaction of the two photons. Hence, despite the fact that detectors and electronics today are approaching optimal time resolution [144-147], reducing the randoms fraction (R/P) considerably, random coincidences continue to be of concern. The problem can be alleviated somewhat with the use of metal shields to block activity from areas that are not within the object of interest. More elaborate steps need to be taken to completely eliminate the blurring due to random coincidences and prevent corruption of statistics due to the application of the correction method.

Random coincidences in small animal PET

The randoms fraction in small animal PET tomographs is not expected to be very high since a small fraction of the injected dose, which itself is lower than typical human doses, ends up in the target organs. Autoradiography studies have shown that less than 1% [4] of the injected FDG dose ends up in the rat brain, and similar fractions are expected with other tracers. Nevertheless, the absence of shielding for events outside the FOV could make the randoms contribution appreciable. An approximate method to estimate random as well as scatter coincidences is the tail fitting method [148]. Since the distribution of randoms is a slowly changing function, and as long as the object does not fill the entire FOV, a paraboloid or Gaussian is fit to the tails outside the object and the distribution of "background" events. Recently, randoms have been estimated using one of the two methods described below:

Randoms estimation methods

1. **Delayed coincidence channel estimation method**

This is the most commonly implemented method to estimate random coincidences, and possibly the one least susceptible to errors in implementation. Along with the prompts, coincidences are collected within a delayed coincidence channel wherein the timing signals from one detector are delayed by a time significantly greater than the coincidence timing resolution of the system so that there are no true coincidences in the delayed channel. As the rate at which uncorrelated photons strike the detectors is the same for both channels, an approximation of the number of randoms in the prompts channel is obtained in this manner. This was originally implemented real-time in the electronics for tomographs that output histogrammed coincidence data, but can easily be applied to singles list mode data processed offline as well.

The delayed channel randoms has identical properties to the prompts channel, and while that would be considered an advantage in terms of matching dead time and efficiency, a major drawback of the approach is that Poisson noise from both channels could propagate into the reconstructed image. Revisiting Equation (4) to calculate the propagation of error from the delayed channels randoms estimate similar to Strother et al [30]:

If T, P and D are the number of true, prompt and delayed coincidences respectively such that T = P - D, and the statistical noise in P and D are √P and √D, the uncertainty in T can be given by:

$$\Delta T = \sqrt{\Delta P^2 + \Delta D^2} = \sqrt{P + D} = \sqrt{T + 2D}\ .$$

Hence, subtraction of the delayed channel estimate doubles the effective noise contribution of random coincidences to the data compared to a noiseless estimate. The problem is exacerbated at high count rates when random coincidences outnumber true coincidences. This limits administered activities, and has led to the exploration of other techniques to improve high count-rate performance of PET systems.

A number of variance reduction schemes have been proposed, ranging from smoothing of the randoms estimate to more complicated techniques summarized by Badawi et al [149] that rely on certain approximations of proportionality in the randoms for certain LORs. The goal of these methods is to bring the noise contribution due to the randoms estimate (k in Equation (5)) down to $0 < k < 1$.

2. **Singles-based estimation method**

Another method directly applies Equation (3) to obtain the randoms rates for all detector pairs [150]. This is possible only when singles rates at each detector are available, and

the time window for each detector pair is accurately known. Since the number of singles detected by a typical PET scanner are roughly 2 orders of magnitude higher than the number of prompt coincidences, the fractional noise from such a randoms estimate is negligible. The error propagation can be calculated as above from $r = 2\tau s^2$, which is a simplified expression for the singles-based randoms count rate estimate in Equation (1). Note that the variables r and s in the calculation denote count rates whereas the same letters capitalized (R and S) denote counts.

$$R = 2\tau s^2 t$$

The error in R can be written as:

$$\Delta R = (2\tau t) \cdot 2(\Delta s/s) \cdot s^2 = 4\tau t \cdot s\Delta s$$

Hence,

$$(\Delta R)^2 = 16\tau^2 t^2 . s^2 . \Delta s^2$$

Substituting $\Delta s = \sqrt{S}/t$ and $R = 2\tau s^2 t$,

$$(\Delta R)^2 = 8\tau s R$$

Therefore ΔT from Equation (4) becomes $\sqrt{T + R + 8\tau s R} = \sqrt{T + R(1 + 8\tau s)} \approx \sqrt{T + R}$

Since $\tau s \ll 1$, the additional noise contribution to the trues from the randoms estimate is minimal. Note that this calculation assumes discrepancies in the coincidence window widths between LORs are negligible.

The implementation of this idea is straightforward, as long as the singles rates used in the formula are obtained from events that have survived energy discrimination and could realistically be registered as a random coincidence. The calculation is an integral of a product (not a product of an integral) and hence sampling of the randoms estimate needs to be carried out at a sufficiently high frequency. For tomographs in which recorded singles are averaged over adjacent detectors, Brasse et al [151] included intrinsic detector efficiencies in the formula to account for the bias introduced due to any differences between single and coincident photons (due to differences in the energy spectra, dead time, pulse pile-up etc in the channels that constitute them):

$$R_{ij} = 2\tau S_i \varepsilon_i S_j \varepsilon_j \times \text{calibration factor.}$$

Some concerns that call for careful implementation of the singles based algorithm include errors due dead time, as well as to the time window for each detector pair, which could vary due to time offsets caused by trace lengths, time walk etc.

Application of correction

The online subtraction of random coincidences from the prompts generates sinograms corrected for randoms at the end of the study, resulting in a single sinogram that is corrected, on an average, for randoms contamination. However, direct subtraction of two

Poisson variables would produce a result that is not Poisson and go against the requirements of commonly used statistical reconstruction algorithms such as MLEM. Yavuz and Fessler [152] derived a logical likelihood formula to use MLEM on randoms-precorrected PET data wherein they found the likelihood for a Poisson with a mean of (P+2R) and then shifted it by -2R. This was termed as the "Shifted Poisson" approach. However, precorrected sinograms also have negative values that cause the MLEM to diverge. Setting them to zero causes a slight positive bias [153]. If the storage size of the sinogram is not an issue, the ideal approach would be to store separate estimates and properly account for the additive contamination (R) using a modification to the MLEM equation from Equation (***18***) shown below:

$$x_i^{n+1} = \frac{x_i^n}{\sum_j^{NLOR} A_{ji}} \sum_j^{NLOR} A_{ji} \frac{y_j}{\left(\sum_k^{NVOX} A_{jk} x_k^n \right) + R_j}$$

The goal of a given iteration then becomes to find the solution x that, when forward projected and added to the randoms estimate, best fits the measured projection data y.

Selection of method

Randoms estimates are an approximation of the average number of randoms and are not obtained on an event-for-event basis. Both algorithms have been shown [151, 154] to adequately estimate the mean of the randoms at typical counting rates. If the singles-based method is implemented accurately, a considerable improvement in image noise variance is expected.

2.4.2 Scatter correction

The evolution of PET technology from 2D to 3D (without septa) has caused an increase in scattered coincidences by orders of magnitude. Correction for scatter is important not just to improve the contrast of the image, but also for accurate quantitation of non-homogenous objects. It can be calculated that 50% of all 511 keV Compton interactions produce scatter with an angle of 60° or less [27]. The most likely energy and angle are ~450 keV and 35°[155]. Therefore, the use of a narrow (±100 keV) energy window about 511 keV would reject all scattered events. However, not all photons are completely stopped after the primary interaction, and since only a portion of the energy is deposited in such a case, some valid photons may not survive a tight energy cut. To avoid this reduction in sensitivity to true coincidences, it is prudent to use a larger energy window, even for systems that might have perfect energy resolution. Scanners typically use 350 keV–650 keV [55]. On the other hand, scatter is one of the most difficult issues to correct for in PET, and the use of carefully selected energy discriminators is more beneficial than the development of accurate correction methods. An optimal tradeoff between sensitivity to true coincidences and scatter rejection needs to be achieved using the right window width, and any scatter that remains can be

corrected using specialized algorithms. The problem of photon scatter has had a long history in SPECT as well as PET, and only a few key solutions will be discussed here.

Scatter fractions in small animal PET

There is not a large amount of literature on scatter correction in small animal PET since the scatter fractions are expected to be small. However, the contribution of scatter from outside the FOV could be large in some cases. Yang et al [65] recommended a wider energy window setting for rat imaging studies compared to mouse imaging in the microPET II, due to the larger scatter fraction (S/P) in rats. Ignoring the scatter in the gantry and room environments, they measured 3% and 10% scatter fractions for mouse-sized and rat-sized phantoms respectively using energy windows of 150-750 keV and 250-750 keV. The microPET Focus showed only slightly larger scatter fractions due to its larger FOV [25]. The Sherbrooke small animal APD-PET scanner includes a multi-energy-window data acquisition to fit the spatial distribution of individual scatter components of the object, collimator, and detector using simple functions. With this tomograph, the scatter fraction for rat imaging was approximated to be 33.8% according to Monte Carlo calculations [43].

Scatter estimation methods

Scatter correction methods can be broadly divided into four categories detailed below: curve-fitting methods, multiple energy window-based methods, convolution-deconvolution methods and simulation-based methods. Known principles of photon scatter that are used in the design of these approaches are:

1. Scatter has a low-frequency, slowly varying distribution.
2. The energy of the scattered photon decreases with the scattering angle.
3. An energy spectrum for 511 keV photons in tissue contains photons that have scattered multiple times in the lower energy regions, and photons that have scattered once or not at al around the photopeak.

1. Curve-fitting methods

Tail fitting is the simplest approach to scatter correction. A smoothly varying function is fit to the counts appearing outside the object, based on the assumption that any counts outside the object are not collinear with the annihilation location and have to be attributed to scatter. Karp et al [148] used a second-order polynomial, and Cherry et al [156] used a Gaussian function to fit the scatter "tails". This approach is simple and computationally efficient. It will correctly estimate scatter from outside the FOV, which is not possible with some of other methods. The main drawback is that the approximations of a smoothly varying function may not be accurate for heterogeneous regions, resulting in over or under subtraction. Also this approach may not be feasible when the object fills a large fraction of the scanner's FOV.

2. **Multiple energy window methods**

These methods were developed originally for parallel-beam SPECT [157], to reject the contribution of events that are not within the projection line. Dual energy window methods [158] are based on the assumption that the scatter within the photopeak window (say 380–850 keV) can be accurately estimated using the distribution of Compton scattered events within a lower, scatter-only window (200–380 keV). Shao et al [159] proposed an extension to the dual window technique by accounting for distribution dependencies and source size by comparison with a calibration phantom. These ideas are straightforward, but are considered to be lacking since a majority of scattered events in the photopeak window undergo only a single Compton interaction, whereas in the lower energy window multiple interactions are more common [160]. Bendriem et al [161] used a trues-only window with a very high LLD (550-850 keV) along with a wider photopeak window which included scattered events. By scaling the trues and subtracting them from the larger window, they achieved an estimate of the scatter from the same energy window as the data. The estimate was noisy because of the small fraction of counts within the trues-only window, but could be smoothed if required. More recently, the multispectral method has been developed [162], based on the acquisition of data in a very large number of equal-sized energy windows. The spatial distribution of scattered and unscattered components in each window is fit using simple mono-exponential functions. The above methods all account for scatter from outside as well as inside the FOV and work well for systems with high energy resolution.

3. **Convolution-subtraction methods**

Bergstrom et al [163] carefully measured the scatter response of a line source positioned at regular intervals (assuming spatial variance of scatter) and obtained a position-related scatter response function h(s,x), where x is the radial position of the source. This estimate was then convolved with the measured data to estimate of the scatter, which was subtracted from the measured data. In the ideal case, unscattered data would have been used for the initial convolution, but the measured data was a reasonable approximation for small scatter fractions. Other researchers used an iterative approach to obtain an estimate of unscattered data [105]. This method is fast (once the scatter response has been generated) and explicitly accounts for the shape and materials of the object. It works best for homogenous objects, since the scatter response was calculated for a uniform phantom. The scatter estimate is noise-free, but does not account for scatter from outside the FOV.

Bergstrom's original formulation was calculated in 2D, and the extension to 3D data adds a level of complexity since a 2-D scatter response defined in terms of radial (x) and axial (z) variables [164, 165] is needed.

4. **Model-based Methods**

Given a map of attenuation coefficients to represent the object, and using well-understood principles of the physics of photon interaction in matter, the scatter fraction in a particular study can be modeled. Two approaches to scatter modeling using Monte Carlo and mathematical models are discussed below.

i) Monte Carlo models

Monte Carlo models are ideal research tools for accurate modeling of photon transport, and hence, scatter. Photons are tracked through the object using information from the attenuation map, and the random chance of Compton interactions is modeled. In order to be able to accurately use Monte Carlo simulations for correction, an accurate estimate of the source and object geometry is required, which is not easy to obtain in PET studies. Levin et al used FBP reconstructions for an initial estimate of true source distribution [78]. Other researchers use attenuation maps obtained from anatomical images and incorporate them into Monte Carlo models [124].

Although Monte Carlo simulations allow maximum accuracy and flexibility in the model, they may not always be feasible due to time constraints. Researchers have developed strategies to speed up the calculation, such as the variance reduction techniques discussed earlier, and innovative sampling techniques based on the geometry of the tomograph [166]. Levin et al used a coarse sampling of the image volume for scatter estimation. This was seen to be reasonably accurate, since scatter does not have high frequency components. If simulation time and matrix storage are not of concern, Monte Carlo models with attenuation maps incorporated in them can be used to generate a reconstruction probability matrix which accounts for the combined effects of attenuation and scatter in the most authentic manner.

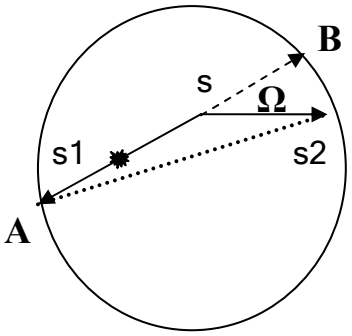

Figure 17 Single scattered photon

ii) Mathematical models

A popular class of modeling methods is based on the single scatter assumption [32, 167] that only one of the two annihilations photons undergoes a Compton interaction prior to being detected. This has been shown to be true for 70-80% of scattered events for a 76 cm ring tomograph with 10cm axial FOV using simulated data [160]. For the illustration in Figure 17 the single scatter coincidence rate for the LOR connecting detectors A and B due to one of the two photons having scattered at S has been defined by Watson et al as:

$$P_{scat}^{AB} = \int_{V_s} dV_s \left(\frac{\sigma_{AS}\sigma_{BS}}{4\pi R_{AS}^2 R_{BS}^2} \right) \frac{\mu d\sigma_c}{\sigma_c d\Omega} (I^A + I^B)$$

where V_s is the scattering volume.
μ is the attenuation coefficient of the object.
σ_{AS} and σ_{BS} are the geometric cross sections of detectors A and B as seen from S.
R_{AS} and R_{BS} are the distances from the scatter point.
σ_c is the Compton cross section calculated from the Klein-Nishina [168] formula.
I_A and I_B are the estimated attenuated unscattered emitter intensities for paths SA and SB, relative to the initial intensity I_0 given by:

$$I^A = \varepsilon_{AS}\varepsilon'_{BS}\, e^{-\left(\int_S^A \mu ds + \int_B^S \mu' ds\right)} \int_A^S I_0 ds$$

$$I^B = \varepsilon'_{AS}\, \varepsilon_{BS} e^{-\left(\int_S^A \mu' ds + \int_B^S \mu ds\right)} \int_S^B I_0 ds$$

The primed variables are calculated at the scattered photons energy and the total intensity (I_A + I_B) takes into account the fact that the scattering event could occur along either of the two paths. While a thorough explanation of the above formulae is beyond the scope of this manuscript and is available in [32], the components of the equation can be understood as an integration over the volume V_s of:

1. the geometric probability of detection (based on solid angle) by detectors A and B for an event scattered at S.
2. the probability of scattering at point S through angle Ω, calculated from the Klein-Nishina formula.
3. The attenuation of the initial intensity (taking into account the intrinsic efficiencies of the detectors).

Ollinger et al [31] derived a similar formula, but also extended it to multiple scatters by convolving the single scatter distribution with a one-dimensional kernel [169]. Moreover, they solved the problem iteratively, rather than assuming the intensity of the true processes from the image without scatter correction. Another drawback of the Watson method, i.e. scatter from outside the FOV (OOFOV) was also addressed by Ollinger by incorporation of information to model the OOFOV regions. This yielded images with an accuracy equivalent to 2D imaging.

The obvious advantages of SSS methods are the statistical quality and the precision of the scatter estimate. Barney et al [170] successfully demonstrated the accuracy of the above models by comparing them with Monte Carlo simulations. The main drawback of both the above approaches is simulation time. Nevertheless, these are among the most popular scatter correction approaches and have found widespread use, with or without optimizations [28, 171, 172], in clinical PET tomographs.

Application of correction

Similar to randoms, subtraction of the scatter from the prompts sinogram should be avoided. Ideally, scatter would be incorporated into the probability matrix but since this is often not feasible, the estimated scatter component is included with a forward projection of the reconstruction, similar to the randoms.

Selection of method

The selection of a scatter correction method depends upon the uniformity of the object being imaged, and its size relative to the tomograph's FOV. For neurological studies with a fairly low scatter fraction within a homogenous object, simpler estimates such as tail fitting might be sufficient. For more robust calculations in complex objects such as the thorax, model-based methods would produce images with higher accuracy, at the cost of time.

2.4.3 Attenuation correction

As discussed in 2.1.1B, attenuation correction methods in PET estimate the probability of attenuation for each LOR, and are not affected by the location of the decay within the LOR. Attenuation correction is essential when tissues of varying thicknesses make up the objects anatomy, since this may inhibit the detection of certain regions lying below denser regions.

Attenuation correction for small animal PET tomographs

The impact of attenuation in small animal tomographs is usually relatively minor, and a global scale factor is often considered to be sufficient [173]. Although this is known to produce a "cupping artifact" (due to the fact that the same correction factor is applied to all LORs, but the central LORs traverse through more material) the error may be negligible for small objects. Chow et al [174] compared the global scale factor with two other standard approaches described below (transmission source-based [175] and CT-based [176]) in terms of noise and accuracy using microPET data. They summarize that transmission source-based methods result in images that are noisier than the uncorrected data. Additionally, these methods substantially increase scan times and anesthesia exposure. Using optimized, post-injection CT-scanning, registration and scaling protocols, they obtained images with a high level of qualitative and quantitative accuracy. More details about the two approaches are provided next.

Overview of approaches

1. **Global correction factors**

When imaging regions of uniform attenuation dominated by soft tissue such as the brain and abdominal areas, a basic distribution can be approximated from the emission data

by determining the body contours [177] using empirical or automatic edge detection methods and a global attenuation coefficient can be applied to the reconstructed object. Reliable methods of attenuation correction for more complicated objects require the spatial distribution of linear attenuation coefficients for the object being imaged, called the attenuation map, discussed below.

2. **Estimation of attenuation map**

The attenuation map can be obtained by comparing the count rates from an external transmission source with the count rate of the same source when the subject is not in the tomograph. Historically, ^{68}Ga/^{68}Ge ring sources have been used [178, 179] where one of the two annihilation photons is detected after it traverses through the object. For large systems, this can be a noisy measurement. Continuously rotating rod sources [180] gained popularity for a few years to estimate attenuated projections. When the high count rates of the rod sources, especially towards the edges, were observed to increase the scatter, Derenzo [51] suggested using a point source in singles mode, i.e. shielding the near detector from it. The source was rotated along the patient and translated axially, and LORs were formed between the source position and the far detector. This technique was especially useful for 3D tomographs. Currently, ^{137}Cs is a popular singles photon source for transmission measurements [181, 182], though the correction requires a calibration for the 662 keV photon energies. Single photon counting has been shown to be more efficient, but also more prone to the effects of photon scatter.

Typically, transmission scans take ~20 mins and are carried out before [182], during [183] or after [184] the PET study. Long transmission scans are required for good statistical quality. Alternatively, segmentation and tissue classification are used to separate regions from low-statistics transmission measurements and uniform attenuation coefficients are applied them [185, 186]. Transmission scanning is available on most commercial clinical and preclinical PET and SPECT scanners since it is a relatively simple correction to implement, but makes a dramatic improvement to the quantitative accuracy of the study.

With the advent of sequential PET-CT scanners, followed by simultaneous scanners during the late 90s, investigators have explored the use of CT-based attenuation correction methods [176]. CT images contain pixel values that are related to the linear attenuation coefficient μ, calculated for x-ray photon energies. These could then be scaled to 511 keV coefficients and applied to PET images, or alternatively segmented into uniform tissue regions and assigned standardized μ values for those tissues. Kinahan et al [187] pointed out that a scaling factor may be required to account for the fact that there is a larger fraction of photons undergoing photoelectric interactions at X-ray energies of 80 keV compared to 511 keV and that this fraction changes depending on the type of tissue. Hence they used different scaling factors for soft-tissue regions compared to bony regions.

The advantages of CT-based corrections are that CT images have higher resolution and statistical quality compared to PET transmission measurements, within shorter acquisition times. In the past, accurate image registration was a problem, and the use of fiducial markers [188] was common for offline alignment of the images to obtain attenuation maps registered to the PET data. Complications involving coregistration [189] have been eliminated with the new generation of simultaneous PET-CT scanners.

Finally, attenuation correction using MRI images is a new area of research. Zaidi et al [190] used fuzzy clustering to distinguish separate attenuation regions in MRI images, then classified them into bone, brain, cavities etc and assigned tissue-dependent attenuation coefficients. This could be a promising alternative to transmission sources in the latest generation simultaneous PET-MRI systems.

Application of attenuation correction

The forward projected attenuation map, followed by exponentiation, is a sinogram of Attenuation Correction Factors (ACFs) which can be applied as a multiplicative factor to the measured data before or after reconstruction. Data is corrected for scatter prior to attenuation. As with scatter, ideally, attenuation factors would be integrated with the probability matrix.

2.4.4 Dead time correction

In an ideal PET system, the detected true count rate should increase linearly with the activity in the FOV. Dead time is highly dependent on the design of the system, time taken by coincidence circuits, multiplexing etc. The primary factor that affects dead time is the integration time of the detector. If a photon deposits energy in the detector while a charge is still being integrated from a previous event, there are two possible outcomes – it either results in a collective charge that is higher than the ULD, or the two are treated as one, with incorrect position and energy. Dead time can be paralysable, wherein each subsequent event arriving while the system is unresponsive contributes an additional dead time eventually leading to system saturation, or nonparalysable, in which events detected while the system is "dead" are ignored. A decaying source experiment is used to measure dead time, using a uniform source of a known quantity of fast decaying tracer. Repeated measurements are made and plotted as the source decays. Since the detected count rate should be proportional to the activity, the expected count rate without dead time can be extrapolated from the detected count rate at low rates.

Correction for dead time

The easiest correction method involves generating a look-up table of correction factors derived from the decaying source experiment. However, variations in the source distribution could change the relative count rates at individual LORs. In practice, combined correction factors are obtained for each LOR using measured data as well as calculations

from known issues in the system architecture [191, 192]. Dead time models for paralysable as well as nonparalysable cases have been evaluated. Since dead time correction methods were not deemed necessary for the RatCAP, these are not discussed here.

2.4.5 Normalization

Normalization is a correction for non-uniformities due to variations in the sensitivities of individual crystal due to

- Differences in intrinsic crystal efficiencies
- Variation in gains
- Geometry and arrangement of detectors, positions of crystal within block

The extent of this error depends on the number of detector pair combinations for a particular system, and the degree of variability between them.

Estimation of normalization coefficients

A **direct** method to obtain normalization coefficients (NCs) for each detector pair involves acquiring a high statistics dataset of a phantom with a known distribution that illuminates all the LORs for a given projection angle. If a homogenous phantom that fills the tomograph's FOV is used, the reciprocal of the attenuation and scatter-corrected sinogram of the phantom is normalized for a gain of unity to obtain correction factors. For the various source distributions used to determine the correction, the expected "ideal" response must be factored out. Researchers have used rotating rod sources [179] in 2D [193] or 3D [194] for high statistics normalization factors, as well as ring sources for which all projections can be acquired simultaneously. One of the disadvantages of rods is that if high enough count rates are used for practical scan times, the issue of high scatter at the edges needs to be solved. With narrow ring sources, it is hard to determine the shape of the expected projection because the point spread functions vary along the lines of response. Various other source designs have been explored including plane sources (or moving line source bailey[195]) and cylindrical sources [196].

Problems with the direct normalization approach are listed below:

1. For 3D PET scanners, noise-free data can only be obtained with long acquisition times, especially since low rate data is preferred to minimize randoms and dead time [197]. If the NCs do not vary with time, a one-time high statistics scan per imaging system is feasible. This is certainly true for geometric factors, but may not account for intrinsic crystal effects.
2. Scattered coincidences and true coincidences have been shown to have different NCs [198], which bias the correction.
3. The sources must have very uniform concentrations to avoid biasing the data.
4. Dead time effects change apparent efficiencies

A faster, robust alternative to direct methods is the component-based normalization technique, originally developed by Hoffman et al [199]. NCs for true coincidences within a particular LOR AB in a block detector system are expressed as a product of the factors in the equation below:

$$NC_{AB}^{true} = \varepsilon_A \varepsilon_B c_A c_B t_{AB} g_{AB}^{trans} g_{AB}^{axial} m_{AB}$$

where ε is the intrinsic efficiency of the detector, c is the block profile factor which describes the systematic variation in efficiency based on the placement of a crystal within a block detector, t represents the time window alignment factors [149], g^{trans} and g^{axial} are the transaxial and axial geometric factors, and m represents the structural misalignment factors. Each component is categorized as variable (changes with time and should be part of routine maintenance) or fixed. Typically, geometric factors are considered to be fixed, and intrinsic efficiencies of crystals are variable. This model reduces the number of counts required in a normalization measurement by separating the individual detector efficiency contributions from LOR efficiencies since there are fewer detectors than LORs. Other normalization factors are computed by averaging over multiple LORs and optimizing symmetries similar to probability matrix generation strategies. A separate dead time correction is applied to count rate-dependent factors.

Several variants of the component-based normalization method, especially the estimation of intrinsic detector efficiencies have been optimized and validated by researchers [57, 200]. Visser et al [201] evaluated the component-based method provided with the Siemens Inveon with a focus on image noise and found that a scan of 10 min produced images with an equivalent level of accuracy compared to a 10h direct normalization scan. For non-commercial implementations, however, the estimation of individual factors with optimized statistical quality might be complicated to obtain. Bai et al [202] developed a unified model to estimate all factors simultaneously within a maximum likelihood framework and have shown positive results.

Application

Normalization is most commonly applied after data has been binned into a sinogram. A new method has been shown to have better noise properties, wherein NCs are applied event by event during the binning process [203]. As with the other correction factors, incorporation of NCs into the system model is considered to be the optimal approach.

2.4.6 Calibration

For PET to be recognized as a useful quantitative tool, it is necessary to accurately calibrate the reconstructed, corrected images in units of activity per unit volume. Calibration

in this manner would allow the end user to correlate different studies with varying injected doses. Reconstructed images are usually cross calibrated using the ratio of ROI values in a high statistics phantom study to measured values of aliquots of the same tracer solution in a calibrated well counter.

Section Conclusion

It is apparent from the above overview that quantitation in PET is a vast, continually developing field. Although none of the problems encountered in PET have ideal solutions, it is possible to optimize imaging protocols to achieve accuracies within a few percent for well-defined tasks.

3. RatCAP - Techniques and Validation

3.1 Introduction to the RatCAP (Rat Conscious Animal PET)

An introduction to the RatCAP tomograph was provided in the Overview (Section 1) at the beginning of this dissertation. This subsection focuses on the design and development of two generations of the system.

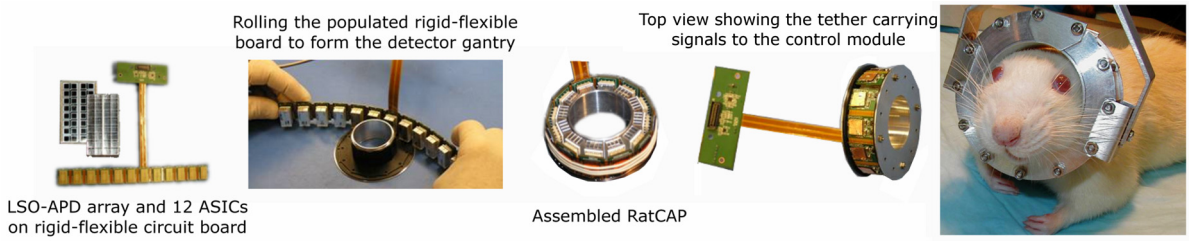

Figure 18 RatCAP parts and assembly

3.1.1 System design and design goals

The RatCAP detector block is a 4x8 array of LSO crystals individually coupled to an APD array with a 93% packing fraction. The crystals are 2.22 x 2.22 mm in size and 8 mm in length (or 5 mm in case of the first generation system). Each detector block is equipped with a custom Application Specific Integrated Circuit (ASIC) [204] which consists of 32 channels each comprising a charge sensitive preamplifier, a pole-zero network with 32 programmable gain settings, a 3rd order bipolar Gaussian shaper, a zero-crossing discriminator (ZCD) for time pick off and a programmable energy discriminator. Details and block diagrams for the chip are in [204]. Twelve such composite detector blocks are placed on a rigid-flexible printed circuit board (PCB) which is rolled to form the detector gantry as shown in Figure 18 such that the inner circumference is a continuous polygonal ring of crystals with an inner diameter (and imaging FOV) of 3.84 cm and axial length of 2 cm. This is sufficient to cover the entire brain of the rat when placed just below the harderian glands.

The data flow chain is illustrated in Figure 19. Detected events from the channels of each ASIC are transmitted on a single multiplexed serial line. 12 such data lines are routed along the flexible circuit to a control module, and then via flexible ribbon cable to a specialized module called the TDC and Signal Processing Module (TSPM) [205, 206]. Calibration signals, connections for high voltage (HV) to bias the APDs and power for the chip are transmitted

on a reverse path along this line. The TSPM consists of a Field Programmable Gate Array (FPGA)-based time to digital converter that time stamps each singles event and packages the time and position information for readout. Data is transmitted to a standard PC via optical fibers (required for signal integrity in an MRI environment) through a PCI card. Singles list mode data is stored and processed for coincidences using offline software. Each event is 8 bytes in size, and a typical PET study with a 500 μCi injection scanned for about an hour results in images of ~2GB. Images are reconstructed using MLEM with a Monte Carlo-based probability matrix [207] that takes advantage of the small size of the imaging FOV and small number of detectors.

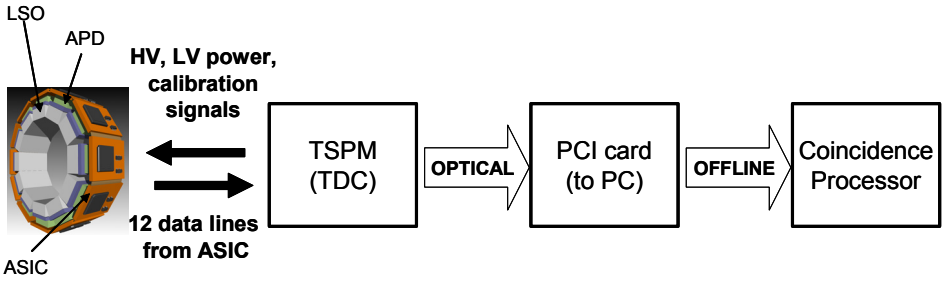

Figure 19 RatCAP data flow diagram

Some design goals unique to this system that have been successfully accomplished are:

- The complete system has the dimensions of 8 cm outer diameter * 2.6 cm length. This is small enough to not obstruct the animal's vision, whiskers or interfere with other senses.
- The system weighs less than 200 grams. The weight is counterbalanced so that the animal has only to overcome the inertia of the device to move. Full freedom of movement, including rotation, is provided.
- The system has low power requirements (<2W) to avoid overheating, since the APD gains are sensitive to temperature fluctuations. Temperature also needs to be controlled for animal comfort. In order to limit power dissipation, the system does not have ADCs, and does not measure the energy of the photons. The only available information for output is the report from the discriminator. The consequences of this are discussed in [208].
- The entire electronics design including routing of signals has been accomplished within the limited area provided.

Expected problems

- Low geometric sensitivity: The main consequence of making the system small and light is the loss of sensitivity due to the small number of detector elements (and axial size) compared to standard preclinical PET systems. Simulated and measured sensitivity values will be reported in the latter sections of this manuscript.
- Parallax: Although increased sensitivity can be achieved by the fact that the object fills the space between the detectors, maximizing the solid angle for detection, this results in significant errors due to crystal penetration towards the edges of the FOV. With 8 mm thick

crystals, parallax causes a broadening of the LOR by 3.5 times at the edge of the FOV compared to the center.

- High background events: Since the RatCAP images only the brain of the rat, and side shields have been avoided to control its weight, the system is susceptible to high fractions of random coincidences and scatter from other organs outside the FOV. Figure 20 shows the measured randoms fraction as a function of axial location for a typical RatCAP study with a 0.8 mCi injection.

All the issues mentioned above can be corrected to a large degree, or at least compensated for using an accurate iterative image reconstruction approach.

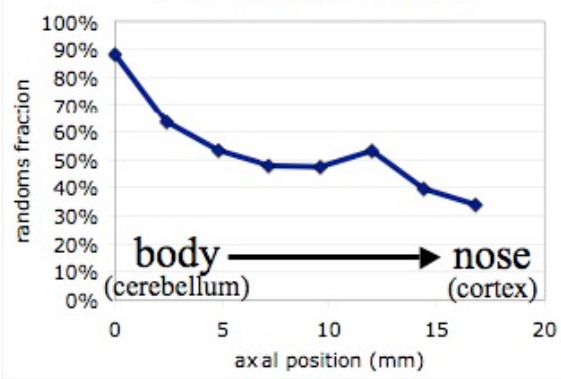

Figure 20 Expected OOFOV randoms contribution to RatCAP images. From [7]

Comparison of first generation and second generations of the RatCAP

1. **ASIC (improved energy discrimination)**

The ASIC for the first RatCAP prototype had a common energy discriminator for all 384 channels, leading to a large variation in applied energy windows owing to the ~20% variation in gains across channels. The ASIC underwent a complete redesign in 2007 and now includes programmable gains for each amplifier (over a range of 2.7:1 in 32 steps), and an optional upper discriminator threshold, The ASIC also has lower noise and is equipped with electrostatic discharge protection.

2. **TSPM (improved timing and dead time)**

Another notable development with the 2nd generation RatCAP was the new firmware logic implemented using tapped delay lines [205] which achieves a bit resolution of less than 600 ps to allow fine-tuning of the time window described in Section 3.2.2.

Also, the VME-based data acquisition system of the first prototype was capable of achieving rates of ~1Mcps/block with an accuracy of <1.1ns, which would permit studies of 30 μCi without significant dead time. Since this system was also bulky and consisted of obsolete components, a new idea was implemented consisting of an optical link from the TSPM to a computer via a standard PCI card. Higher data rates of 70 MB/s (or 10M counts per second) are now achievable, and dead time is not an issue for typical PET studies as demonstrated later in this work.

3. **Support system (improved mobility)**

The weight of the first generation RatCAP was supported from above by a tether on a counterweighted pivoting arm attached to a rotating "Ratturn" bowl shown in Figure 21 (left). Last year, a completely different concept was developed to further improve the mobility of the animal and eliminate the problems caused by the cable twisting in the previous design. It consists of a linear telescoping structure almost 1 m in length, supported

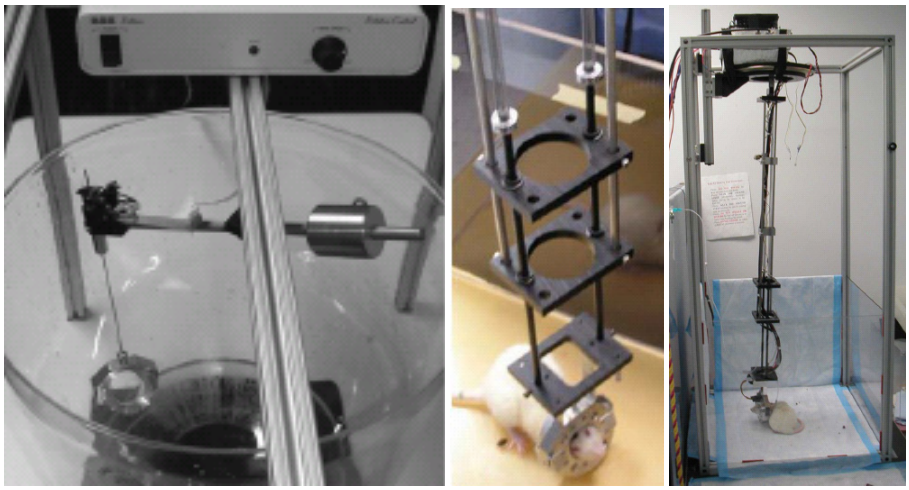

Figure 21 RatCAP support systems

The (left) Ratturn bowl and the new spring loaded system showing (center) holes for the cables (right) leading to the TSPM board placed on top

by loose springs. Figure 21 (right) shows the holes in the structure through which the cables are routed upwards to the data acquisition board which is placed on a horizontal support at the top. The entire structure freely rotates about its axis and pivots at the top in all directions while the cables remain mostly stationary. This seems to be even less obstructive than the previous design, and is tolerated well by awake animals.

3.1.2 Monte Carlo system model

A brief description of the RatCAP Monte Carlo system models and the efforts taken to model the realistic system response is presented in this section. Since the reconstruction and quantitative correction methods discussed in the following sections depend on the accuracy of this model, attempts have been made to ensure a faithful match with respect to the geometry and materials of the RatCAP, positron physics and the physics of photon transport. Two modular Monte Carlo packages designed specifically for PET and SPECT have been evaluated, namely SimSET (SIMulation System for Emission Tomography) and GATE (Geant4 Application for Tomographic Emission). They allow the user to customize the design and materials of the system, the object, the source distribution and sinogram binning parameters. Some useful features that are common to both packages include:

- Modeling of the physical processes associated with PET, including positron range, photon noncolinearity and photon attenuation and scatter derived using material properties and particle energies.
- Definition of detector material (LSO in our case), metal and/or plastic, radioactive isotopes, phantom materials (or brain tissue for rat brain simulations).
- Custom modeling of complex phantoms using image-based inputs.

GATE offers additional advantages including modeling of:
- Time-dependent processes (randoms, dead time, time-varying tracer kinetics).
- Exact geometries such as block detectors, dual-layered detectors.
- Detector cross-talk, dead time and pileup.
- Optical photon tracking.

GATE is a general-purpose Monte Carlo package with origins in high energy physics. It is versatile and provides more flexibility with object, source and detector modeling compared to SimSET. However, SimSET is more efficient since it is optimized for PET/SPECT applications. It is at least an order of magnitude faster than GATE, even without the use of variance reduction acceleration techniques, as discovered by us as well as other researchers. Investigators at Johns Hopkins have combined the strengths of the two packages by using SimSET to expedite the generation and tracking of photons [209, 210], and GATE for the complex detector modeling. In case of the RatCAP, both packages have been evaluated individually. It must be noted that time-dependent processes and block detectors were not available with the version of SimSET that we used, but a new release includes these in limited capacity.

1. **SIMulation System for Emission Tomography (SimSET)**

SimSET v2.6.2, released in 2001, was used to model the RatCAP. The individual modules and the tools provided by SimSET to construct them are described below.

Modified Block Detector Model

Since the package provided only cylindrical ring detector geometries, it has been modified to simulate discrete detector elements and block detectors. A grid of rectangular crystals organized in evenly-spaced blocks is placed over the cylindrical PET detector model provided by SimSET [121]. Events that fall within a block are assigned to a crystal based on their x and y locations. Events that do not fall within the block are rejected. Future upgrades to this model will use the latest release v2.9 (2009) which supports block detector modeling.

Source and Object Definition

The dimensions and discretization of the object are defined in the user-configurable photon history generator parameters file provided by SimSET. Activity and object distributions are defined in separate binary image files with the same discretization.

Physics model and signal processing

The isotope and object material are defined so that the software accurately accounts for positron range. Photons with a minimum energy of 50KeV are tracked, and their noncolinearity accounted for. The energy thresholds used for the RatCAP are applied after blurring the photon's energy by the system's energy resolution. A separate counter for scatter is enabled. Importance sampling is turned off for maximum authenticity.

Output

Data is binned into standard sinograms similar to measured data from the RatCAP. Scatter-only sinograms are output along with trues + scatter sinograms. Random coincidences are not accounted for, since time-dependent behavior is not modeled.

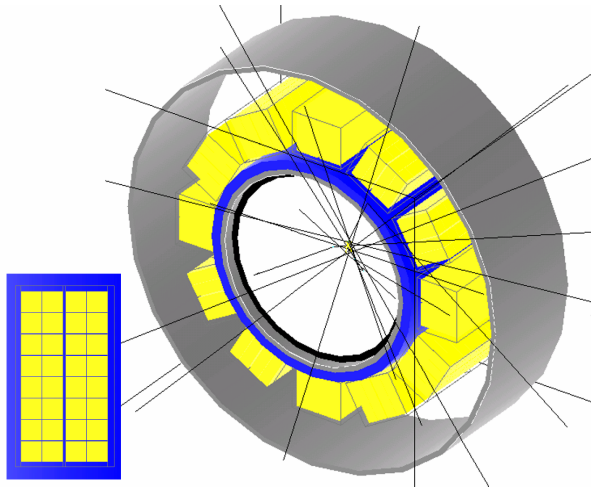

Figure 22 RatCAP Monte Carlo Model using GATE

2. Geant4 Application for Emission Tomography (GATE)

GATEv3.0.0 opened up new possibilities for accurate modeling and algorithm testing due to its advanced features described below:

Modified Block Detector Model

Block detectors are modeled accurately by modeling a single block, including the spacing between detector crystals, and then arranging 12 copies of it in the form of a ring as shown in the graphic in Figure 22 (also provided by GATE). The inner aluminum ring is surrounded by a ring made of delrin, followed by the detectors and finally the outer aluminum ring. For versions of the RatCAP with shorter crystals, the spacing between the front faces of the detectors and the ring could easily be simulated.

Source and Object Definition

The sources and objects are defined as continuous shapes by selecting them from a list of standard shapes, or by using voxelized inputs. The activity within the source could be defined in MBq or mCi, and the number of counts depended on the length of time selected for the simulation.

Physics model and signal processing

As with SimSET, the isotope and object material are defined so that the simulation accurately accounts for positron range. Photons with a minimum energy of 50KeV are tracked, and their noncolinearity accounted for. After detection, a series of signal processing steps known as the "digitizer" mimic a real detectors signal processing steps to convert photon interactions into counts. The digitizer includes energy and time blurring and windowing, and dead time and pile up effects.

Output

Singles list mode ASCII output files are processed using the standard RatCAP binning algorithms. These were consistent with coincidence list mode files output by GATE, wherein two singles in coincidence with different event IDs were counted as random. Since scattered photons were tagged as well, an estimate of the trues, randoms and scatter could be obtained.

Crystal length	GATE (T + S)	SimSET (T + S)
5mm	0.31217	0.324
8mm	0.70123	0.768

Table III Comparison of simulated coincidence sensitivities using GATE and SimSET

Validation of models

Table III compares the simulated coincidence sensitivities at 350KeV for a point source placed in air at the cFOV. The results show that there is a good match between the two models, and differences can probably be explained by the fact that the true block detector model using GATE detects a slightly smaller fraction of events. Both models were also validated against measured data from the RatCAP and the results are reported in Section 4.1. Very similar sensitivity and resolution properties were observed throughout the transaxial FOV for point sources stepped radially away from the center in Figure 24. The figure shows a cross validation between SimSET and GATE using a previous RatCAP design, as well as a comparison of a SimSET simulation with recently measured data, since GATE model for our current system does not exist. Since the placement of the source was done manually on a best-effort basis for the measured data, the inconsistency in source location is attributed to human error. Axial sensitivity simulated using SimSET was also consistent with expected values as shown in Figure 23.

Selection of Monte Carlo package

Since equivalent levels of accuracy are achieved using both packages, the more efficient SimSET is used at the core of our reconstruction and for a majority of our simulations, whereas GATE is used for tasks that are less demanding computationally, but take advantage of its power. These include validation of randoms and multiple correction algorithms, complex phantoms designed using anatomical atlases etc.

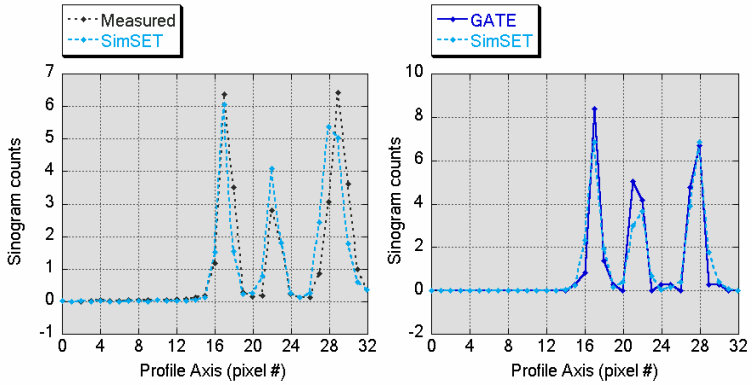

Figure 24 Cross validation of SimSET and GATE sinograms using 3 point sources placed at 17, 22 and 28 where (17,17) is cFOV

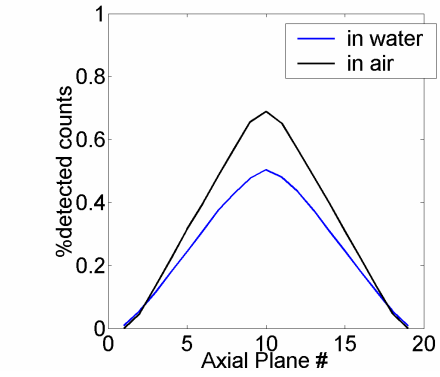

Figure 23 Simulated axial sensitivity profile in water and air

3.2 Data Acquisition and Processing

The RatCAP data processing chain begins with the singles list mode data file, which consists of 1 MB buffers of singles events. Each buffer contains 131072 x 8-byte events, each packaged into a 64-bit word: 39 bits for the timestamp with 10 ns resolution, 6 bits for the "fine" timestamp, 4 for block address, 5 for crystal address and the rest for other identifying information. Basic data integrity checks have been performed on decoding the data to ensure Poissonian timestamps, fix known irregularities and correct for rollover of the clock after a period of 91 minutes. The consistency of the data is checked on a regular basis, along with energy and timing recalibration, as prerequisites for coincidence processing. A comprehensive review of the steps involved is presented in this section.

While the RatCAP system has undergone numerous upgrades over the years, a distinct separation point was the major ASIC upgrade [204, 211]. Since data processing methods differed slightly prior to this development, a version number (1 or 2) will be used in this section to identify the system used.

3.2.1 Energy calibration

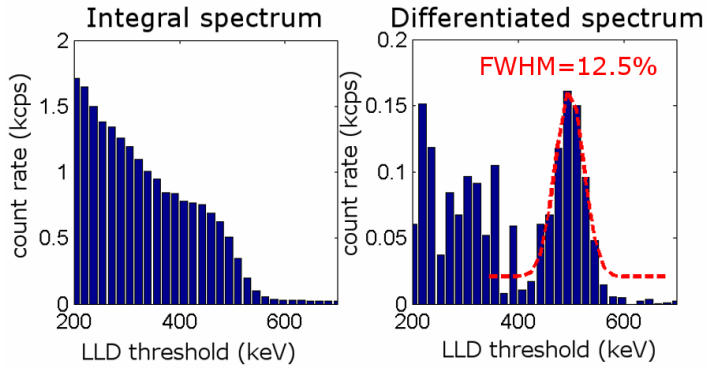

Figure 25 Energy spectrum for a single channel of the RatCAP

Selected channel has energy resolution equal to the average energy resolution of the system. The measured integral spectrum on the left is differentiated to visualize the photopeak on the right

A. Selection of discriminator thresholds

To meet the design goal [7] of reduced power consumption to prevent excessive heating, ADCs were not implemented in the RatCAP ASIC. The programmable discriminator thresholds facilitate energy gating on the chip, but since the energy of the interaction is not reported, visualization of energy spectra requires a special "threshold scan". This involves the acquisition of multiple data files as a function of the lower level discriminator (LLD) threshold as it is varied from the baseline till beyond the photopeak. The resulting count rate vs. LLD plot is the integrated energy spectrum shown in Figure 25 and

needs to be differentiated to visualize the photopeak. An average energy resolution of 12.5% over the 384 channels was observed.

Threshold scan, photopeak alignment and gain programming procedure:

1. Since APD gains vary as a function of the applied reverse voltage, select the operating high voltage (HV) such that all photopeaks are visible within the dynamic range.
2. Acquire singles data files by stepping the threshold voltage from the baseline through the complete range and plot count rates vs. LLD per channel (see Figure 25).
3. Differentiate integral spectrum from above and fit the photopeak for all channels, save locations of centroids.

At this point, for RatCAPv1, the lowest energy photopeak was determined and the common LLD for all channels was set to 3σ below it, where σ is the standard deviation of the photopeak. This resulted in a 20% FWHM variation in the relative energy threshold across channels, as low as 150 keV for those with high gain.

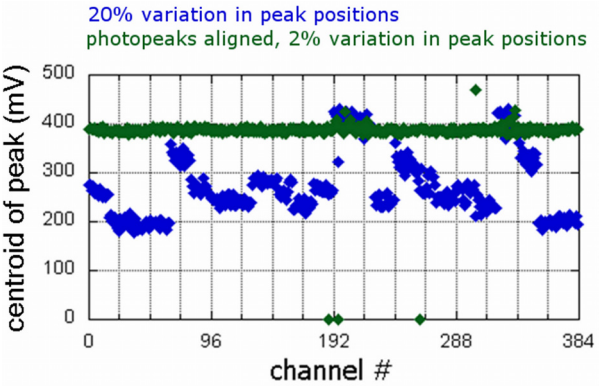

Figure 26 Photopeak positions before and after gain adjustment for individual channels

Since the ASIC-v2 allowed the programming of individual gains for each channel, an initial threshold scan was carried out with gain=1 for each channel. From the centroid locations, the gains could be adjusted so that all peaks were aligned in the best possible location to maximize the dynamic range of the system. This was done as follows:

4. Determine the ideal operating HV such that the highest photopeak maximizes the dynamic range with all gains set to 1.
5. Set gains for individual channels to align all photopeaks at 3σ from the baseline.
6. Set the LLD at predecided value, approximating the mean of the centroids for all channels as 511 keV. Currently, an LLD of 350 keV has been selected for RatCAP studies. No ULD is used.

Figure 26 shows the distinct 12-block structure due to varying APD gains resulting in a 20% variation in peak positions. The green series shows the aligned photopeaks, with a significantly smaller variation.

The dramatic improvement in system energy resolution by adjusting the relative photopeaks so as to enforce a uniform threshold is apparent in Figure 27 (left). Due to the tight energy

window that is now possible, the programmable gains allow for a more uniform discrimination between scatter and the photopeak events. Figure 27 (right) shows Monte Carlo-simulated scatter sinograms of a point source placed in water for the LLD settings used for both versions of the system. The gain for each channel of RatCAPv1 was modeled into the simulation, which shows a (>60%) larger scatter fraction for RatCAPv1.

Another important step is to control the temperature for RatCAP measurements since the APDs are sensitive to temperature fluctuations and the photopeaks are seen to shift by 3% per degree change in temperature.

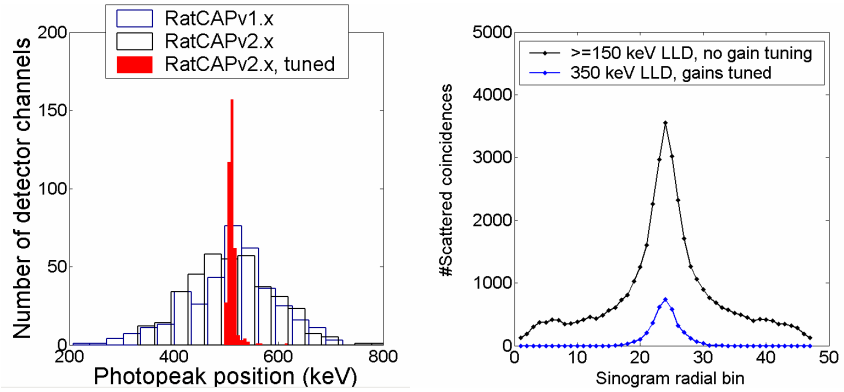

Figure 27 Energy resolution and scatter rejection after photopeak alignment (left) Reduced variation in photopeak locations, enabling the use of a tighter energy window and (right) Demonstration of improved scatter rejection ability using simulated scatter sinograms for a point source in water at cFOV using the settings for RatCAP v1 and v2

3.2.2 Timing calibration

A. Fine time resolution calibration

The 100 MHz clock provides a bit resolution of 10 ns. As mentioned in the previous section, finer resolution is obtained for RatCAPv2 using a tapped delay line logic in the FPGA firmware [205]. The calibration of this firmware involves the observation of the distribution of these fine TDC bins within a clock period. Each fine timestamp bit was empirically determined to have a resolution of 556 ps.

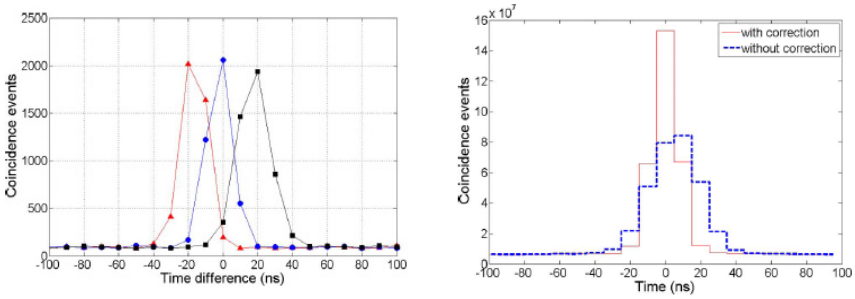

Figure 28 Correction for time offsets from [212] (left)time spectra for three coincidence channels showing t_0 offsets and (right) improvement in timing resolution from 36 ns to 23 ns after correction for RatCAPv1

B. Time offset delay correction

Issues such as baseline variations in the ASIC triggering circuits, gain variations among channels etc cause the signal arrival time among detector channels to vary greatly due to time walk. Since each individual channel has an inherent offset delay, the combined delay of two detectors in a coincidence channel results in a large number of variations in the arrival time (or t_0) of each coincidence as shown in Figure 28 (left). These offsets broaden the overall system coincidence timing resolution, and would require the use of a time window large enough to accommodate them all, resulting in an increased randoms fraction. To achieve the best timing performance, these offset delays (henceforth called t_0 offsets) are measured and corrected using a robust linear least squares approach developed by Park et al [212] for the RatCAP. The idea is to employ Singular Value Decomposition (SVD) to derive the individual channel time offsets (t_i) from the offsets measured in the set of coincidence time spectra. The relation in ***(17)*** is used where Δt_{ij} denotes the time offset for each coincidence pair.

$$A_{MxN} \bullet x_N = B_M$$

$$\begin{bmatrix} 1 & -1 & & \dots & & 0 & 0 \\ 1 & 0 & -1 & \dots & & 0 & 0 \\ : & & & \dots & & & : \\ : & & & \dots & & & : \\ 0 & & & \dots & 1 & 0 & -1 \\ 0 & & & \dots & & 1 & -1 \end{bmatrix} \bullet \begin{bmatrix} t_1 \\ t_2 \\ : \\ : \\ t_{383} \\ t_{384} \end{bmatrix} = \begin{bmatrix} \Delta t_{12} \\ \Delta t_{13} \\ : \\ : \\ : \\ : \\ : \\ \Delta t_{382,384} \\ \Delta t_{383,384} \end{bmatrix} \qquad (17)$$

This is a linear expression in the form $A_{MxN} \cdot x_N = B_M$ where M is the total number of coincidence pairs (72,192) and N is the number of detector channels (384). B is the column vector containing the centroids of the time spectra, x is the column vector of the individual channel delays to be calculated and A is the matrix of coefficients to relate the two. The inversion of A is performed using SVD to derive the values for x.

Procedure for t0 offset correction

Coincidence data for the time spectra are typically acquired using a high statistics measurement of a uniform phantom which fills the entire FOV activity. Individual time spectra are binned and fit to Gaussian functions, and Δt is determined from their centroids. For the data shown in Figure 28, the histogram of Δt had an FWHM of 0.84 ns. Matrix A is arranged so as to correspond to the measured Δt vector. Using SVD from the GNU Scientific

Libraries (GSL), the 53MB matrix A is decomposed and inverted within 10 minutes. The t_0 offsets for each of the 384 channels are obtained by a simple multiplication of this inverted matrix with the Δt vector. The result for RatCAPv1 (10 ns bit resolution) from [212] is shown in Figure 28. The power of this approach, however, is more evident with the use of the fine time bins in RatCAPv2, which allowed the tuning of each channel more accurately to obtain an improvement in overall system timing resolution of 13.5 ns as shown in Figure 29. The resulting 9 ns overall resolution is close to the average resolution (8.5 ns) of a single channel. This allowed the use of a coincidence time window τ of ±9 ns for optimal randoms rejection in all LORs.

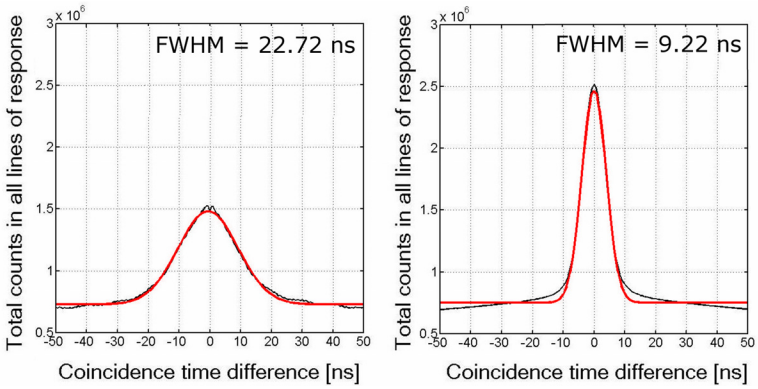

Figure 29 t_0 offset correction for RatCAPv2 showing an improvement in overall system timing resolution from 22 ns to 9 ns

Dependence of timing on LLD

Data was acquired using ^{68}Ge rod sources at 250, 350 and 450 keV to determine the influence of the LLD on system timing. The mean values of the t_0 offsets (ns) and time resolution FWHM (ns) were plotted for all LORs. The t_0 offsets were seen to be independent of LLD, but the time resolution improved significantly with higher energy cuts. The plot below shows that the selection of timing and energy windows is not trivial, and a metric known as Noise Equivalent Count Rate (NECR) is used to optimize the same in Section 4.1.

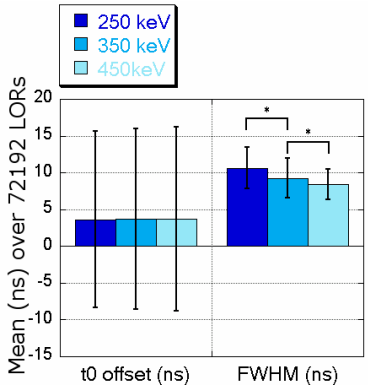

Figure 30 Increasing LLD results in a significant improvement in the time resolution but does not affect t0 offsets

3.2.3 Coincidence sorting and binning

Since the ASICs report their data through a serial line to the TSPM, the sequence of singles events is usually out of order at small time scales, although the time stamps are generally monotonic on a macroscopic scale. Singles events are sorted according to their timestamps prior to coincidence checking using a sliding window to avoid sorting large data buffers at once. This is achieved by the Standard Template Library (STL) associative container, Set, that maintains a sorted list of unique objects. The sliding window is made large enough to accommodate events within the coincidence window and delayed window (see Section 3.4.2) but not too large for optimal processing. This allows for the implementation of a relatively simple coincidence processor which compares the timestamp of each event with that of the next. If the difference is larger than the coincidence window of 2τ, it is guaranteed that the event is not in coincidence with any other. A counter in the appropriate bin in the sinogram is incremented for each valid coincidence. If more than 2 events are detected within the window, they are rejected and a multiple coincidence counter is incremented. An estimate of random coincidences is obtained using the delayed coincidence channel as described in 2.4.1. The program outlined in Figure 31 outputs prompts and delayed sinograms; along with diagnostic tools such as crystal hit maps, time spectra, energy spectra from the thresholds scan set of data files and count rate logs. An option to bin dynamic sinograms is provided.

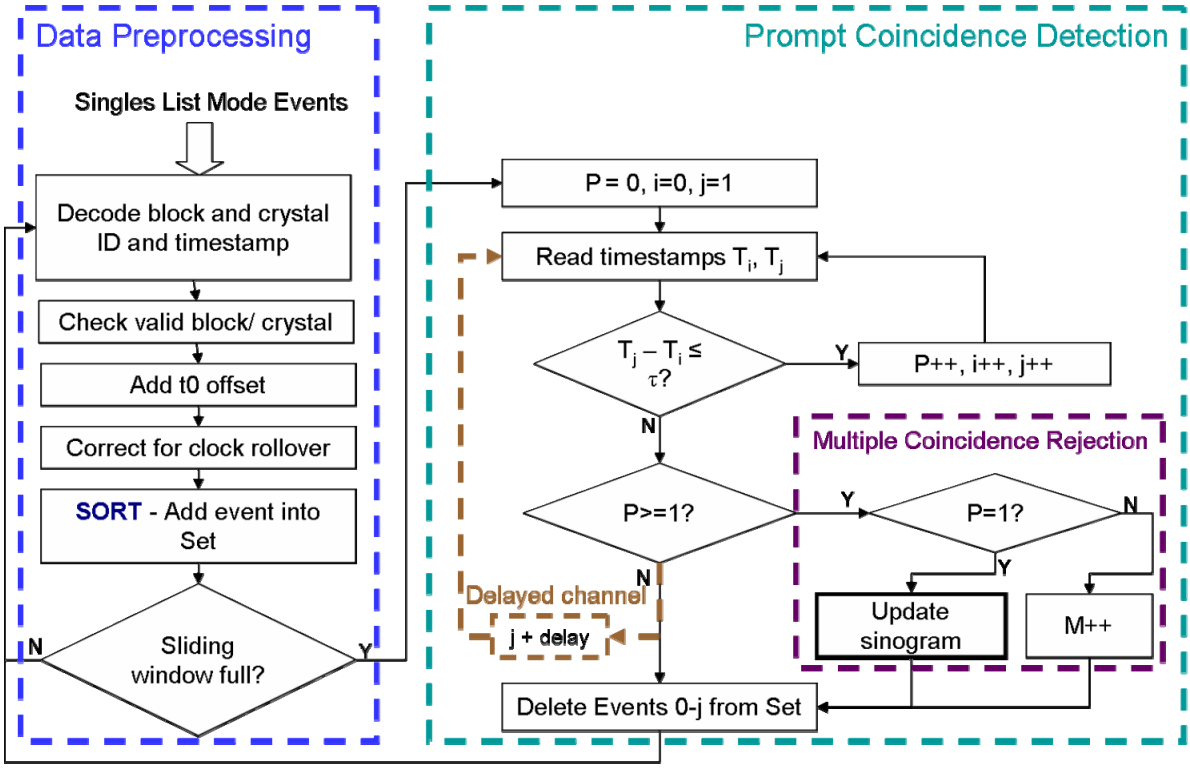

Figure 31 RatCAP Coincidence Processor Flowchart

RatCAP sinograms

Sinograms are uncompressed and fully 3D with 47 radial bins and 24 angular bins, since each ring of detectors is made up of 48 elements. A span of 1 gives 8 segments and a total of 64 axial planes, for 72192 total sinogram bins. These are stored as 4-byte integers resulting in sinograms of size of 282KB * f, where f is the number of dynamic time frames binned.

Section Conclusion

Performing the calibration scans detailed in these sections regularly to determine the optimal data acquisition protocols and coincidence processing parameters will go a long way towards ensuring consistently reliable imaging results with the RatCAP.

3.3 Image Reconstruction

3.3.1 Filtered Back Projection

Although it was decided at the outset that iterative reconstruction methods would be used to achieve improved resolution and noise performance for the RatCAP, 2D-FBP was also implemented for comparison of resolution performance across scanners. MATLAB provides functions to invert the Radon transform (sinogram) using FBP, but the unique geometry of the RatCAP calls for a few correction steps prior to reconstruction. Our approach takes advantage of the Monte Carlo model discussed earlier to come up with weighting factors for the sinograms to account for deviations from the ideal system response for FBP.

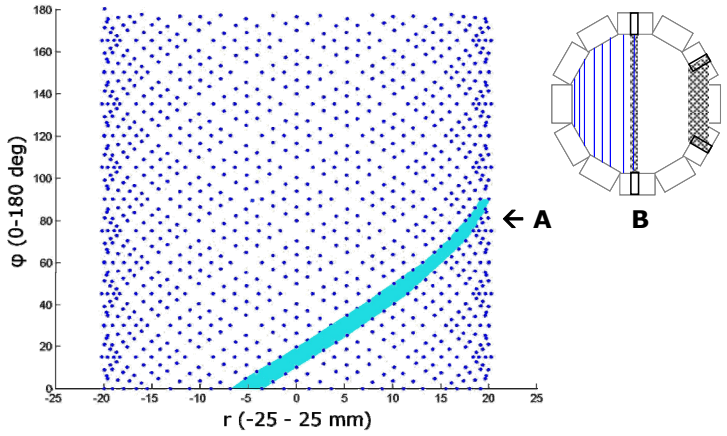

Figure 32 RatCAP sampling issues.
(left) non-uniform LOR sampling due to block detector geometry and circular FOV and (right) LORs are more closely spaced towards the edges of the FOV, but are broader.

Procedure

Assuming the centers of two detectors in coincidence are at (x1,y1) and (x2,y2) on the 2D Cartesian grid, the distance between them (or the length of the LOR connecting them) is $l = \sqrt{(y2-y1)^2 + (x2-x1)^2}$, the radial distance r of this LOR from the origin at (0,0) (or the cFOV) can be calculated by the shortest distance of a point from a line, given by $\frac{x1y2 - x2y1}{l}$, and the projection angle ϕ is $\varphi = \text{atan2}(\frac{y2-y1}{x2-x1})$.

Plotting r vs. ϕ for all combinations of detector pairs allows the visualization of our interleaved sampling grid as shown in Figure 32. Based on the figure, a summary of resolution degrading factors for the RatCAP geometry is given below. Most of these issues

are more pronounced in RatCAP sinograms since the imaging FOV occupies the entire detector aperture.

1. Gaps between detectors → the gaps between block detectors (for e.g.; blue band in the sampling grid) are fairly large compared to the size of the FOV and lead to missing projections, which violate the assumptions of standard FBP.
2. Non-uniform sampling → Due to the ring geometry of the tomograph, LORs are more closely spaced towards the edges compared to the center. The interleaved sinogram has a separation of 1.3 mm at r=0, which reduces to 0.62 mm at the $r=R_{max}$. FBP would require these LORs to be resampled into a uniform grid.
3. Crystal penetration → Oblique crystals near the edges of the FOV lead to an uncertainty in the exact location of the interaction along the depth of the crystal. This broadens the LORs, resulting in poorer resolution recovery in those regions.
4. Attenuation and scatter; variations in detector efficiencies → If uncorrected cause distortions.

The steps involved in the RatCAP's FBP algorithm are outlined in the flowchart in Figure 33 and elaborated below.

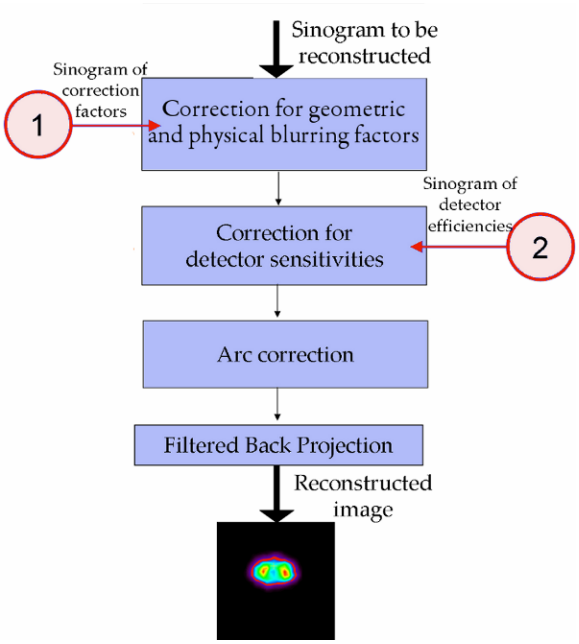

Figure 33 RatCAP Filtered Back Projection algorithm flowchart

Step 1: Sinogram pre-correction

Random coincidences were subtracted from the prompts sinogram prior to reconstruction.

Step 2: Correction for geometric and physical blurring factors (solid angle, crystal penetration, scatter and attenuation)

The Monte Carlo system model described earlier was used to generate weighting factors for each LOR. Ideally, this would be achieved by simulating a separate datasets of a long rod source perpendicular to each projection. Since the response of a rod source in a perfect system

is flat, the response in this case will contain the weighting factors for each projection, and could be used to correct for the combined effects of the non-uniformities. Since this was slightly complicated to implement, the rotation of the tomograph was approximated instead by rotating the phi bin for each detected event by the required angle of rotation. The 4 cm long rod source was simulated in water to include attenuation effects and, to some degree, scatter. Only 1/6th of the angular projections were simulated, assuming 6-fold scanner symmetry in ϕ. For statistical accuracy, >20 million coincidences were simulated in each voxel of the source.

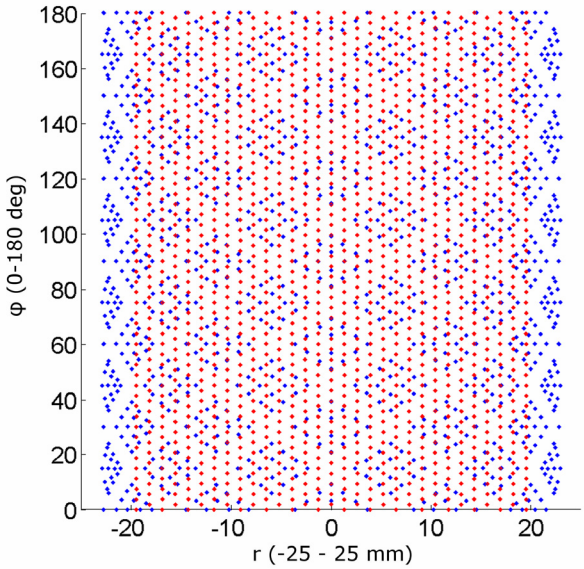

Figure 34 Uniform sampling grid (red) overlaid on original grid (blue)

Step 3: Correction for detector efficiencies.

A sinogram of LOR efficiencies was used to factor out non-uniformities due to variations in the efficiencies of the detectors. Since the same sinogram was used in the iterative reconstruction approaches, it will be discussed in more detail in a subsequent section.

Step 4: Arc correction.

This step is a correction for the non-uniform sampling, and can be considered as a correction for the positions of the LORs relative to the front face of the detectors. It was achieved by resampling the RatCAP sinogram into the uniform sampling grid shown in red, superimposed on the original RatCAP sampling grid in Figure 34. Interpolation was carried out using Delaunay triangulation of the data. Only sinogram pixels with non-zero values were used for resampling. The phi bins were shifted by half bin to align the phi bins at r=0 (since we do not have actual samples at r=0 and phi=0). This would cause a slight (<4° ~ < 1 image pixel) rotation in the output image, but would be more appropriate sampling. Figure 35 shows the effectiveness of the arc correction for point sources stepped through many radial positions in the FOV.

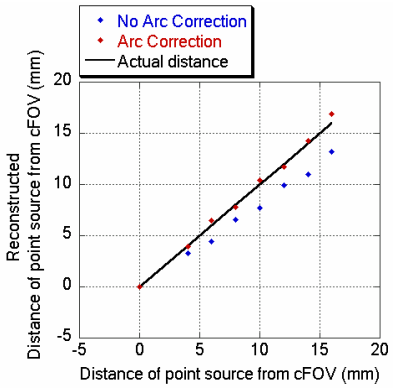

Figure 35 Validation of arc correction for point sources stepped through the FOV

Step 5: Filtered back projection.

The inverse Radon transform was performed on the corrected sinograms using the in built function in MATLAB. The function allows a selection of filters to be applied, interpolation methods and cutoff frequencies. The projections are zero-padded to a power of 2 before filtering to prevent spatial domain aliasing and to speed up the FFT. The images shown below were reconstructed with a ramp filter at Nyquist frequency.

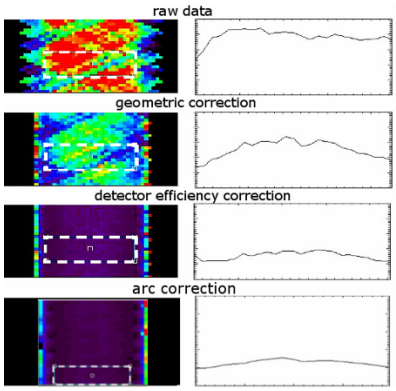

Figure 36 Steps 1 through 4 in sinogram space for a uniform cylindrical phantom

Validation

A separate scan of the uniform cylindrical phantom was used to validate the approach. Profiles on the sinograms (Figure 36) as well as the images (Figure 37) we used to compare the improvement at each step. The sinogram looks similar to that of an ideal cylinder after step 2, and is less noisy after step 3. In image space, the success of this approach is more evident. Reconstructing the image without any corrections shows a hole at the center, due to a combination of attenuation and geometric effects. The geometric and blurring corrections make the image profiles more uniform, but an undershoot artifact appears. The final image after resampling and zero padding shows no artifacts and an accurate redistribution of the counts such that there is no background activity. The algorithm will be used to evaluate the spatial resolution of the tomograph and compare it to other systems in 4.1.3.

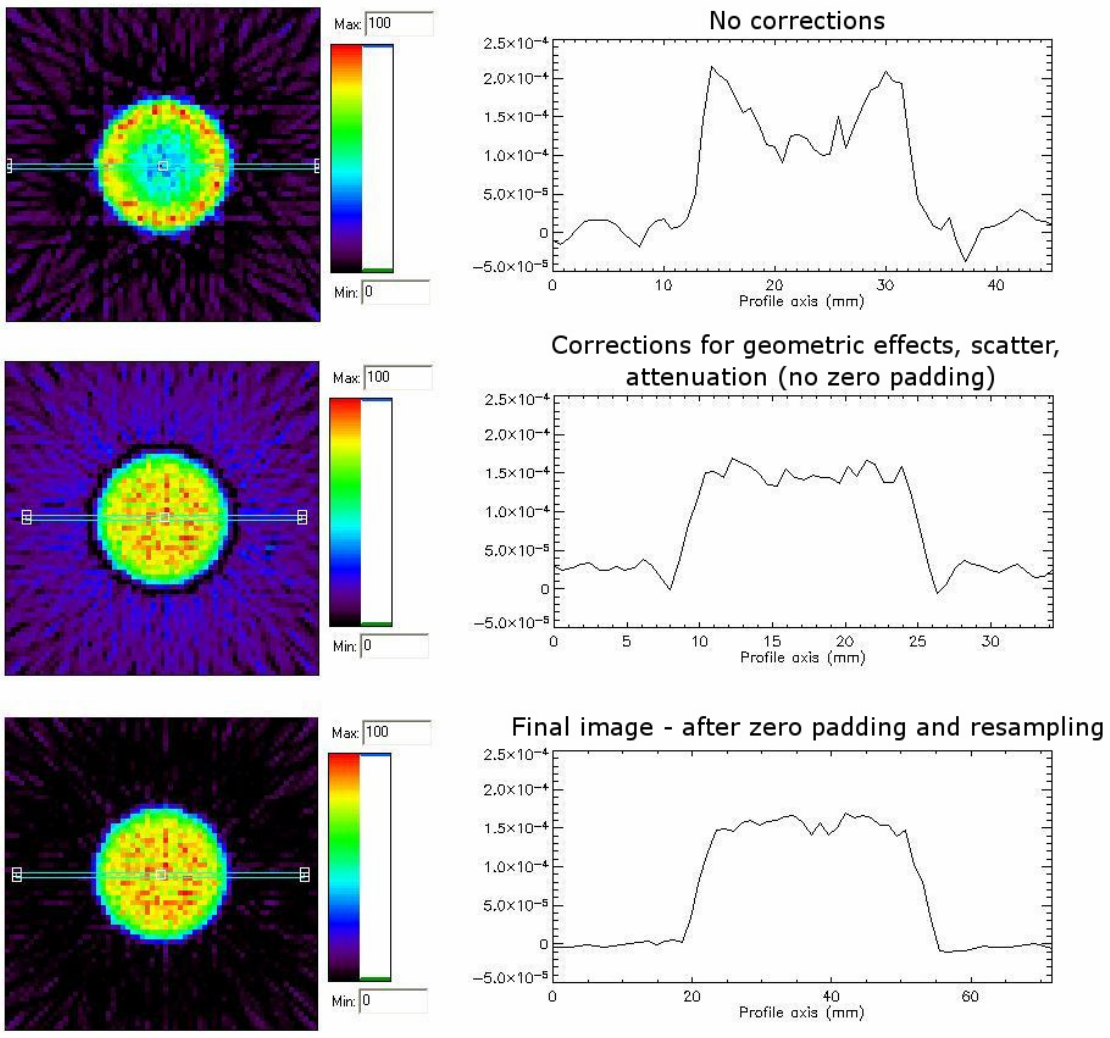

Figure 37 RatCAP FBP - results

3.3.2 Maximum Likelihood Expectation Maximization

The implementation of MLEM for the RatCAP system (RC-MLEM) contains additional explicit corrections to Equation **(16)** for random coincidences (r; additive contamination) and detector efficiencies (ε; multiplicative) as shown in Equation (***18***).

$$x_i^{n+1} = \frac{x_i^n}{\sum_j^{NLOR} A_{ji}\varepsilon_j} \sum_j^{NLOR} A_{ji}\varepsilon_j \frac{y_j}{(\sum_k^{NVOX} A_{jk}\varepsilon_j x_k^n) + r_j} \qquad (18)$$

A unique feature of our approach, and definitely the crux of RC-MLEM, is the Monte Carlo-estimated probability matrix, of which this section aims to be a thorough review. The other components of the algorithm i.e. the basis function, objective function and the optimization algorithm are standard. A quick justification for their selection follows:

- The cubic voxel basis was selected as being the most straightforward to implement and it is assumed that noise control will be handled sufficiently post-reconstruction.
- The use of ML-EM to maximize the Poisson likelihood is valid since no pre-correction factors are applied to the sinograms to destroy their Poissonian nature. Randoms are obtained as a separate estimate and accounted for correctly in the forward projection.
- While groups with larger systems struggle to store the pre-computed matrix and run the algorithm to convergence, the problem is tractable due to the small size of the RatCAP. Only the non-zero values and associated voxel look-up table are stored (~500MB) and the time taken per iteration is 3 seconds.

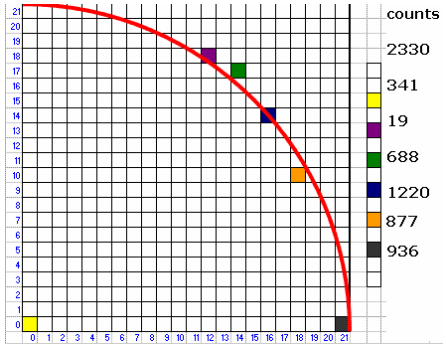

Figure 38 Treatment of edge voxels in SimSET

A. Probability matrix generation and storage

Source placement and simulation area:

Voxelized "point" sources are defined at the centers of each of the ~26K voxels within the cylindrical FOV using the comprehensive Monte Carlo system model described in

Section 3.1.2 and a separate simulation is run for each voxel. To make sure that voxels that are partially within the FOV at the circumference are modeled accurately, the acceptance radius for the center of a voxel is increased to (inner_diameter/2) + (voxel_diagonal/2). SimSET weights the counts based on the fraction of the voxel inside the circular FOV as shown in Figure 38, hence activity was simulated within the exact tomograph radius.

Attenuating and scattering object:

Sources are defined within a cylindrical phantom filled with water, the measurements of which match a phantom that is used for RatCAP calibration studies. This allows the calculation of normalization factors by taking a ratio of the simulated data to the measured data of the same phantom. The simulation tracks the photons in the water to account for an approximation of scatter and attenuation in tissue.

Storage:

Owing to the small size of the RatCAP's FOV, and the relatively few detectors and possible LOR combinations, the computation and storage of the matrix is within our capabilities. The number of elements in the complete probability matrix is 72192 (LORs) * 26011 (voxels) = ~1.9 billion. Instead of the actual probability values, which would require floating point integers and increase the storage size, the number of detected counts is stored as 2-byte integers, and the total simulated counts are factored out at the end of the reconstruction. This results in a full system matrix size of ~ 3.5GB. The individual sinograms are concatenated and then zero-suppressed to yield a ~500MB matrix (see examples in Table IV). A separate system matrix is generated from the scatter-only sinograms to allow forward projection of the reconstructed image through the scatter matrix for an estimate of the scatter contribution to the data.

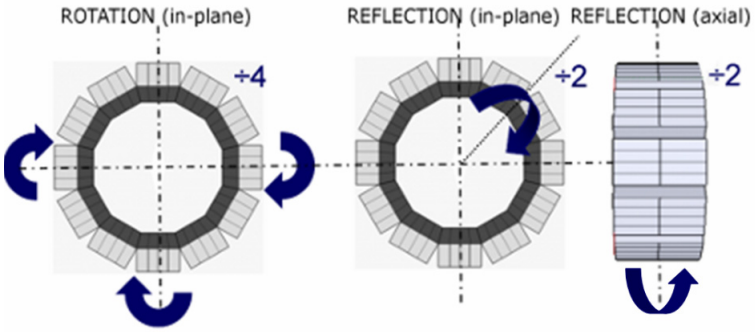

Figure 39 Symmetries in the RatCAP system

Computational cost and speed up factors

The simulation of the entire FOV takes approximately 10 days using eight cores of a standard CPU. A speed up of a factor of 16 was obtained by storing information regarding the inherent symmetries in the system in a look-up table. As suggested by Johnson et al [115]

and shown in Figure 39, the projections from one quadrant can be rotated in-plane by 90°, 180° and 270° to obtain projections for the other three quadrants. There is also 45° reflection symmetry within each quadrant. These factors combined result in a factor of 8 reduction in the matrix size and simulation time. Axial reflection symmetry provides another factor of 2. Breaking it down further in the transaxial plane is impossible due to the gaps between detectors. There is, however, the possibility of an additional factor of 2 due to parallel symmetry in the sinogram planes that has not been explored.

Current versions of the probability matrix do not make use of symmetries in order to allow the inclusion of asymmetric factors such as detailed object geometries, or the energy thresholds for individual detectors as mentioned in the next section.

The use of symmetries does not have any impact on the speed of reconstruction itself, but MLEM is highly parallelizable [213-215] and can be accelerated if required.

Probability matrix type	%Nonzero	Storage size (MB)	%detected counts
Comprehensive, Trues + Scatter	2.309	592	0.304
Comprehensive, Scatter alone	1.908	492	0.056
Geometric	1.096	281	0.360
Comprehensive, Trues alone	0.492	103	0.249

Table IV Table of system matrix sizes and sparseness

Comparison of probability matrix types

A number of probability matrix designs have been explored for multiple versions of the RatCAP with as well as without symmetries. For instance, for RatCAP v1, without programmable gains, the global energy threshold needed to be set at 150KeV for all channels to be detected. Since the actual threshold for each detector varied, a modification was made to the SimSET model for that system which read separate energy thresholds for each detector from a file to ensure a better match with the measured data. This was done away with for RatCAPv2. At the moment at least 2 matrix versions per scanner are in use, one is purely geometric and accounts for only solid angle and sampling effects whereas the other also includes positron range, photon noncolinearity and object scatter and attenuation (henceforth referred to as the comprehensive matrix). The sizes of these matrices are reported as the fraction of non-zero matrix elements in Table IV above.

It follows from the table that while photon scatter contributes a small fraction of the total counts (~18%); the inclusion of blurring factors (or more methodical modeling) reduces the sparseness of the probability matrix. The table also shows that higher statistics in the probability matrix increase the fraction of non-zeros. Since the comprehensive trues matrix has 30% fewer detected true coincidences than the geometric matrix (presumably due to attenuation), the higher statistics in the geometric matrix cause it to be less sparse. Clearly, there is a lot to be gained from maximizing the tradeoff between matrix accuracy and

simulation time/ storage size. Our studies to gain a better understanding of these issues are discussed in the following section.

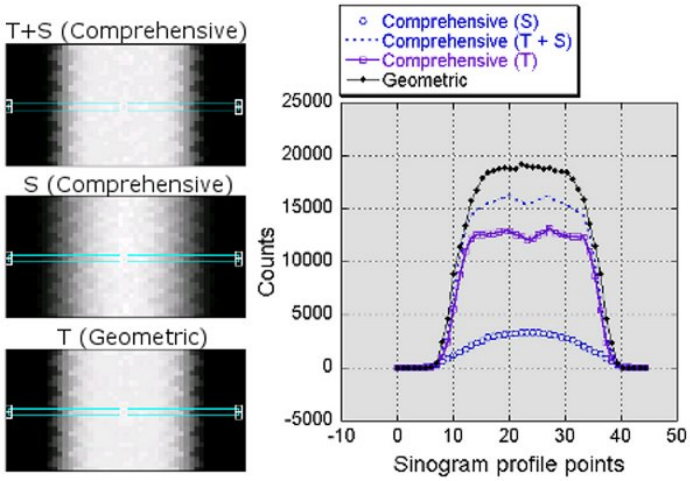

Figure 40 Comparison of sinogram profiles for geometric and comprehensive matrices
The separate scatter profile generated from scatter-only sinograms is also shown.

Probability matrix accuracy

Statistical accuracy in A is vital to avoid propagation of errors into the reconstructed image. One might expect that if significantly more events are simulated per voxel in A than can ever be expected to be seen in the data, the reconstructed image should not be affected by the noise in the matrix. While it is obvious that arbitrarily increasing the number of simulated decays will improve accuracy, it would be advantageous to find a point at which further simulations do not cause a significant incremental improvement in the image. A number of factors need to be considered when deciding on how many simulated decays will suffice, including errors in the data, the object being imaged and the reconstruction algorithm itself. A simulation study was performed and summarized here to find the optimal trade-off between matrix simulation time and reconstructed image accuracy, for typical objects that are imaged with the RatCAP. The steps are outlined in Figure 41 and elaborated upon below:

Simulated decays per image voxel (DPV)	%Nonzero	%Error in 'n' realizations
1 million (1M)	1.3	0.04
10 million (10M)	4.97	0.008
50 million (50M)	15.34	0.003

Table V Table of probability matrix characteristics for matrix accuracy study

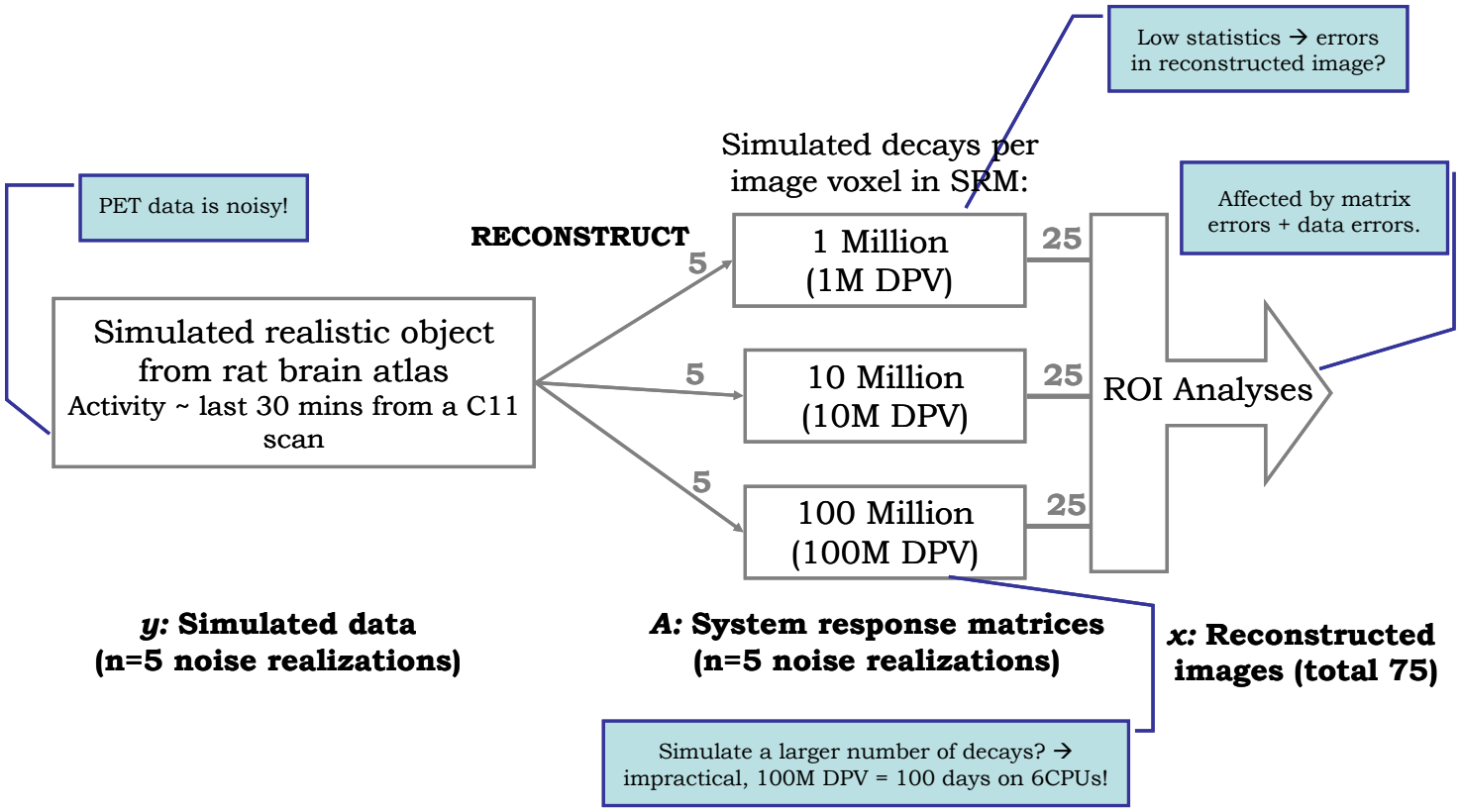

Figure 41 Illustration of simulated study design to evaluate system matrix accuracy

A single realistic dataset with 10,000 simulated decays per image voxel (DPV) was reconstructed using system matrices with varying accuracy (1M, 10M and 100M DPV). Five noise realizations of the data were reconstructed using each of five noise realizations of all the system matrices, resulting in 75 total reconstructed images for analysis. In a subsequent study, the statistics in the data to be reconstructed was also varied.

Probability matrices:

Comprehensive probability matrices were generated at 3 count levels; with 1 million (1M), 10 million (10M) and 50 million (50M) simulated decays per voxel (DPV). For each case, n=5 noise realizations were simulated to estimate the variability in the matrix. A very small FOV (1.75mm dia, 1mm length) was simulated. A comparison of the properties of the matrices is in Table V.

Data to be reconstructed:

To simplify the analysis and eliminate any misinterpretation that could arise due to differences between the model and detector, data was simulated using the same model that was used to generate the matrices. A rat brain atlas [216] was used to simulate three separate compartments (or regions) namely the left and right striata, frontal cortex and other brain tissues surrounding them. m=5 realizations were reconstructed using all n realizations of the 3 probability matrices, resulting in 3 x n x m total images to be reconstructed. In cases where the statistics of the data was evaluated, data was simulated at three count levels: 10K, 100K and 1M DPV, adding another factor of 3 to the number of images reconstructed.

Reconstruction:

Convergence of the high as well as low frequency components of the image was tested by reconstructing a single image for 10,000 iterations. Since the change in ROI values between 1,000 iterations and 10,000 iterations was <0.01%, subsequent images were reconstructed for 1,000 iterations and post smoothed with 1.8 mm 3D-Gaussian filter. 1.8 mm was selected since this was the resolution measured at cFOV using FBP.

Data Analysis:

ROIs were analyzed for the striata (typical uptake region), or for 'striatum/non-specific binding region' values. Different sizes of ROIs were used assess the combined effects of noise and ROI size. The "large" ROI included all the voxels in the striata and the "small" ROI included only 6 voxels in its central region. The %variability of the noise realizations was calculated as the ratio of the standard deviation to the mean expressed as a percentage. %Bias was calculated as the difference of the means from the true (simulated) values.

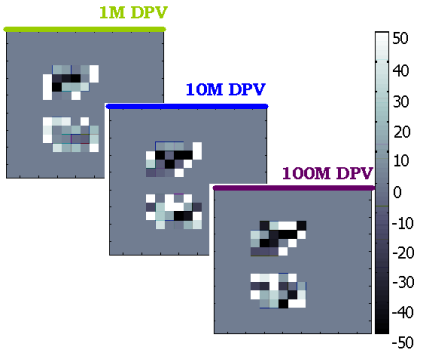

Figure 42 %Bias (%difference from simulated activity map of rat brain striata) images showing high frequency errors with varying count levels.

Goal I: Determination of extent of problem

It was established from initial studies that ROIs drawn the striata converged to a biased value. One dataset was simulated with 100K total DPV and reconstructed without any background activity with all 3 x n matrices. The %bias parametric images in Figure 42 show that the error occurs at the high frequency edges, and is likely due to partial volume effects, expected due to smoothing.

Goal II: Evaluation of noise and bias with varying matrix statistics

For each of the 3 count levels in the matrix, 75 total images were reconstructed (3 datasets * m noise realizations of each * n probability matrices). Noise-bias curves were plotted in Figure 43. The %variability does not change drastically with higher statistics in the matrix, and seems dependent only on the data. As long as the DPV simulated in the matrix are not less than the expected DPV of the data, the noise in the reconstructed image will depend mainly on the noise in the data. Oddly, there seems to be a dependence of the bias on the statistics of the matrix as well as the data.

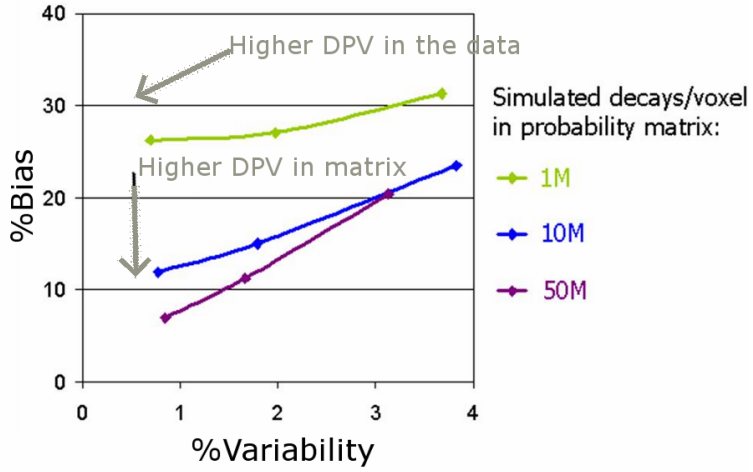

Figure 43 Effect of matrix accuracy and data accuracy on ROI bias and noise.
1K, 10K and 1M decays were simulated per image voxel (DPV) in the sinograms to be reconstructed. Probability matrices with 1M, 10M and 50M DPV were used for reconstruction. Five noise realizations of each of the datasets were reconstructed using each of five noise realizations of all the system matrices, resulting in 225 total reconstructed images for analysis. %Bias represents the difference in the mean of the noise realizations from the simulated input. %Variability represents the %std/mean among the noise realizations. It must be noted that in this plot, %Variability represents variability due to noise in the data as well as the matrix. Improved statistics in both (data and matrix) improves the bias but does not have a significant impact on the variability.

Goal IIIa: Evaluation of effect of ROI size in the presence of background activity AND
Goal IIIb: Separate evaluation of effect of matrix statistics and data statistics

Since the ratio of radiotracer concentration in specific to non-specific binding regions is pertinent to PET kinetic analyses, activity was simulated in the compartments in the ratio

6.5:1.5:1. (This number was obtained from autoradiography studies by [217]. This is a challenging test for the reconstruction and the results of Figure 44 are not easily interpreted. The %variability was assessed separately for the matrix and the data in this case. Also, due to the results of Goal I, ROIs of different sizes were evaluated. Again, the noise seemed dependent mainly on the noise in the data (and was highest for the smallest ROI). The bias was small for the small ROI, as expected with partial volume errors. This bias seemed to improve with increasing statistics in the data and the matrix. There was no clear-cut explanation for this phenomenon, but some of our conjectures are presented.

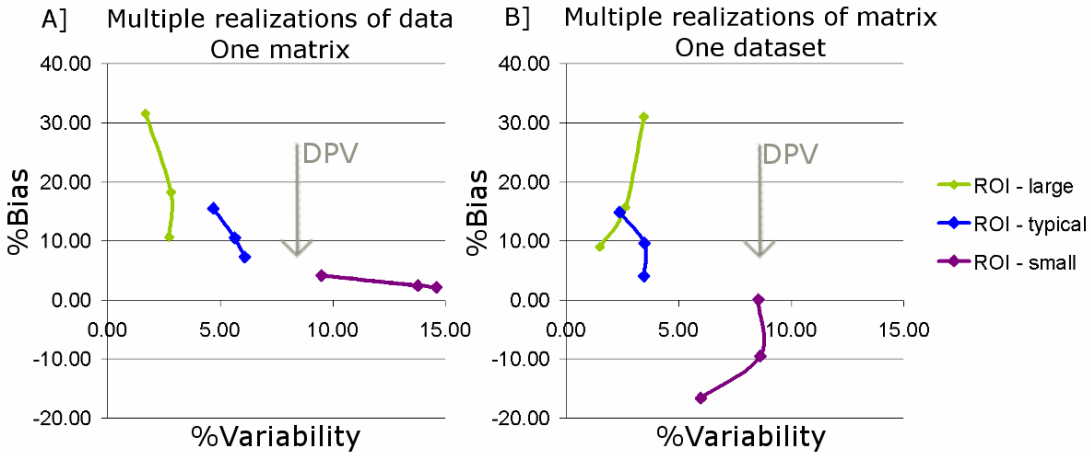

Figure 44 Effects matrix accuracy, data accuracy and ROI size

Here, the %Variability in the data is plotted independently (left) of the %Variability in the matrix (right). Hence, for each point on the curve, %Variability is calculated from 5 total images (as opposed to 25 in the previous plot). Clearly, this parameter does not change significantly with improved statistics in the matrix. The parameter affected by the statistics in the matrix is the bias. Hence, ROI sizes were varied between small, noisy regions with values that should be accurate and larger regions with high expected bias.

Summary of observations:

- The true system response was never predicted, and the algorithm converged to a biased value that was dependent on the variability of the data as well as the variability of the probability matrix.
- This bias in the reconstructed image appeared as an underestimation of voxel values at the high frequency components of the image and was observed to be less pronounced as the accuracy of the matrix improved.
- At the count levels expected from a typical scan in the RatCAP, the bias for a typical ROI improved by 2% with 50M DPVs in the matrix compared to 10M. This is a relatively small gain compared to the 5x increase in simulation time. It can be concluded that a typical ROI can be reconstructed with acceptable accuracy using 10M DPV in the matrix.

- Having said that, higher statistics in the matrix improve the accuracy of large ROI values, which might be useful for noisy datasets.

Possible explanations:

One possible explanation for the dependence of bias on the statistics in the matrix is that the matrix itself does not have uniform statistics. Less likely LORs are more accurate with the high statistics in the matrix. A related study was performed for the OPET [218], where the number of simulated decays was varied based on the axial position of the voxel to account for differences in axial sensitivity. In a preliminary simulation study, they showed a slight improvement in the resolution and contrast recovery, but a significant improvement in image noise. The goal of our approach, however, was not to have uniform statistics in the matrix but to have an accurate representation of the data. The generation of probability matrices with uniform statistics has not been explored.

B. MLEM convergence and noise control

The convergence of our implementation of MLEM for a specific ROI (striatum in a ^{11}C-Raclopride study) was studied using one of the 10K datasets (m=5) from the study above, reconstructed with the 1M and 10M probability matrices. The convergence plot in Figure 45 shows that the region has not quite converged till ~1000 iterations. Error bars were plotted from the standard deviation within a small, noisy ROI selected as a demanding test for the technique. At 1000 iterations, post-smoothing brought about a 20% improvement in standard deviation in the ROI selected, and looks qualitatively similar to the image after 10 iterations but is more accurate.

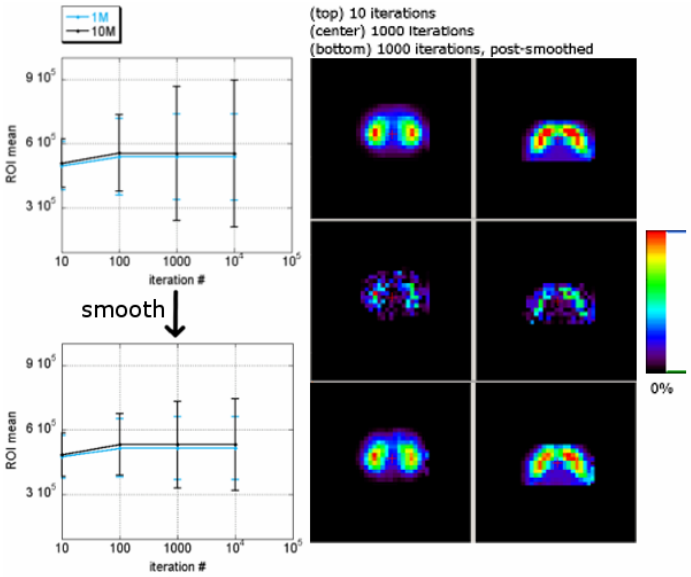

Figure 45 Noise and convergence properties with a post-reconstruction smoothing filter. Error bars are obtained from the standard deviation within the ROI.

Object dependent convergence

The object dependence of convergence was investigated by comparing the reconstructions of:

- a measured sinogram of point source placed in cylindrical phantom filled with water
- above sinogram + measured sinogram of the phantom filled homogeneously with ^{18}F solution.

Since a low rate point source was used, the randoms contribution of the point source data was assumed to be negligible, hence the addition of counts was considered to be realistic. For the dataset with the warm background, noise in a background ROI is also reported as a function of iteration. Figure 46 shows the results. The point source in the warm background converges at a completely different rate, and also converges (at ~1000 iterations) to a different value (the mean value of the background was subtracted) as discovered by other researchers [219]. All images were post-smoothed with a 1.8 mm 3D-Gaussian filter.

Observations

It can be concluded from the above that for ROI analyses on small distinct objects in the presence of background activity, images must be reconstructed for at least 1000 iterations and post-smoothed to control noise. The selection of the post-smoothing filter will be discussed in the next section. ROIs must exclude the edges of the objects to avoid partial volume effects and high frequency artifacts. Obviously, this may not be the most favorable approach for objects with a different source distribution.

All PET systems employing EM reconstruction schemes have to deal with issues such as the object and position dependence of the mean values and statistical noise, and no universally acceptable solution exists at the moment. As long as these problems are well understood for a particular system, protocols can be optimized for specific imaging tasks to ensure accuracy within a few percent.

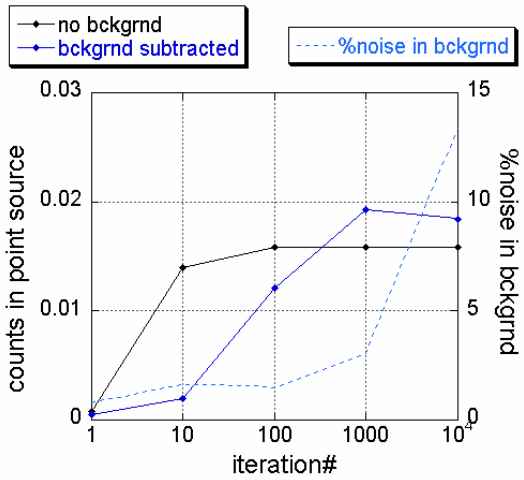

Figure 46 Object-dependent MLEM convergence for a point source with and without warm background

3.3.3 Noise vs. bias reconstruction analysis

A small investigation of the performance of our implementations of FBP and MLEM in terms of noise and resolution recovery is presented in this section. Further evaluation of contrast recovery, resolution throughout the FOV etc will be discussed in the section that covers phantom studies, since these are dependent on the efficacy of the correction methods discussed in the next section.

Overview of approach:

Data:

Sinogram of cFOV point source (10MB data) added to cylindrical phantom sinogram (500MB data) leading to a contrast of 3:1. 10 noise realizations were generated. The point source data had a total of ~65,000 true coincidences.

Reconstruction:

1) 2D-FBP
2) 3D-MLEM with the geometric probability matrix (3D-MLEM$_g$)
3) 3D-MLEM with the comprehensive probability matrix (3D-MLEM$_c$)

Analysis:

Resolution: FWHMs were calculated from a 3-pixel wide profile fit to a Gaussian with an offset.

Noise: The %std/mean was calculated for a 100-pixel background ROI on a different axial slice from the point source. For 2D FBP, a single slice was used. For MLEM, 3 slices were used.

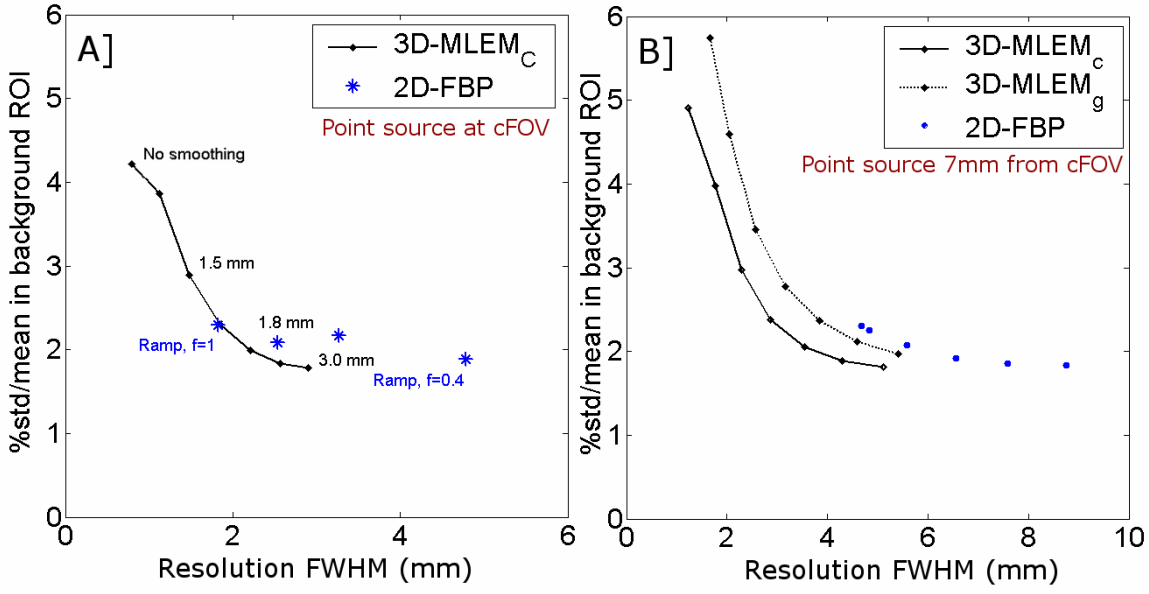

Figure 47 Comparison of FBP and MLEM for the RatCAP

Goal I: Determination of FBP cutoff filter

The cutoff frequency for the ramp filter was varied from f=1 to f=0.4 to find one with MLEM-equivalent noise levels. The MLEM images were post-smoothed using Gaussians with FWHM varied between 0 and 3 mm. Noise-bias curves for a point source at cFOV (Figure 47A) show that the filter at Nyquist frequency produces a sufficiently smooth image comparable to MLEM, and no further reduction in cutoff frequency needs to be applied for similar count levels.

Goal II: Comparison of algorithms for off-center ROI

The point source at cFOV is reconstructed satisfactorily using both reconstruction algorithms in Figure 47. However, the reconstruction for a point source placed off-center is slightly more challenging and was evaluated for the source placed 7 mm away in the radial direction. In this case, the resolution numbers reported are the tangential and radial resolutions added in quadrature. The performance of the geometric matrix was evaluated here as well.

Section Conclusion

For a point source placed in the center of the FOV, an ideal case for FBP, the resolution and noise properties are similar to that of MLEM. For sources placed away from the center, however, it is clear that MLEM achieves a better noise-bias curve, despite our corrections for FBP. It is also evident that the comprehensive system model outperforms the geometric model, though it relies heavily on the accuracy of the modeling. These results validate our premise that systematic modeling of the data and system response result in increased accuracy in the reconstruction throughout the FOV.

3.4 Quantitative Corrections and Calibration

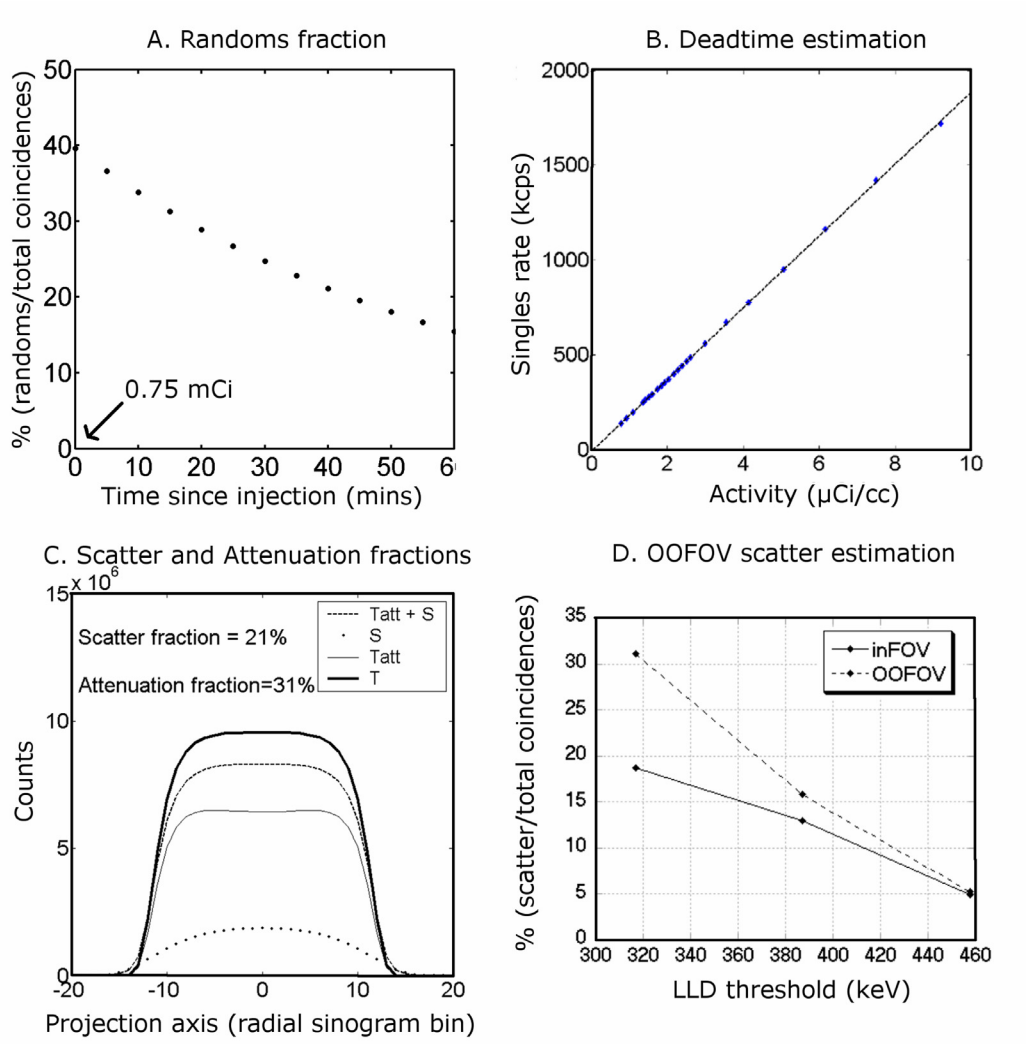

Figure 48 Count rate dependent errors in RatCAP studies

A. Randoms fraction for a typical animal study with a 0.75mCi injection: <=40%
B. Estimation of dead time from decaying source experiment: 0% up to 10µCi/cc
C. Scatter / attenuation fractions for a uniform cylindrical phantom: 21% / 31%
D. Scatter from outside the FOV (OOFOV): +7% at 350KeV

3.4.1 Magnitude of errors in RatCAP studies

Random coincidences

Since only the brain of the rat is within the FOV of the tomograph and restrictions on its weight prevent the use of side shields, the RatCAP is vulnerable to random coincidences from organs outside the FOV. Figure 48A shows the randoms fraction, calculated as the %(randoms/total coincidences) for a typical RatCAP study with a ~750 μCi injection of ^{11}C-Raclopride. At the time of injection, 40% of the detected coincidences were random. Towards the end of the scan, when the data rates were as low as 10 kcps, the randoms fraction reduced to ~15%. The estimate was obtained using the delayed channel method with a time window of ±9 ns. Random coincidences are the biggest concern in RatCAP studies, and the development of an accurate method for correction is crucial.

Multiple coincidences

The total coincidence rate quantifiable by a PET scanner is limited by the size of the time window due to multiple coincidences at very high rates. For example, for rates in the range of tens of millions of singles per second, the time difference between adjacent events could be, on an average, less than the size of typical nanosecond time windows. It is very likely that most of the coincidences detected are multiple. Unless advanced algorithms are used to separate the true coincidences, this would result in a loss in sensitivity. In case of the RatCAP, since multiples are rejected by our coincidence processing algorithm, this phenomenon results in a loss of >10% of the trues at singles rates >1Mcps using a time window 2τ of ±20ns. Data rates >1 Mcps are avoided for quantitative RatCAP studies.

Scatter and Attenuation Fraction

Using a threshold of 350KeV to filter out low energy photons, a simulated cylindrical phantom sized to fill the entire FOV of the RatCAP (3.6 cm diameter x 2.6 cm length) showed that the scattering of one or both photons one or more times in tissue results in an increase of a 21% in the total coincidences (T_{att}+S), as shown in Figure 48C. An additional contribution of 7% at 350KeV comes from the 6 cm diameter x 13 cm length cylindrical phantom simulated outside the FOV (OOFOV), with the OOFOV fraction increasing significantly with the size of the energy window as shown in Figure 48D. The fraction of attenuated photons %(T-T_{att})/T, calculated for the same phantom within a homogenously attenuating water medium is 31%. Even though the rat brain has a slightly more complex structure, this is a good approximation of the expected attenuation fraction in our studies.

Dead time

A decaying source experiment was carried out to estimate the amount of dead time in our system using a "head" phantom placed inside the FOV as well as an OOFOV "body"

phantom as shown in Figure 49, with sizes similar to the simulated phantoms described above. The singles rate was seen to be linearly related to the activity in the phantom with r=0.995 up to 10 μCi/cc or detected singles rates of 2.5Mcps. Since typical injected doses for RatCAP studies are expected to be 5-10μCi/cc, no correction for dead time is required within this range.

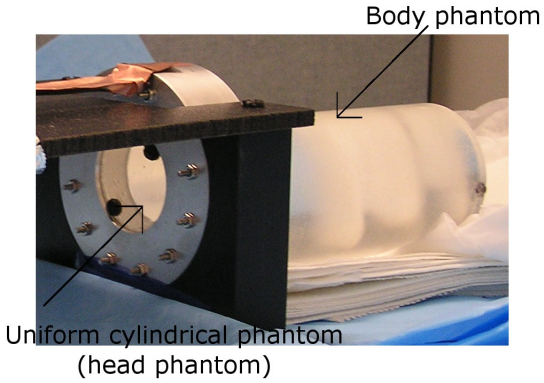

Figure 49 Phantom relative sizes and placement

Two cylindrical phantoms filled homogenously with activity and placed back to back such that their volumes correspond to the head and body of a rat

Detector efficiencies

Normalization for the RatCAP is essentially a correction for intrinsic detector efficiencies, since the geometric effects related to the block detector geometry and sampling are modeled into the probability matrix. Although the efforts described in 3.1 have minimized any variation between the detectors through careful selection of the detectors and alignment of their gains to ensure an electronic and mechanical match, some non-uniformity among them still remains, and can be factored out. The variation between LORs has been measured to be ~24% FWHM and is shown in Figure 50. Geometric effects have been factored out in the plot to isolate only the non-uniformity in the detectors, although it is possible that the plot also contains the error contribution due to possible mismatches between the simulation and the measured data.

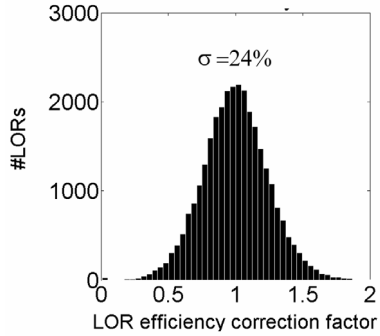

Figure 50 Histogram of LOR efficiencies for RatCAP v2.6

Note that these correction factors account for not just intrinsic detector efficiencies but also any mismatches between the simulation and measured data

3.4.2 Randoms correction

Since the object to be imaged fills the FOV of the RatCAP, it is not possible to use profile fitting methods to estimate randoms and scatter. Instead, the delayed coincidence channel and singles-based approaches to obtain randoms estimates have been compared and evaluated.

1. **Delayed coincidence channel approach**

This delayed coincidence channel idea has been adapted to fit the offline coincidence processing scheme for the RatCAP's singles list mode data. Since our coincidence processing is not done in real time, estimating the randoms in this manner does not add dead time to the system. An overview of the algorithm is provided here but is described in greater detail in [212]. The most straightforward implementation of the delayed channel on time-sorted data would involve delaying every single event to look for a random pair. This would result in a factor of 2 in the randoms estimate as shown in Figure 51 which can be factored out. However, a simple division by 2 would require the storage of floating point data. Reducing the size of the delayed window to τ (with the prompts window being 2τ) is not possible in discrete implementations since symmetric time windows need an odd number of bins to account for the zero time difference bin in the center. The chosen solution was to delay only one specific channel of each coincidence pair to mimic traditional electronic schemes and produce integer data with no scale factors.

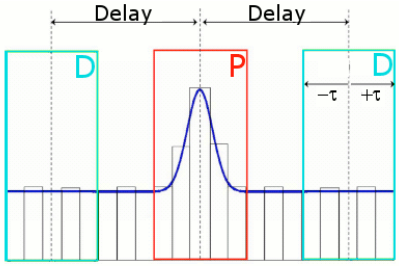

Figure 51 Estimating randoms using the delayed channel method.
Figure shows two delayed windows on either side of the prompts window

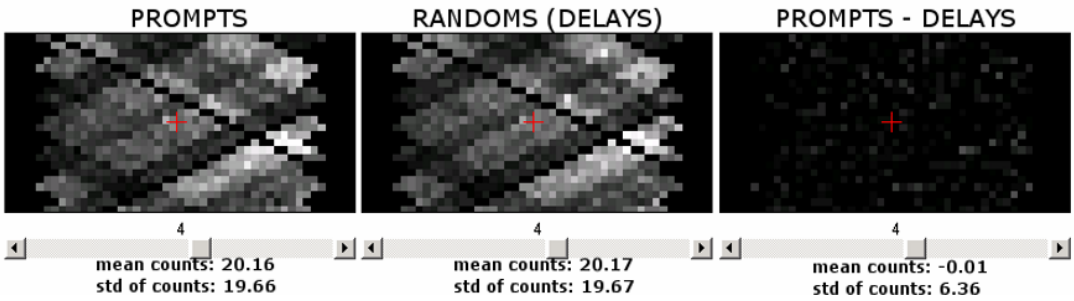

Figure 52 Evaluation of delayed channel estimate I: using a single photon source for which all detected coincidences should be random

To validate the delayed coincidence channel estimate D, a ~3 mCi ^{137}Cs source was placed inside the FOV and data was acquired with the LLD set at 500 mV to account for the

higher energy photopeak of ^{137}Cs. Any coincidences detected using a single photon source must be random, and the number of prompt coincidences, P must equal D. Figure 52 shows that the accuracy of the mean of D over the entire sinogram was >99%. This high level of accuracy was also true for multiple ROIs drawn throughout the FOV.

Next, a ~30 μCi ^{68}Ge point source was scanned in air in the center of the FOV with the ^{137}Cs source placed outside as a source of high randoms. The resulting sinograms had ~6 times more random coincidences than true coincidences. The LLD was set to 350 keV for this study, and high scatter in the background was expected due to the low threshold for ^{137}Cs photons. Figure 53 shows the sinograms and sinogram profiles before (left) and after (right) randoms subtraction. An approximate estimate of scatter, obtained as described in the next section, was also subtracted. The subtraction of scatter reduced only ~10% of the background counts whereas the remaining 490% reduction was due to randoms subtraction.

While Figure 52 and Figure 53 demonstrate the low bias of the delayed channel estimate, Figure 52 also underscores the noise in D, and a substantial increase in the noise on subtraction.

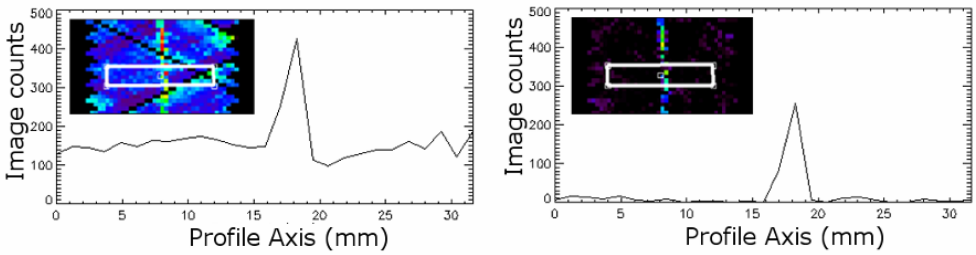

Figure 53 Evaluation of delayed channel estimate II: using a point source with high randoms background

2. Multiple averaged delayed channels

A simple variance reduction technique implemented for the RatCAP involves the use of an average of multiple, non-overlapping delayed channel estimates. The number of channels averaged is limited only by the rate of incoming data, and 10 windows were used in our case for a reduction in noise by a factor of √10. This technique has the same advantages as a single delayed window in terms of dead time and efficiencies, but could be a significant improvement for noisy data.

3. Singles-based estimation technique

The two techniques discussed so far were compared with the singles-based randoms estimation (SBR) technique, implemented as follows: Since the RatCAP singles list mode data file consists of events that have already passed through energy discrimination, Equation (3) in Section 2.1.1C is applied only to singles that can realistically contribute to a random coincidence. In order to ensure uniform statistical quality in the singles based estimate for a given dataset independent of the rate, the SBR estimate was updated frequently after a fixed

number of singles rather than after fixed time intervals. This minimized the error in the estimate even with rapidly decaying tracers. An idea of the level of noise reduction compared to D can be had from Figure 54, which compares the two estimates with the ^{137}Cs source placed slightly off-center.

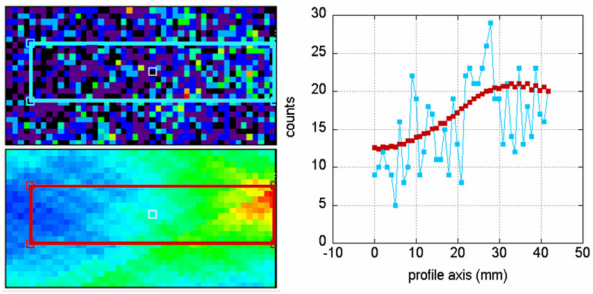

Figure 54 Pictorial comparison of randoms estimation methods with a focus on noise.
(left) Transverse sinogram planes of (top) delays and (bottom) singles-based estimate with source placed slightly off-center
(right) profiles along marked boxes showing matched means and improved noise with the singles based estimate

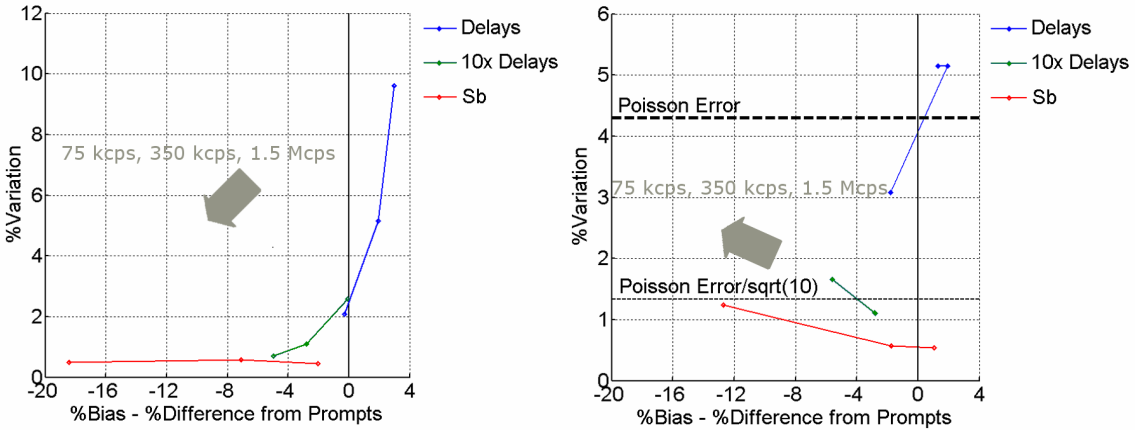

Figure 55 Noise vs. Bias comparison of 3 methods to estimate random coincidences/
(left) fixed number of singles processed for each point on the curve (Poisson noise varies for the delayed channel estimate). (right) fixed number of randoms evaluated (Poisson noise should be constant).

Validation and comparison of methods

For a quantitative test of the performance of the three methods at varying singles rates, the ^{137}Cs source was moved in steps away from the tomograph to vary the rate of incoming data from 1.5Mcps to 75kcps. Each dataset was acquired at 500 keV and split into 25 statistically independent subsets with the same number of singles (50,000) in each. The means and standard deviations (stdev) for each dataset were calculated from the total counts in the 25 subsets. Bias was calculated as the %difference of the mean from the mean prompts,

since all coincidences should have been random. Noise (%Variation) was expressed in terms of %stdev/mean. The results are plotted in Figure 55 (left)
Since D reduces with count rates, the evaluation of both delayed channel estimates using a fixed number of singles at different count rates is not appropriate. A new analysis was performed, but this time with a varying number of singles processed at each data rate in such a way as to obtain an equal number of random coincidences within a margin of error of 1%. Each sinogram had ~500 ± 5 counts, and the Poisson noise in both delayed estimates was uniform at all data rates, as shown Figure 55 (right).

Interpretation of results

The figures above clearly demonstrate the superior statistical quality of the singles-based estimate due to the Poisson errors in the delays, as well as 1/√10th of the Poisson error in the estimate using an average of multiple channels. Although multiple delayed channels are straightforward to implement, using a large number is time consuming, and an accurate implementation of the SBR method might be more practical. In the RatCAP implementation, a significant bias was observed in the SBR estimate at high rates. This could partly be due to an underestimation of the prompts at high rates because of multiple coincidence rejection as discussed earlier. The windows for D and P will have the same treatment for multiples, and since P was used as the true value, this shows up as a relative bias in the SBR estimate. For the data set at 1.5Mcps singles rate, over 3% of the coincidences were rejected, reducing the apparent "bias" in the SBR to 4%. A small rate-dependent bias still remains, and even though we do not expect a large fraction of dead time at operating rates, it could explain the bias with the 1.5Mcps estimate.

Since randoms are fairly uniform over the FOV, the distribution of errors in the sinogram was not considered. Sinograms with very low counts/LOR similar to realistic data were used, so as to focus the study on noise.

3.4.3 Attenuation and scatter correction

A first order correction for attenuation and scatter was achieved by simulating the sources for the reconstruction probability matrix A within a homogenous cylinder filled with water. Since the interactions of photons in the attenuating medium would then be built into the probability matrix, the reconstructed images would be corrected for attenuation as well as scatter. To take this premise a step further, an attenuation map of the rat head was obtained using anatomical images from the SkyScan-1076 in vivo microCT scanner. Our approach to develop and validate a CT image-based attenuation correction method is discussed below.

Set up and generation of probability matrix

For all RatCAP studies, an aluminum positioning sleeve is stereo tactically aligned and surgically mounted on to the head of the rat for constant and reproducible placement for

all subjects. Four Sprague Dawley rats were scanned in the CT scanner with the aforementioned sleeves attached, to aid co-registration of CT data to the RatCAP's FOV. A couple of transverse planes of the CT image are shown in Figure 56 along with a positioning scan with the aluminum sleeve. The CT images of the four subjects were downsampled for matched resolution with the PET images using filtering and nearest neighbor interpolation. Next, they were segmented into four regions: air, bone, tissue and aluminum using a basic thresholding algorithm. An example of a downsampled, segmented CT image is in Figure 56. Finally, the images were used as the attenuation input files to our SimSET model. One image (Rat0) was used to generate the probability matrix as described in Section 3.3.2, while the others were intended to simulate biological variability among rats.

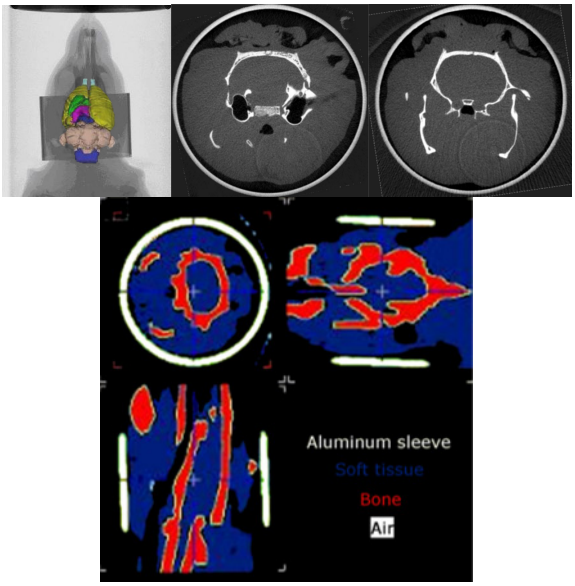

Figure 56 Generation of CT-based attenuation map
(top, left) Placement of Aluminum sleeve and pilot scan showing positioning of sleeve with brain regions overlaid (top, right) Two CT image slices (bottom) Segmented CT image

Comparison of geometric, homogenous and CT attenuation maps

A simulation study using the image from Rat1 as the input attenuation map is shown in Figure 57. The emission distribution for the simulation was obtained from a prior high statistics ^{18}F-FDG rat brain study in the RatCAP. A comparison of image profiles using the geometric (air), homogenous (water) and CT-based probability matrices for reconstruction of this simulated sinogram is in Figure 57, along with the %difference from the simulated value. The figure confirms that a global scale factor would not be sufficient to correct for attenuation, and modeling the attenuation map is necessary. The 20% improvement due to attenuation compensation compared to the geometric matrix (i.e. no correction for attenuation or scatter) is consistent with initial calculations of the attenuation fraction earlier in this section. An additional increase of ~5% in the striatal ROI was seen due to the CT matrix. Moreover, the

cold valley between the striata has been reproduced more accurately using the CT matrix due to improved scatter modeling. The images were reconstructed for 100 iterations, and iterating to convergence might have improved the match with the simulated input.

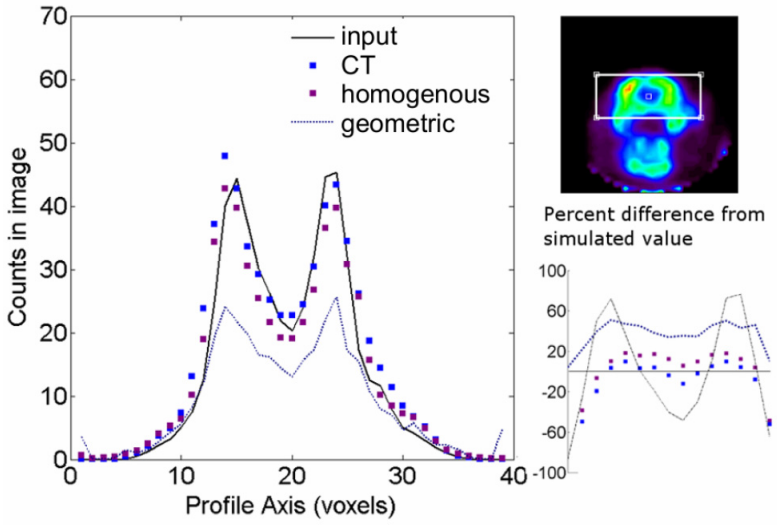

Figure 57 Comparison of 3 object models for attenuation correction.
(left) Transverse profile along (right, top) reconstructed image and
(right, bottom) %difference from simulated values. The input profile is included in this plot only for region identification

Multi-subject simulation study

A separate study was performed to evaluate the feasibility of using this CT-based attenuation matrix for subsequent studies in the RatCAP.

Hypothesis

A single system model which assumes fixed attenuating media will suffice to correct for scatter and attenuation in all rats of a given strain and weight.

Approach

Four separate simulations were generated, using Rat0-Rat3 as the attenuation maps. The same source distribution from the prior study was used as the emission map for all four simulations. Excluding Poisson noise, any variation in the reconstructed images should have been due to the differences in the attenuation map (or inter-subject anatomical variability). To separate the contribution of Poisson noise, 4 noise realizations were simulated for each case for a total of 4x4 simulated sinograms. The sixteen sinograms were reconstructed using the same probability matrix (generated using Rat0) to test the hypothesis. ROIs were drawn on the left and right striata and compared with the simulated value for an estimate of the bias, and the standard deviation among the noise realizations was used as a measure of the uncertainty (labeled accuracy in the plot).

Results

The results presented in Figure 58 also show the 20% and 25% increase in ROI values using the homogenous and CT attenuation maps compared to the no correction case. To test our

hypothesis that a single probability matrix using a representative rat brain image would suffice to correct for all rats of a given weight and strain, the variability among the 4 datasets was compared to the variability within multiple realizations of the same dataset (Rat0), reconstructed using a matched matrix. The former was observed to be larger for our region of interest, which went against our hypothesis, but the overall variability was low compared to the improvement in bias using the CT-based matrix.

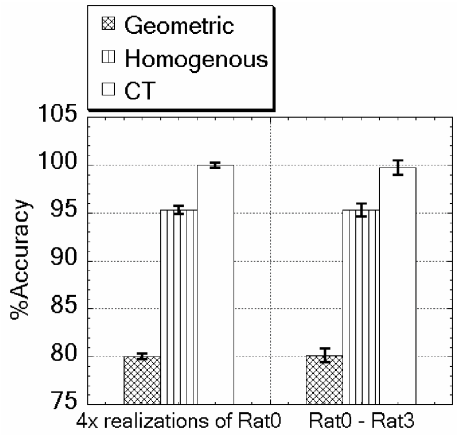

Figure 58 Comparison of within-rat (Poisson) variability to between-rat variability for 3 object models used for attenuation correction.

The hypothesis that a single attenuation map would suffice to reliably correct for attenuation in different rats was proved incorrect by the error bars due to variability between subjects.

Future directions

In the future, a CT map obtained from an average over multiple subjects might increase the reliability of the CT-based probability matrix. A smoothed version of this attenuation map might also be more accurate than a simple homogenous attenuation map. For now, the homogenous map was used for subsequent studies, since a 5% bias was more acceptable than an uncertain estimate. Only a portion of the FOV was simulated for the emission map in this study since realistic activity levels over the entire brain would require extremely long simulations. Hence, testing the impact of attenuation correction on other brain regions relevant to PET studies was not possible.

An independent validation of scatter correction

An estimate of scatter in our sinograms can be obtained by forward projecting reconstructed (converged), randoms corrected images through a probability matrix generated from scatter-only sinograms made available by SimSET. This scatter estimate was validated to verify the accuracy of the scatter modeling using a point source placed within a water-filled cylinder at the cFOV. Data was acquired at 350 keV to match the simulation of the probability matrix. The sinogram was reconstructed for 1000 iterations and forward projected to obtain the estimate shown in Figure 59. The point source shows a scatter fraction of 15%, which was consistent with the simulations discussed earlier.

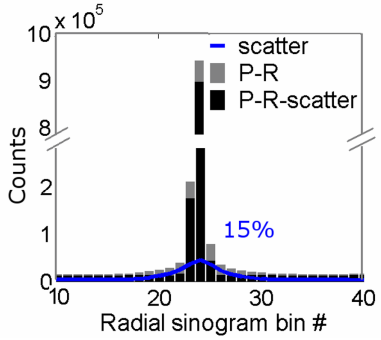

Figure 59 Validation of the scatter estimate for a cFOV point source

The scatter estimate (blue) was obtained by forward projecting the reconstructed image through a scatter-only probability matrix. The scatter and randoms (R) together accurately account for the tails in the point source profile.

Estimation of scatter from outside the FOV

The Monte Carlo-simulated scatter matrix enables a unique method to accurately account for scattered coincidences from outside the FOV (OOFOV). Figure 60 shows a reconstructed image of a simulated scatter-only sinogram using the scatter probability matrix. For the simulated point source placed at cFOV, the resolution of the scatter profile was 6.5mm FWHM. Thus, objects placed outside the FOV that contribute only scattered (and randoms, corrected independently) counts can be estimated by extending the probability matrix to include the OOFOV region. Figure 61 Scatter sinogram of two point sources placed 6 mm apart, reconstructed using the scatter probability matrix shows that since scatter has a slow-varying distribution, two point sources placed 6 mm apart could not be fully separated using the scatter-only matrix reconstruction and hence a high degree of voxelization outside the FOV might not be necessary.

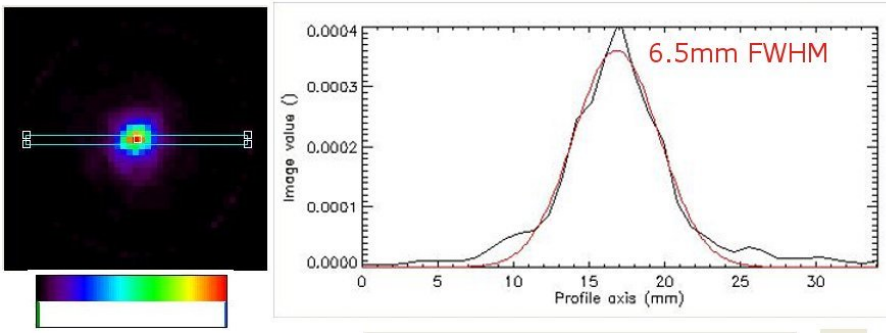

Figure 60 Simulated scatter-only sinogram reconstructed using the scatter probability matrix

A single large voxel has been simulated outside the FOV which corresponds to the volume of the entire rat body (minus the head). Counts scaled to the larger volume are simulated in this voxel during the generation of the probability matrix. Reconstruction using this matrix accurately estimates the OOFOV scattered counts from simulations. Additionally, when the "body" phantom was scanned in the RatCAP with no activity inside the FOV but just water to serve as a scattering medium, the total P-D counts were estimated by the outside voxel.
Since scatter from the body is a small fraction (7%) of the total coincidences at the operating energy window for the RatCAP, this straightforward correction approach should suffice to account for its effects. Future simulations could take into account the nose side of the detector as well, since the localization of activity in the harderian glands just outside the axial end plane of the RatCAP could pose problems.

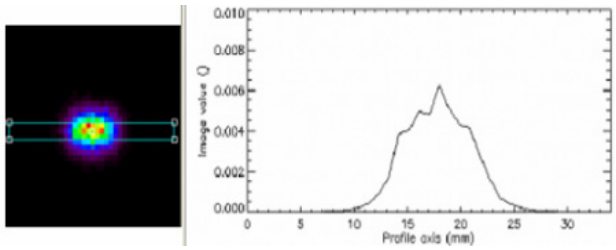

Figure 61 Scatter sinogram of two point sources placed 6 mm apart, reconstructed using the scatter probability matrix

3.4.4 Normalization

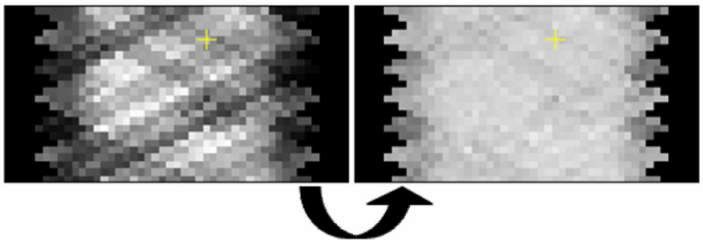
Figure 62 Sinogram of uniform cylinder scanned in RatCAPv1 before and after efficiencies correction

Normalization coefficients for each line of response of the RatCAP are obtained using a high statistics scan of the cylindrical phantom that fills the FOV. The ratio of this sinogram to a simulated sinogram of the same phantom gives a sinogram of intrinsic detector efficiencies. This sinogram is sufficient for normalization since all geometric effects have been modeled in the simulated probability matrix. A correction sinogram obtained in this manner simultaneously corrects for any errors in geometric modeling as well as systemic variations in the detectors. However, the approach is similar to direct normalization and is susceptible to the same issues with Poisson noise. Since the number of LORs in case of the RatCAP is not large, a high statistics measurement is possible, and the influence of the statistics of the normalization data on the reconstructed image will be discussed next.

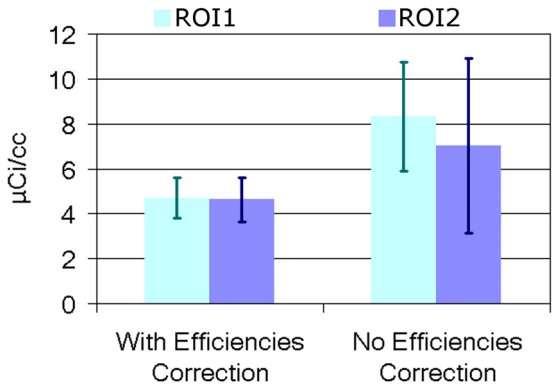

Figure 63 Validation of efficiencies correction for two ROIs drawn on the reconstructed image of a homogenously filled cylindrical phantom scanned in the RatCAP. Error bars represent variation among pixels in an ROI

To begin with, however, the improvement in the sinogram of a homogenously filled cylindrical phantom before and after correction with the efficiencies sinogram is shown in Figure 62. ROIs drawn on different locations on the reconstructed image of the above phantom were compared. It can be observed in Figure 63 that ROI values are more uniform throughout the FOV after efficiencies correction, with an added improvement in the standard deviation within an ROI.

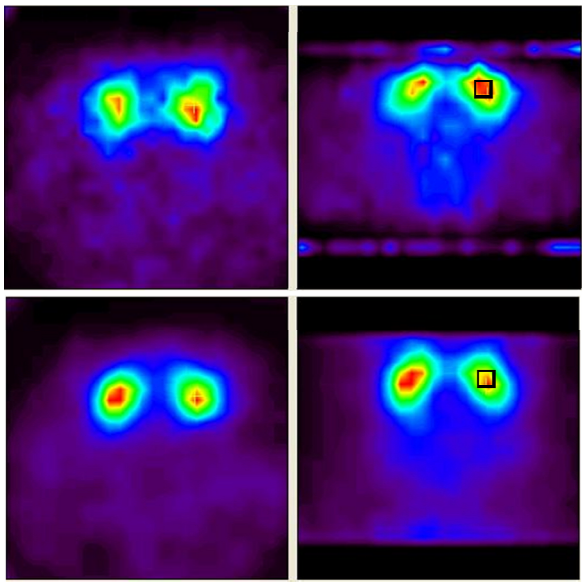

Figure 64 Improvement after (bottom) efficiencies correction in a ^{11}C-Raclopride study. The ROIs shown had a 15% drop in pixel standard deviation after correction

The correction was also qualitatively assessed for a rat brain study with a 1 mCi injection of 11C-Raclopride. The images in Figure 64 were reconstructed for 100 iterations and post-smoothed, and ROIs drawn on the striata showed up to a 15% drop in pixel standard deviation after correction.

Influence of statistical quality of data

Based on the results of the study described in 3.3.2B, 10M counts were simulated in the probability matrix. To ascertain the influence of the statistical quality of the efficiencies phantom, a 13GB ^{18}F-FDG dataset (acquired at rates <5000 kcps) was split to produce efficiencies sinograms at 3 statistical levels – 13GB (high, mean of ~700 true counts per LOR), 4 GB (med) and 1GB (low). The sinograms to be reconstructed were acquired on a separate day using the same uniform phantom. Two datasets were acquired, with ~65 counts/LOR (high) and 3 counts/LOR. The latter was equivalent to a 5-min time frame of a typical study in the RatCAP with a 250μCi injection. This is summarized in the Table VI below.

Trues/LOR	Efficiencies phantom Mean ± std of non-zero values	Phantom data to be reconstructed Mean ± std of non-zero values
High	705±387	65±43
Med	240±192	X
Low/ Typical	65±39	3±2

Table VI Statistics in 1) efficiencies phantom and 2) data to be reconstructed

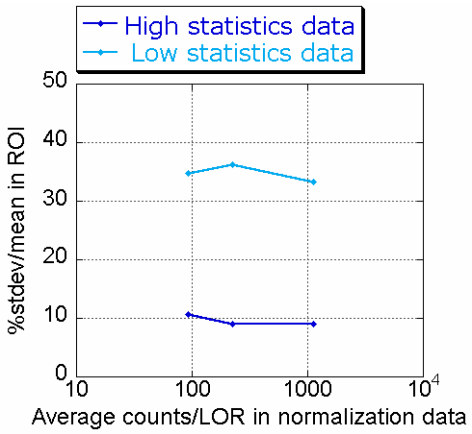

Figure 65 Influence of statistical quality of normalization data

High and low statistics sinograms evaluated. Correction does not seem to be affected by the statistical quality of the normalization data

Observations:

Normalization brought about a larger improvement in the high statistics dataset compared to the "typical" dataset. At 100 iterations, a 35-40% improvement in ROI standard deviation was seen in the high statistics data, and a 10-15% improvement in the low statistics data. Furthermore, this method seems mostly independent of the statistical quality of the normalization data, as shown in Figure 65. This can possibly be explained by the fact that the RatCAP is made up of only 384 detector channels, with a small degree of variability between them. The relatively large number of LORs compensate for the low statistics overall.

3.4.5 Absolute calibration

RatCAP images were calibrated using the cylindrical phantom described previously, filled homogenously with 2GB ^{18}F-FDG solution. Five aliquots of the solution were also measured using a calibrated well counter. The resulting sinograms had >100 counts/LOR. Images were reconstructed using the standard protocol and post smoothed. The ROI count rates obtained from the image were decay corrected to the start of the scan by integrating the area under the decay curve. Large ROIs were drawn on the reconstructed images of the calibration phantom for increased accuracy, and the ratio of the well counter-measured values to the ROI values was used as the calibration factor for subsequent images. The method was validated using a fast decaying phantom filled with 9.8μCi/cc of ^{11}C-Raclopride. The phantom was scanned for 5 half-lives and typical ROI sizes (size of the striatum of the rat) were plotted after decay correction and calibration. Error bars were obtained from ROIs placed at 3 different locations. A maximum of 7% bias was observed for ROIs placed at a distance transaxially and axially from the cFOV. Figure 66 shows the flat calibrated curve up to 5 half lives of the tracer.

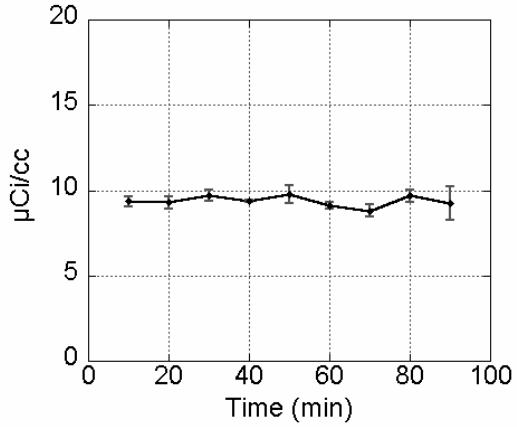

Figure 66 Testing calibration using fast-decaying phantom study

Section Conclusion

PET reconstruction and correction methods are known to be task-dependent, and the efforts made in this section have been geared towards dopamine receptor imaging with the RatCAP using ^{11}C-Raclopride. Numerous other consistency checks have been performed to ensure reliability and reproducibility for other tasks as well which will be redundant here. Instead, a select number of phantom and animal imaging results will be presented in the next section to demonstrate the imaging capabilities of the RatCAP.

4. Imaging Results

4.1 Performance Analysis

This section presents a performance evaluation of the RatCAP system using standard criteria. A comparison with existing PET systems will be provided when possible. Efforts have been made to comply with NEMA [220] standards for performance measurements as far as possible, but due to the unconventional geometry of the RatCAP and the fact that the NEMA standards for small animal systems was only recently published, the experiment designs may not be identical.

4.1.1 Coincidence sensitivity

The absolute sensitivity of the RatCAP was measured using a ~30 μCi ^{22}Na point source encapsulated in a stainless steel sleeve. The sleeve was assumed to be sufficiently thick to annihilate all photons from the source. The absolute activity level for the ^{22}Na source was obtained by counting it in a calibrated ion chamber. No decay correction was performed for the duration of the measurement as it was assumed to be negligible compared to the half life of ^{22}Na. Next, the source was placed in the axial and transaxial center of the RatCAP using a hollow plastic phantom with a hole in the center. 500MB of data was acquired for a total of 4 million true coincidences (<3% randoms). A measurement of the background activity was made and subtracted from the source measurement to account for the intrinsic radioactivity of the LSO scintillator. The standard time window ($2\tau=\pm 9$ ns) and LLDs (350 keV) were used for both measurements, and no ULD was applied. The rate of true coincidences estimated by the coincidence processor was divided by the well counter-measured value to obtain the %sensitivity for the standard operating settings. The use of a low-rate source ensured that the data was not contaminated by dead time or other rate-dependent effects. Sensitivity was measured only at the axial and transaxial center of the tomograph. The 5 mm crystal version of the RatCAP had an absolute sensitivity of ~0.3%, and the upgrade to the 8 mm crystals enhanced this value to ~0.8%. This is consistent with simulated measurements.

Crystal length	GATE (T + S)	SimSET (T + S)	Measured (T+S)
5mm	0.31217	0.324	0.30
8mm	0.70123	0.768	0.756

Table VII Comparison of theoretical and simulated coincidence sensitivities

A majority of existing small animal PET systems claim to have better sensitivity at the cFOV, typically in the 3%-10% range. In case of the RatCAP, this was a deliberate compromise in order to meet the other design goals, i.e. reduced size and weight.

4.1.2 Count rate performance

A NECR measurement was carried out with the 8mm crystal version of RatCAPv2. Two phantoms with a combined volume that complied with NEMA recommendations were used for the measurement. The NEMA rat-sized phantom is solid, right circular cylinder with a diameter of 5 +/- 0.05 cm and a length of 15 +/- 0.05 cm. Due to the RatCAP's unconventional geometry, a smaller "head" phantom had to be used for the imaging FOV, and a separate "body" phantom represented the OOFOV activity. The dimensions and volumes of the phantoms are in Table VIII below.

	Head phantom	Body phantom
Outer diameter (cm)	3.79	6
Inner diameter (cm)	3.53	5.6
Inner Length (cm)	2.35	13.6
Liquid volume (cc), weighed	20.95	348.2

Table VIII NECR phantom sizes

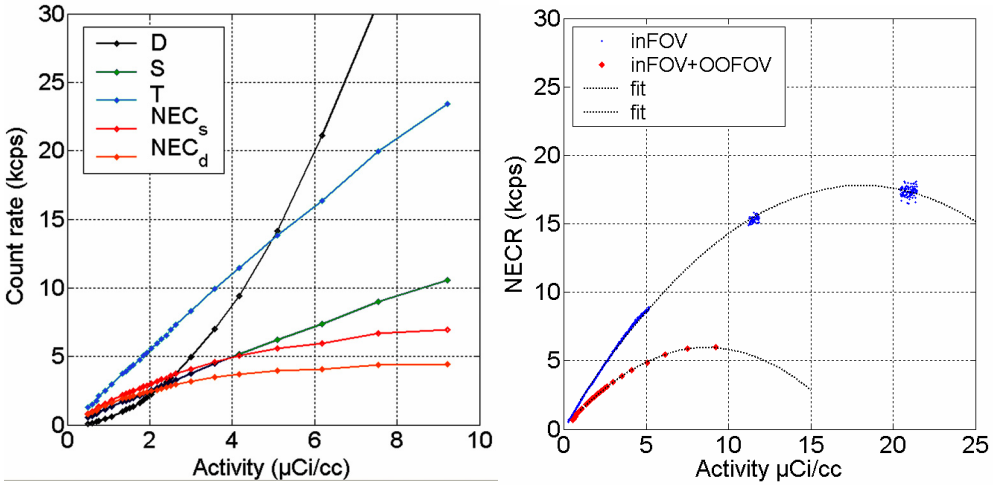

Figure 67 Noise Equivalent Count Rate Curves

(left) Count rate curves at 317 keV showing a peak NEC of 8.3 kcps @ 6.9 µCi/cc using the singles-based randoms estimate and 5.5 kcps @ 5.3 µCi/cc using the delayed channel estimate.

(right) Comparison of NECR using LLD = 387 keV with and without activity outside the FOV. Randoms and scatter from outside the FOV reduce the NECR by a factor of >4.

While NEMA recommends that a high activity source be placed within a cylindrical hole parallel to the central axis at a small radial distance from it, the RatCAP procedure is to uniformly fill the entire phantom with a fast-decaying source. For the results presented here, 3.4 mCi of ^{11}C solution was divided among the 2 phantoms such that the activity concentration in both the phantoms was 9.21 μCi/cc.

Data was acquired using $\tau = \pm 9$ ns at three LLD voltages equivalent to 317, 387 and 458 KeV. A separate file was acquired every 5 minutes (frequency increased to every minute when the peak NECR was expected) for a total of 100 minutes (or 5 half lives). At the end of the study, the count rate at 317 KeV was 100 kcps. Prompts and delayed count rates were calculated. The scatter fraction was estimated from simulations of an identical phantom at each threshold, and assumed to be constant at all rates. The NECR was calculated for two cases – one assuming a noisy randoms estimate (i.e. the measured delays) and the other using the same values, but calculating NECR with k=0. Similar to the NEMA acquisition procedure, each point on the curve was obtained from a measurement with >35,000 prompt coincidences. Table IX contains the observations from the three sets of curves. Although the scatter and randoms fractions were higher for the lowest LLD setting, the peak NECR of 8.3 kcps was observed at 317 KeV as shown in Figure 67. As shown in the figure, in the absence of background noise from OOFOV, the NECR would be higher by a factor of >4. It is encouraging to note that the peak NECR is achievable for typical studies in the RatCAP, since it occurs between 5 and 7.5 μCi/cc within an LLD range of 300 - 450 KeV, which translates to an injected dose of 1.5 – 2.25 mCi in a 300 g rat.

	317 KeV	**387 KeV**	**458 KeV**
Peak NEC_s	**8.3 kcps** @ 6.9 μCi/cc	4.4 kcps @ 7.4 μCi/cc	3.1 kcps @ 7.2 μCi/cc
Peak NEC_d	5.5 kcps @ 5.3 μCi/cc	3.0 kcps @ 6.5 μCi/cc	2.1 kcps @ 6.1 μCi/cc

Table IX Table of NECR values

The Peak NEC_s can be obtained using a noiseless randoms estimate, whereas the Peak NEC_d is the maximum NECR achievable using the delayed window (noisy)

4.1.3 Spatial resolution

A ^{68}Ge point source < 1mm in size, embedded in a metal holder was used for resolution measurements. It was placed within a plastic phantom with holes for the source drilled into it at the center, and then at distances 2 mm apart from 4 mm to 16 mm. >1M prompt coincidences were acquired in each case. 2D-FBP was performed using an unapodized filter on the randoms-subtracted sinograms. FWHMs were measured from Gaussian fits on 2-pixel wide (2.6 mm) profiles about the source in two orthogonal directions.

For the MLEM reconstruction, the sinograms of the ^{68}Ge point source were added to separately acquired sinograms of a uniformly filled phantom, so as to accurately reconstruct the source considering the non-negativity constraint of MLEM. The ratio of source:

background was 10:1. Since the plastic phantom served as an attenuating media for the photons from the point source, adding the sinograms in this manner was equivalent to a combined acquisition except for the negligible randoms contribution. The point source size was not deconvolved for these measurements.

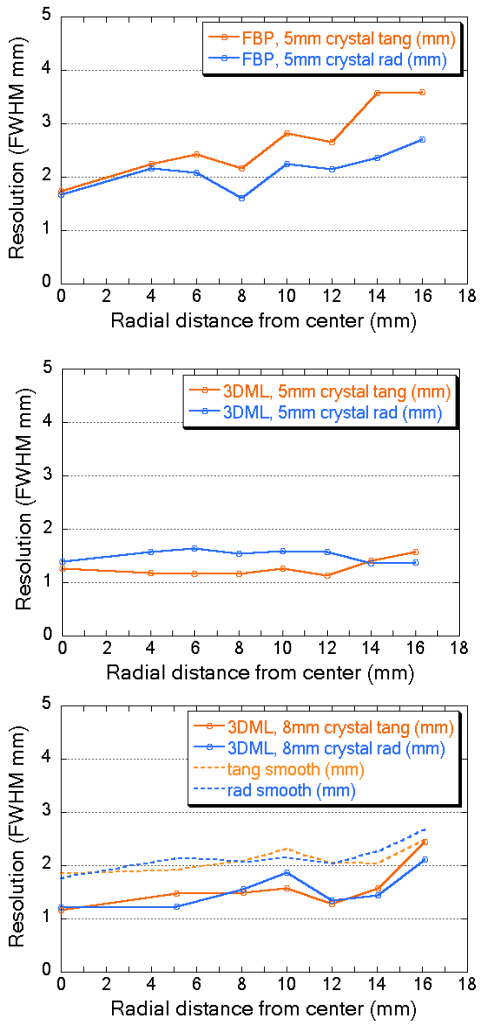

Figure 68 RatCAP Spatial Resolution
(top) 2D-FBP, 5mm crystals. (center) 3D-MLEM, 5mm crystals. (bottom) 3D-MLEM, 8mm crystals. FBP clearly outperforms MLEM, and the MLEM reconstruction results in equivalent resolution properties for both crystal lengths.

Figure 68 shows spatial resolution measurements for the 5 mm and 8 mm crystal versions of the RatCAP using 2D-FBP as well as 3D-MLEM. The MLEM reconstruction has uniform resolution properties throughout the FOV, and is able to resolve smaller structures even at the edge compared to FBP at cFOV. Due to accurate system modeling with MLEM, there is no parallax effect with the longer 8 mm crystals, as is evident from the comparison of the plot

from the 5 mm crystal version. The point at 16 mm on that plot is at the very edge of the FOV, and shows slight resolution degradation due to a ring artifact on the profile axis.

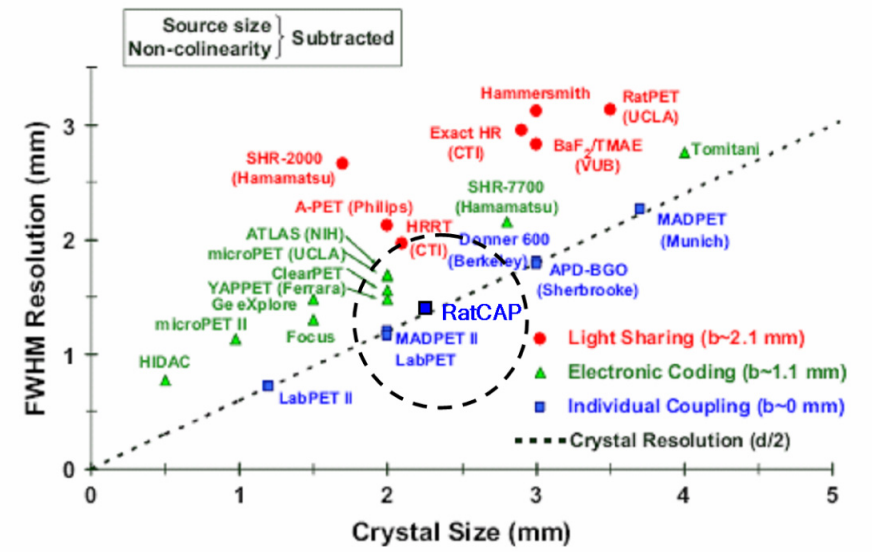

Figure 69 Comparison of spatial resolution for state-of-the-art PET scanners
Obtained from [221]. The dashed line represents the geometric resolution which is equal to half the detector size. The dashed circle highlights the addition of the RatCAP to the original chart.

The resolution of the RatCAP is comparable with other scintillation detector-based systems of its generation due to the small size of its individual detector elements and the use of one-to-one coupling. Figure 69 shows a comparison of some well-known small animal PET scanners using different readout strategies. The RatCAP can be placed right in the center of the field, since its reconstructed resolution has been measured to be almost equivalent to its intrinsic resolution represented by the black line.

4.2 Phantom Studies

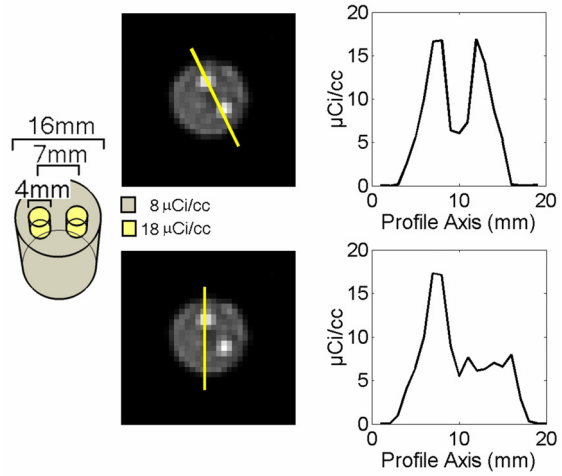

Figure 70 Rat striatum phantom study showing accurate contrast recovery in the striatum and cerebellum compartments

4.2.1 Striatum phantom study

As discussed in Section 3.1, one of the main applications of the RatCAP involves imaging of dopamine D2 receptors in the striatal ROI. The receptor binding potential (BP) is approximated by measuring the ratio of the striatal region to a region with non-specific binding; typically the cerebellum. A phantom that simulates these two compartments has been custom built as illustrated in Figure 70, and was used to evaluate the overall imaging performance of the RatCAP. It consists of two cylindrical striatum compartments placed 0.7 cm apart within a larger cerebellum cylinder. The outer cylinder is 1.6 cm in diameter and 1 cm long, while the inner cylinders are 0.4 cm in diameter and 0.5 cm long. ^{18}F-FDG solution was inserted into both the striatum compartments, then diluted and inserted into the larger cerebellum compartment to reproduce a realistic imaging situation. Aliquots measured in a previously calibrated well counter read 18.32 µCi/cc and 7.92 µCi/cc in the striatum and cerebellum compartments respectively. Images were reconstructed and calibrated using the standard protocol. The recovery coefficient was determined for ROIs on the striata and cerebellum as the ratio of the calibrated maximum pixel ROI values to the measured values of the aliquots. The standard error in the ROI was used as a measure of variability. The recovery coefficient for the striatal ROIs was 0.997±0.22 and cerebellum was 1.03±0.095. Image profiles in Figure 70 show accurate reproduction of contrast measured in the well counter without artifacts. The phantom size, including smaller regions, has been accurately reproduced in the reconstructed image as shown in Figure 71. The results from this phantom study were encouraging in terms of the exactness of the measured ROIs, but it is vital that this high performance holds up in count-limited measurements as well.

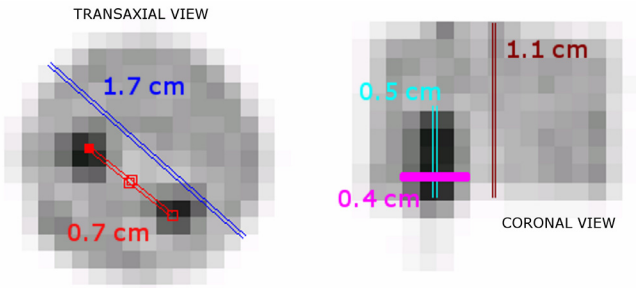

Figure 71 Rat striatum phantom - Dimension measurements in reconstructed image

4.3 Imaging Studies

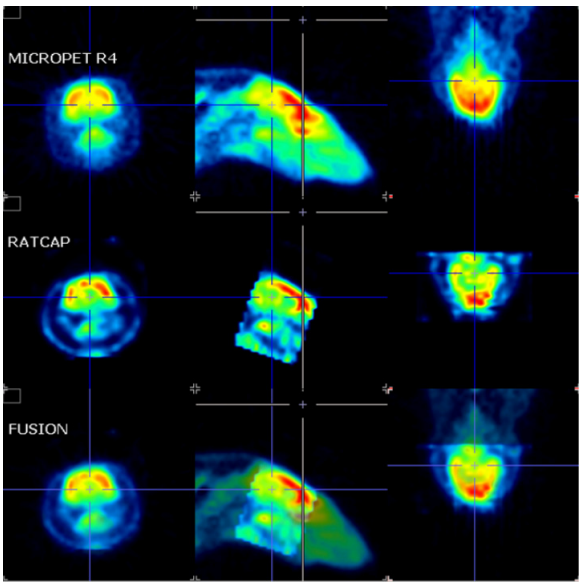

Figure 72 Quantitative comparison of RatCAP and microPET R4 images using ^{18}F-FDG
Note that the RatCAP covers only 2 cm of the microPET's axial FOV. The jagged edges are due to rotation during coregistration

4.3.1 ^{18}F-FDG study – Comparison with microPET R4

Figure 72 shows a comparison of an ^{18}F-FDG study in the RatCAP scan with the commercial animal PET system available at BNL, the microPET R4 [222]. A ~300g Sprague Dawley rat was injected with 1.0 mCi of ^{18}F-FDG solution at (say) time t_0. After a 1-hour long uptake period, it was scanned in the RatCAP for 30 minutes. Next, it was scanned in the microPET R4 for 30 minutes, followed by another scan in the RatCAP for the last 36 minutes. Both RatCAP images were decay corrected to the start time of the microPET study, and the three images were coregistered. The color scales in the figure are mapped to the same value, and it shows a good quantitative agreement between the calibrated RatCAP image and the microPET output, except for slightly higher image noise in the case of the RatCAP. The noise

among the ROI voxels was compared for a 0.015 cc ROI on the striata and found to be ~7% for the microPET image, ~14% for the first RatCAP image and ~20% for final image due to decay of the isotope.

4.3.2 ^{18}F-Fluoride bone study in the mouse

To investigate the feasibility of imaging even smaller structures with the RatCAP, a bone scan of a 30g mouse was performed with a 250 μCi injection of ^{18}F-Fluoride. Only the head of the mouse was scanned for 30 minutes. Reconstructed transverse slices of the skull are shown in Figure 73.

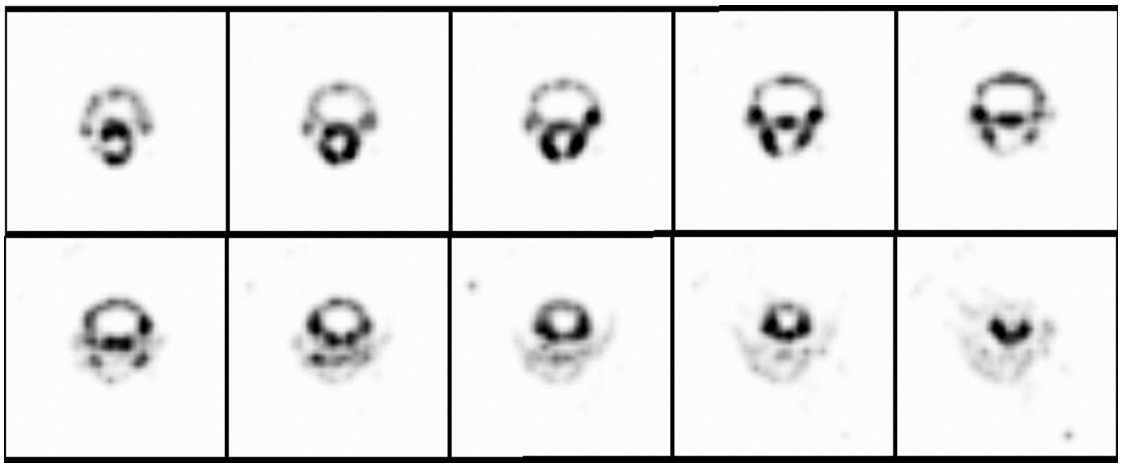

Figure 73 Transverse slices of the mouse skull imaged in the RatCAP using ^{18}F

4.3.3 Imaging the awake animal with ^{11}C-Raclopride

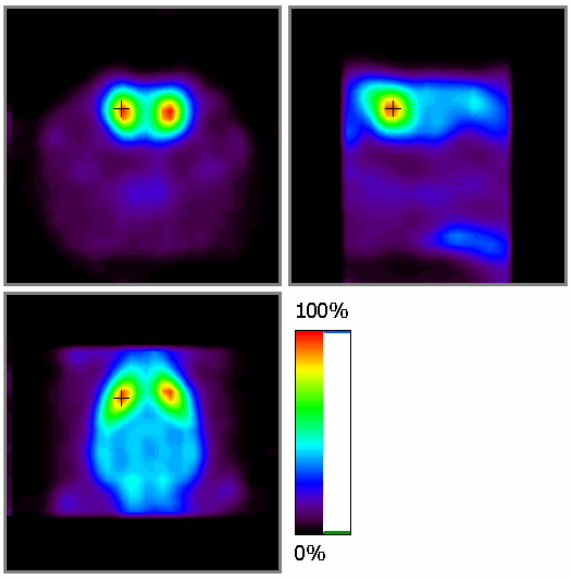

Figure 74 ^{11}C-Raclopride static study on an awake animal

Static Imaging

A high statistics measurement using ^{11}C-Raclopride was performed to obtain the best image quality feasible with the RatCAP for this specialized imaging task. A 278g Sprague Dawley female rat was injected with 1.3 mCi (5 nmol/kg) ^{11}C-Raclopride and scanned awake in the RatCAP for 1 hour to obtain the image in Figure 74 below. Figure 75 shows the sensitivity of the RatCAP to specific binding of ^{11}C-labelled raclopride in a "blocking study". Under baseline conditions (top), normal uptake in the striatum was observed. For the blocked condition below, pre-treatment with 2mg/kg unlabelled raclopride blocked ^{11}C-Raclopride binding, thus decreasing the PET signal only in the specific binding region.

^{11}C-Raclopride studies are routinely performed in the RatCAP on unanesthetized as well as anesthetized animals. Since the influence of anesthesia is too complex to evaluate qualitatively in a static image, the time-varying tracer distributions within the ROIs for awake and anesthetized rats were compared as discussed below.

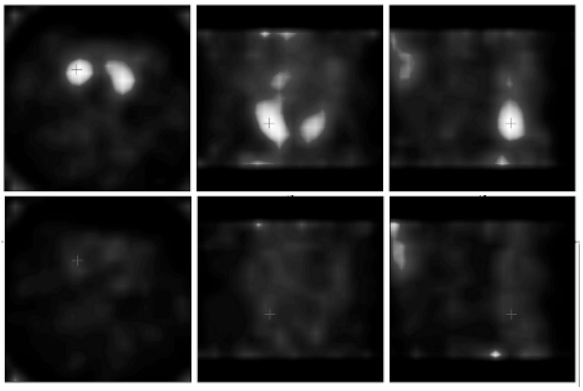

Figure 75 ^{11}C-Raclopride Blocking study
(top) baseline, injection of ^{11}C-Raclopride followed by (bottom) unlabelled raclopride

Dynamic Imaging

Typically, separate sinograms are acquired for each time frame and independently reconstructed. ROIs on the striatum (ST) and cerebellum (CB) for each frame are plotted versus time on the x-axis. Cerebellar regions are acquired as a reference region, or a region that does not contain D_2-receptor binding sites. This has been widely used in lieu of arterial blood sampling in PET studies [223-225]. An approximation of binding potential (BP) is obtained from the following relation:

$$BP \approx \frac{ST}{CB} - 1$$

over the last 30 minutes of the scan.

ROI sizes

A 3 mm diameter cylindrical ROI spanning 3 axial planes (3 mm) is typically used for the striatum in the RatCAP protocols. This is sufficient to cover a large fraction of the region, but excludes the edges to avoid potential partial volume effects. Following standard small animal PET procedures, the cerebellar ROI is larger (5mm dia, 3mm length) for a low-noise estimate. The size of each time frame increases with time, to achieve uniform noise properties with radiotracer decay.

Experimental design I

Five rats for were first scanned awake and then ~1 hour later under anesthesia. Injected doses ranged from 250 μCi – 1 mCi, with injected masses of 5 nmol/kg. As shown in Figure 76, the overall uptake was seen to be higher in the anesthetized animal compared to the awake animal, suggesting that the clearance of tracer is slower under anesthesia. Although the binding potential was observed to be higher in all of the awake studies compared to anesthetized studies in the same animal, the difference in the binding potential was not significant with n=5 (p=0.17, paired t-test).

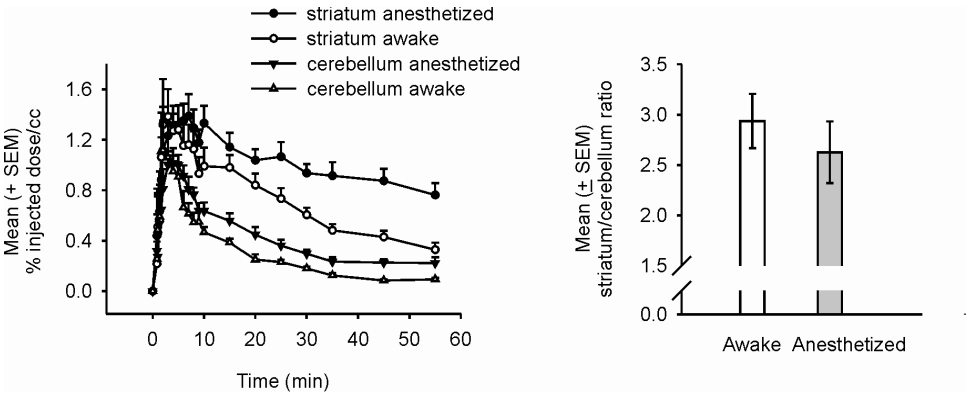

Figure 76 Time-activity curves for awake and anesthetized rats scanned in the RatCAP

Continuous Infusion Paradigm

Recent studies have been carried out using a combined bolus plus constant infusion paradigm [226] for radiotracer administration, which results in a flat BP vs. time curve at equilibrium. Once equilibrium is achieved, the ^{11}C-Raclopride BP can be calculated from the striatum-cerebellum ROI concentration ratio. If a stimulus is applied to perturb the equilibrium state, the change in specific binding of the tracer can be detected without the need for a separate study. This is a promising technique to evaluate the effect of pharmacological stimuli during a single study, and especially in case of the RatCAP to additionally evaluate behavioral/pharmacological stimuli in the awake rat.

Experimental design II

An optimized B/I protocol was experimentally determined, then fixed for all studies. In the awake state, it was found that steady state was achieved with a 40% bolus injection, followed by continuous infusion of 60% of the radiotracer over 60 mins. A different protocol was required for anesthetized animals (30% bolus, 70% infused), most likely due to the slower clearance rate as seen in the previous experimental paradigm.

An infusion pump was used to administer the dose through an intravenous catheter. The bolus portion of the dose was delivered at a high rate over 1 min. The pump speed is then reduced to deliver the remaining dose uniformly over 60 min. Images were reconstructed and time-activity curves generated similar to the procedure detailed above. Figure 77 (left) shows a typical continuous infusion time-activity curve without an intervention which achieves steady state in ~20 mins.

The feasibility of detecting changes in specific binding using this protocol was evaluated with a bolus injection of 2mg/kg unlabelled raclopride at 27 minutes to displace the ^{11}C-labelled raclopride. Since ROI values were observed to have reached a clearance rate close to 0 for the control studies by that time, this intervention was expected to disturb the steady state. As expected, a huge dip is seen in the curve at that point in Figure 77 (right).

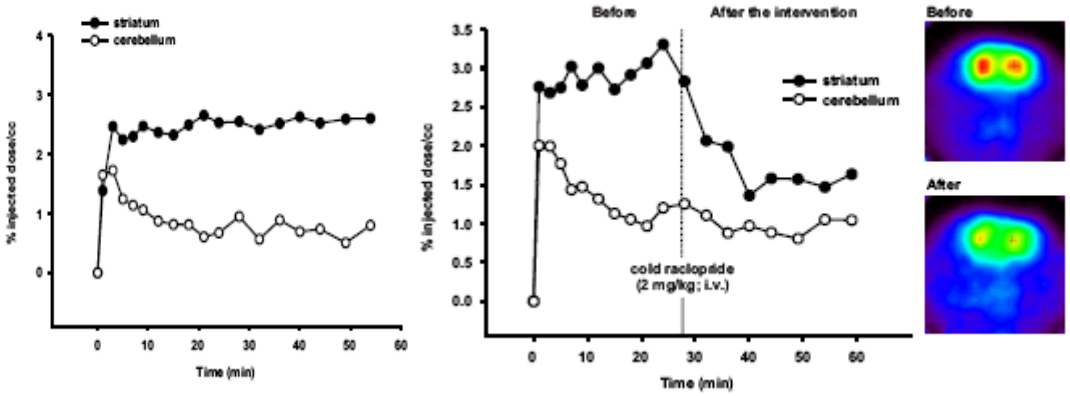

Figure 77 Continuous infusion studies with RatCAP

5. Conclusions

5.1 Future Directions

5.1.1 Continuous infusion studies – bootstrap analysis

As mentioned in the previous chapter, the continuous infusion tracer delivery paradigm would potentially allow the detection of changes in the specific binding of radiotracer in response to pharmacological or behavioral stimuli during a single study. We have successfully detected a 60% change in ^{11}C-Raclopride binding due to competition with unlabelled raclopride (see Figure 77), but the RatCAP's sensitivity to changes of a smaller magnitude needs to be assessed. Detecting subtle changes is a challenge given the relatively low sensitivity of the RatCAP, using standard injected doses. One method to evaluate the accuracy of a measurement from a single (or a few) acquisition is the bootstrap approach [227-229], which can be used to generate multiple statistically equivalent bootstrap replicates from the original sample(s). Our initial studies using this approach are described below.

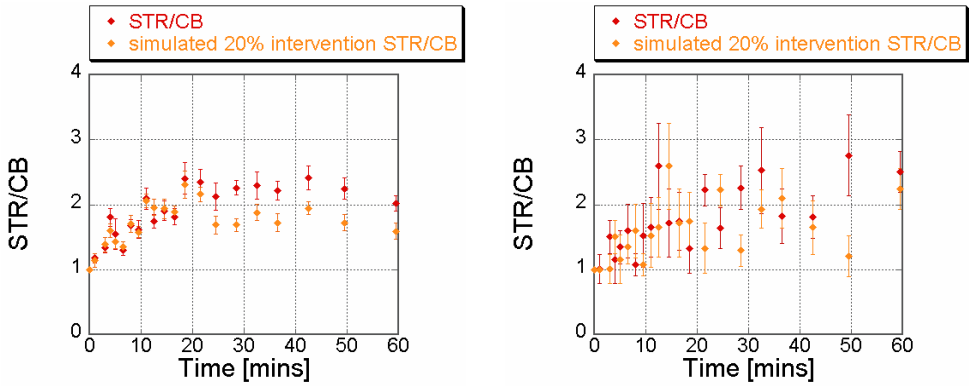

Figure 78 Bootstrapping to estimate accuracy of time-activity curves
(left) injected dose = 1.3 mCi. (right) injected dose = 0.13 mCi

Bootstrap approach

Bootstrap approaches in the literature can be classified as parametric [228] or non-parametric [229], where the later makes no assumptions about the underlying distribution of the data. Since RatCAP data can realistically be assumed to be Poisson, the Haynor-Woods [228] parametric approach has been implemented in our case, where a Poisson random number generator with parameter = 1 is run for every single event for B bootstrap samples. Our implementation of the method has been validated using phantoms, where the original

data was split into a number of parts to determine the true image variance, which agreed with the bootstrap-estimated variance of a single part within 1%.

Estimating accuracy of time-activity curves

The uncertainty in the binding potential estimate due to factors such as injected dose and noise propagation from the reconstruction and correction methods was evaluated in this preliminary study. The red curves in Figure 78 show the original samples (injected doses of 1.3 and 0.13 mCi) with the error bars estimated using the bootstrap approach (B = 10). The orange curves show a simulated intervention, obtained by randomly rejecting 20% of the original coincidences 25 minutes into the study. The values at 5 points before the intervention were compared to 5 points after the intervention in both studies using a two-tailed, paired t-test. This comparison was performed for each bootstrap replicate, with the assumption that each replicate represented a separate experiment. 60% of the p-values showed a statistically significant difference after intervention with the 1.3 mCi injection, but not a single p-value was significant in the in the low statistics curve. In a separate study with varying degrees of simulated interventions, it was found that changes <15% could not be detected with certainty using the RatCAP.

Discussion

The bootstrap replicates reproduce only the Poisson variance in the data, and in reality there will be large inter-subject biological differences and other variables. However, assuming steady state has been reached in the tracer kinetics, the bootstrap estimate of error should be able to predict the best-case detection capability of the RatCAP. Any additional uncertainty between the points on the curve after steady-state must be due to other sources of variance. Thus, if a ≥15% change can be detected assuming only Poisson errors with >1 mCi injected, the RatCAP will have much lower sensitivity to changes in a realistic experiment. A comprehensive analysis of the data acquisition and processing chain to determine the sources of image noise variance will allow us to improve our detection capability and reach a consensus on an optimized approach for quantitative neuroreceptor imaging using the RatCAP.

5.1.2 Dynamic (4D) image reconstruction

The reconstruction of individual time frames in a dynamic sequence is sub-optimal for a number of reasons:

1. Splitting data into separate time frames prior to reconstruction results in noisy images.
2. Frame-wise binning imposes a temporal limit on the dynamics quantifiable by a tomograph. Although an increasingly high number of time frames may be used, this makes individual frames smaller and hence, noisier.

A wide range of methods have been proposed in the literature to perform spatiotemporal (4D) PET image reconstruction. One class of methods estimates temporally varying basis functions [113, 114, 230]while another estimates time-dependent kinetic (functional) parameters directly from the data [231]. These approaches would be ideal for the RatCAP in the case of ^{11}C-Raclopride studies with a fixed object, which would allow a number of simplifying assumptions in the generation of basis functions and the time-dependent probability matrix. The implementation of these methods is expected to improve the chances of detection of subtle changes in specific binding described in the previous subsection.

5.2 Discussion

Research in PET, especially in the case of small animal imaging, is an ongoing pursuit of high resolution and high sensitivity. An effort has been made and presented in this dissertation to maximize the benefit of the Monte Carlo image reconstruction approach to optimize these two parameters for typical PET studies using the RatCAP. System operation, data acquisition and processing protocols have been optimized within the limitations posed by the RatCAP's design and specific application. A combination of empirical measurements and Monte Carlo simulations has been used to thoroughly understand the system and compensate for inadequacies. Some lessons learned are summarized below:

Data acquisition and calibration

- APD gains are sensitive to temperature fluctuations, and the selection of LLD must take into account the 3% per degree change in temperature. Since time resolution depends on LLD (see Figure 30), this becomes even more crucial.
- Although dead time is not a problem, calibration phantom data must be acquired at singles rates <1Mcps for reduced multiples fraction. This is equivalent to <200 μCi in the uniform cylindrical phantom that fills the FOV ("head" phantom).

System modeling

- Both Monte Carlo packages reproduce measured data within a reasonable amount of error, but SimSET is faster than GATE by a factor of 10, without the use of variance reduction techniques which could be employed to bring about additional improvements in simulation time. The use of symmetries speeds up the simulation by a factor of 16.
- Simulating scatter with an LLD of 350 keV doubles the storage size of the matrix but brings about essential improvements in the reconstruction as shown in Figure 40 and 57-60.
- Higher statistics in the matrix also increase the storage size, but improve the accuracy of values in large ROIs (which might be susceptible to edge effects). This could be useful for noisy datasets.

Image reconstruction

- The RatCAP FBP algorithm can successfully be used for a first-pass reconstruction, but higher resolution and quantitative accuracy is achieved with RC-MLEM.
- For ROI analyses on small distinct objects in the presence of background activity, images must be reconstructed for at least 1000 MLEM iterations and post-smoothed to control noise.
- The size of the post-smoothing filter can be varied between 1.5 mm and 2.0 mm depending on the object being reconstructed.

Quantitative corrections

- Randoms - At detected singles rates below ~500 kcps, the singles-based method provides significantly better noise performance compared to the delayed channel approach. The

values of both estimates are accurate within 5%. At higher rates, the singles-based randoms estimate would need to be scaled to account for the reduction in prompt (and true) coincidences due to multiples.

- Attenuation - The CT-based attenuation correction is promising, provided that a method to control image noise variance is developed for the use of a fixed system response model for all subjects. One idea could be the use of an average of multiple attenuation maps in the probability matrix simulation. Another could be smoothed attenuation maps that preserve only areas with high structural detail. Alternatively, since the use of a CT map resulted in an almost uniform ~5% increase in the FDG rat brain image compared to a homogenous map, ROIs could be scaled up by an empirically determined factor, or this effect could be ignored in favor of reduced image noise variance.
- Scatter – The use of an accurate CT-based attenuation map brought about an improvement in scatter correction as well, but since the overall contribution of scatter in RatCAP images is small at 350 keV, the homogenous map is sufficient. The contribution of OOFOV scatter can be estimated by including the OOFOV region (front as well as back) with coarser discretization in the system model.
- Normalization – Low statistics normalization data are sufficient to correct for variations among detector efficiencies and bring about a significant qualitative as well as quantitative improvement in RatCAP images.

Imaging studies

- For a ^{11}C-Raclopride study in the RatCAP, contrast recovery of ~97% is expected, but image noise variance might be a concern with low injected doses. The selection of ROI could play a significant role.
- The use of newly-developed methods to reduce image noise variance, especially the reduced-variance randoms estimates, along with optimized reconstruction and post-smoothing should improve future results.

In summary, the feasibility of using the RatCAP for quantitatively accurate PET studies of the rat brain has been confirmed. The system is now routinely used for dynamic studies, and its performance has been shown to be on par with existing small animal PET systems. While the impact of this one-of-a-kind system on the field of preclinical imaging has yet to be realized, it is anticipated that imaging the animal awake and enabling correlations with behavior will open up a new realm of possibilities in quantitative neuroimaging.

Bibliography

[1] B. Bendriem and D. W. Townsend, *The theory and practice of 3D PET*: Springer, 1998.

[2] I. J. Hildebrandt, H. Su, and W. A. Weber, "Anesthesia and Other Considerations for in Vivo Imaging of Small Animals," *ILAR JOURNAL*, vol. 49, pp. 17, 2007.

[3] S. Momosaki, K. Hatano, Y. Kawasumi, T. Kato, R. Hosoi, K. Kobayashi, O. Inoue, and K. Ito, "Rat-PET study without anesthesia: Anesthetics modify the dopamine D_{<FONT SIZE='-1'>1</FONT>} receptor binding in rat brain," *Synapse*, vol. 54, pp. 207-213 %U http://dx.doi.org/10.1002/syn.20083, 2004.

[4] A. Matsumura, S. Mizokawa, M. Tanaka, Y. Wada, S. Nozaki, F. Nakamura, S. Shiomi, H. Ochi, and Y. Watanabe, "Assessment of microPET performance in analyzing the rat brain under different types of anesthesia: comparison between quantitative data obtained with microPET and ex vivo autoradiography," *NeuroImage*, vol. 20, pp. 2040-2050, 2003.

[5] W. Hassoun, M. Le Cavorsin, N. Ginovart, L. Zimmer, V. Gualda, F. Bonnefoi, and V. Leviel, "PET study of the [11 C] raclopride binding in the striatum of the awake cat: effects of anaesthetics and role of cerebral blood flow," *European Journal of Nuclear Medicine and Molecular Imaging*, vol. 30, pp. 141–148, 2003.

[6] L. L. Howell, J. M. Hoffman, J. R. Votaw, A. M. Landrum, and J. F. Jordan, "An apparatus and behavioral training protocol to conduct positron emission tomography (PET) neuroimaging in conscious rhesus monkeys," *Journal of neuroscience methods*, vol. 106, pp. 161–169, 2001.

[7] P. Vaska, C. Woody, D. Schlyer, S. Shokouhi, S. Stoll, J.-F. Pratte, P. O'Connor, S. Junnarkar, S. Rescia, B. Yu, M. Purschke, A. Kandasamy, A. Villanueva, A. Kriplani, V. Radeka, N. Volkow, R. Lecomte, and R. Fontaine, "RatCAP: Miniaturized Head-Mounted PET for Conscious Rodent Brain Imaging," *IEEE Trans Nuc Sci*, vol. 51, pp. 2718-2722, 2004.

[8] P. Vaska, C. Woody, D. Schlyer, V. Radeka, P. O'Connor, J.-F. Pratte, S. Shokouhi, S. Stoll, S. Junnarkar, M. Purschke, S.-J. Park, S. Southekal, V. Dzhordzhadze, W. Schiffer, J. Neill, M. Murphy, T. Aubele, R. Kristiansen, A. Villanueva, S. Boose, A. Kandasamy, B. Yu, A. Kriplani, S. Krishnamoorthy, R. Lecomte, and R. Fontaine, "Initial Performance of the RatCAP, a PET Camera for Conscious Rat Brain Imaging," *IEEE NSS/MIC Conference Record*, 2005.

[9] P. Vaska, C. L. Woody, D. J. Schlyer, V. Radeka, P. O'Connor, S.-J. Park, J.-F. Pratte, S. Junnarkar, M. Purschke, S. Southekal, S. Stoll, W. Schiffer, D. Lee, J. Neill, D. Wharton, N. Myers, S. Wiley, A. Kandasamy, J. Fried, A. Kriplani, and R. Lecomte, "Performance Enhancement of the RatCAP Awake Rat Brain PET System," *IEEE NSS-MIC Conference Record*, 2006.

[10] P. Vaska, C. Woody, D. Schlyer, J. F. Pratte, S. Junnarkar, S. Southekal, S. Stoll, D. Schulz, W. Schiffer, and D. Alexoff, "The design and performance of the 2 nd-generation RatCAP awake rat brain PET system," in *IEEE Nuclear Science Symposium Conference Record, 2007. NSS'07*, vol. 6, 2007.

[11] D. Schlyer, P. Vaska, C. Woody, D. Schulz, S. Junnarkar, S. Southekal, S. H. Maramraju, W. Schiffer, and D. Alexoff, "Comparison of [11C] raclopride kinetics in awake and anesthetized rats using the RatCAP Awake Rat Brain PET System," in *Society of Nuclear Medicine Annual Meeting Abstracts*, vol. 49: Soc Nuclear Med, 2008, pp. 208P.

[12] S. Shokouhi, "Image Reconstruction and System performance Simulations of Rat Conscious Animal PET (RatCAP)," in *Biomedical Engineering*, vol. Ph.D. Stony Brook: Stonybrook University, 2004.

[13] J. Langner, "Event-Driven Motion Compensation in Positron Emission Tomography: Development of a Clinically Applicable Method," Faculty of Medicine Carl Gustav Carus, University of Technology Dresden, Germany, 2008.

[14] R. E. Carson, "Tracer kinetic modeling in PET," *Positron Emission Tomography, Basic Science and Clinical Practice*.

[15] M. A. Ariano, *Receptor localization*: Wiley-IEEE, 1998.

[16] C. D. Anderson, "The positive electron," *Physical Review*, vol. 43, pp. 491–494, 1933.

[17] W. H. Sweet, "The uses of nuclear disintegration in the diagnosis and treatment of brain tumor," *The New England Journal of Medicine*, vol. 245, pp. 875-878, 1951.

[18] C. A. Burnham, S. Aronow, and G. L. Brownell, "A hybrid positron scanner," *Physics in Medicine and Biology*, vol. 15, pp. 517–528, 1970.

[19] G. L. Brownell and C. A. Burnham, "MGH positron camera," in *Tomographic Imaging in Nuclear Medicine: The Proceedings of a Symposium Held September 15-16, 1972*, 1973.

[20] G. L. Brownell, J. A. Correia, and R. G. Zamenhof, "Positron instrumentation," *Recent advances in nuclear medicine*, vol. 1, 1979.

[21] *BNL2000bulletin*.

[22] D. A. Chesler, "Positron Tomography and Three-Dimensional Reconstruction," in *Tomographic Imaging in Nuclear Medicine: The Proceedings of a Symposium Held September 15-16, 1972*, 1973.

[23] C. S. Levin and E. J. Hoffman, "Calculation of positron range and its effect on the fundamental limit of positron emission tomography system spatial resolution," *Physics in Medicine and Biology*, vol. 44, pp. 781–800, 1999.

[24] M. E. Phelps, E. J. Hoffman, S. C. Huang, and M. M. Ter-Pogossian, "Effect of positron range on spatial resolution," *Journal of Nuclear Medicine*, vol. 16, pp. 649, 1975.

[25] J. S. Kim, J. S. Lee, K. C. Im, S. J. Kim, S.-Y. Kim, D. S. Lee, and D. H. Moon, "Performance measurement of the microPET focus 120 scanner," *Journal of Nuclear Medicine: Official Publication, Society of Nuclear Medicine*, vol. 48, pp. 1527-1535, 2007.

[26] A. H. Compton, "A quantum theory of the scattering of x-rays by light elements," *Physical Review*, vol. 21, pp. 483–502, 1923.

[27] M. E. Phelps, *PET*: Springer, 2004.

[28] R. Accorsi, L. E. Adam, M. E. Werner, and J. S. Karp, "Optimization of a fully 3D single scatter simulation algorithm for 3D PET," *Physics in Medicine and Biology*, vol. 49, pp. 2577 2598, 2004.

[29] T. Beyer, D. W. Townsend, T. Brun, P. E. Kinahan, M. Charron, R. Roddy, J. Jerin, J. Young, L. Byars, and R. Nutt, "A Combined PET/CT Scanner for Clinical Oncology," *J Nucl Med*, vol. 41, pp. 1369-1379, 2000.

[30] S. C. Strother, M. E. Casey, and E. J. Hoffman, "Measuring PET scanner sensitivity: relating countrates to image signal-to-noise ratios using noise equivalents counts," *IEEE Transactions on Nuclear Science*, vol. 37, pp. 783 788, 1990.

[31] J. M. Ollinger, "Model-based scatter correction for fully 3D PET," *Physics in Medicine and Biology*, vol. 41, pp. 153 176, 1996.

[32] C. C. Watson, D. Newport, and M. E. Casey, "A single scatter simulation technique for scatter correction in 3D PET," *Three-Dimensional Image Reconstruction in Radiology and Nuclear Medicine*, vol. 4, pp. 255 68, 1996.

[33] J. Seguinot, A. Braem, E. Chesi, C. Joram, S. Mathot, P. Weilhammer, M. C. Llatas, J. G. Correia, M. R. da Silva, F. Garibaldi, and others, "Novel geometrical concept of a high-performance brain PET scanner. Principle, design and performance estimates," *NUOVO CIMENTO-SOCIETA ITALIANA DI FISICA SEZIONE C*, vol. 29, pp. 429, 2006.

[34] A. P. Jeavons, R. A. Chandler, C. A. R. Dettmar, and O. P. Syst, "A 3D HIDAC-PET camera with sub-millimetre resolution for imagingsmall animals," *IEEE Transactions on Nuclear Science*, vol. 46, pp. 468–473, 1999.

[35] P. Vaska, A. Bolotnikov, G. Carini, G. Camarda, J. F. Pratte, F. A. Dilmanian, S. J. Park, and R. B. James, "Studies of CZT for PET applications," in *Nuclear Science Symposium Conference Record, 2005 IEEE*, 2005.

[36] D. L. Bailey, *Positron emission tomography*: Springer, 2005.

[37] J. S. Huber, W. W. Moses, M. S. Andreaco, and O. Petterson, "An LSO scintillator array for a PET detector module with depth of interaction measurement," *Nuclear Science, IEEE Transactions on*, vol. 48, pp. 684-688, 2001.

[38] M. Schmand, L. Eriksson, M. E. Casey, M. S. Andreaco, C. Melcher, K. Wienhard, G. Flugge, R. Nutt, C. T. I. P. E. T. S. Inc, and T. N. Knoxville, "Performance results of a new DOI detector block for a highresolution PET-LSO research tomograph HRRT," in *IEEE Nuclear Science Symposium, 1997*, 1997.

[39] S. I. Ziegler, B. J. Pichler, G. Boening, M. Rafecas, W. Pimpl, E. Lorenz, N. Schmitz, and M. Schwaiger, "A prototype high-resolution animal positron tomograph with avalanche photodiode arrays and LSO crystals," *European Journal of Nuclear Medicine and Molecular Imaging*, vol. 28, pp. 136–143, 2001.

[40] S. Surti, J. S. Karp, and G. Muehllehner, "Image quality assessment of LaBr3-based whole-body 3D PET scanners: a Monte Carlo evaluation," *Physics in Medicine and Biology*, vol. 49, pp. 4593–4610, 2004.

[41] A. Kuhn, S. Surti, J. S. Karp, G. Muehllehner, F. M. Newcomer, and R. VanBerg, "Performance assessment of pixelated LaBr 3 detector modules for time-of-flight PET," *IEEE Transactions on Nuclear Science*, vol. 53, pp. 1090–1095, 2006.

[42] W. H. Wong, N. A. Mullani, G. Wardworth, R. K. Hartz, and D. Bristow, "Characteristics of small barium fluoride (BaF2) scintillator for high intrinsic resolution time-of-flight positron emission tomography," *IEEE Transactions on Nuclear Science*, vol. 31, pp. 381–386, 1984.

[43] R. Lecomte, J. Cadorette, S. Rodrigue, D. Lapointe, D. Rouleau, M. Bentourkia, R. Yao, and P. Msaki, "Initial results from the Sherbrooke avalanche photodiode positron tomograph," *Nuclear Science, IEEE Transactions on*, vol. 43, pp. 1952-1957, 1996.

[44] Y. Shao, R. W. Silverman, R. Farrell, L. Cirignano, R. Grazioso, K. S. Shah, G. Vissel, M. Clajus, T. O. Tumer, T. O. Tumer, S. R. Cherry, and A, "Design studies of a high resolution PET detector using APD arrays," *Nuclear Science, IEEE Transactions on*, vol. 47, pp. 1057, 1051, 2000.

[45] M. Watanabe, H. Okada, K. Shimizu, T. Omura, E. Yoshikawa, T. Kosugi, S. Mori, T. Yamashita, and H. P. Kk, "A high resolution animal PET scanner using compact PS-PMT detectors," *IEEE Transactions on Nuclear Science*, vol. 44, pp. 1277–1282, 1997.

[46] Y. C. Tai, A. Chatziioannou, S. Siegel, J. Young, D. Newport, R. N. Goble, R. E. Nutt, S. R. Cherry, and others, "Performance evaluation of the microPET P4: a PET system dedicated to animal imaging," *Physics in Medicine and Biology*, vol. 46, pp. 1845–1862, 2001.

[47] S. Moehrs, A. Del Guerra, D. J. Herbert, and M. A. Mandelkern, "A detector head design for small-animal PET with silicon photomultipliers (SiPM)," *Physics in medicine and biology*, vol. 51, pp. 1113–1128, 2006.

[48] S. Surti and J. S. Karp, "Imaging characteristics of a 3-dimensional GSO whole-body PET camera," *Journal of Nuclear Medicine*, vol. 45, pp. 1040, 2004.

[49] M. Huisman, S. Reder, A. Weber, S. Ziegler, and M. Schwaiger, "Performance evaluation of the Philips MOSAIC small animal PET scanner," *European Journal of Nuclear Medicine and Molecular Imaging*, vol. 34, pp. 532-540 %U http://dx.doi.org/10.1007/s00259-006-0271-7, 2007.

[50] G. F. Knoll, *Radiation Detection and Measurement*, vol. 1, 3rd ed: Wiley; 3 edition (January 5, 2000), 2000.

[51] S. Derenzo, H. Zaklad, and T. Budinger, "Analytical study of a high-resolution positron ring detector system for transaxial reconstruction tomography," *Journal of Nuclear Medicine*, vol. 16, pp. 1166-1173, 1975.

[52] S. Derenzo, W. Moses, R. Huesman, and T. Budinger, *Critical instrumentation issues for <2 mm resolution, high sensitivity brain PET*, vol. 1993. Amsterdam, the Netherlands: Elsevier Science Publishers, 1993.

[53] S. E. Derenzo, "Precision measurement of annihilation point spread distributions for medically important positron emitters," *Positron Annihilation*, pp. 819–23, 1979.

[54] M. Schmand, L. Eriksson, M. E. Casey, K. Wienhard, G. Flugge, R. Nutt, C. T. I. P. E. T. S. Inc, and T. N. Knoxville, "Advantages using pulse shape discrimination to assign the depth ofinteraction information (DOI) from a multi layer phoswich detector," *IEEE Transactions on Nuclear Science*, vol. 46, pp. 985–990, 1999.

[55] S. R. Cherry, J. A. Sorenson, and M. E. Phelps, *Physics in Nuclear Medicine*, 3 ed: Elsevier Science, 2003.

[56] A. M. Alessio, P. E. Kinahan, and T. K. Lewellen, "Modeling and incorporation of system response functions in 3-D whole body PET," *Medical Imaging, IEEE Transactions on*, vol. 25, pp. 828-837, 2006.

[57] J. R. Stickel and S. R. Cherry, "High-resolution PET detector design: modelling components of intrinsic spatial resolution," *Physics in Medicine and Biology*, vol. 50, pp. 179-195, 2005.

[58] C. S. Levin and H. Zaidi, "Current trends in preclinical PET system design."

[59] F. C. Arion, "Molecular imaging of small animals with dedicated PET tomographs," *European Journal of Nuclear Medicine and Molecular Imaging*, vol. 29, pp. 98-114 %U http://dx.doi.org/10.1007/s00259-001-0683-3, 2002.

[60] A. Del Guerra, G. Di Domenico, M. Scandola, G. Zavattini, D. di Fisica, and F. Infn, "YAP-PET: a small animal positron emission tomograph based on YAP: Cefinger crystals," in *IEEE Nuclear Science Symposium, 1997*, 1997.

[61] D. P. McElroy, W. Pimpl, B. J. Pichler, M. Rafecas, T. Schuler, and S. I. Ziegler, "Characterization and readout of MADPET-II detector modules: validation of a unique design concept for high resolution small animal PET," *IEEE Transactions on Nuclear Science*, vol. 52, pp. 199–204, 2005.

[62] K. Ziemons, E. Auffray, R. Barbier, G. Brandenburg, P. Bruyndonckx, Y. Choi, D. Christ, N. Costes, Y. Declais, O. Devroede, and others, "The ClearPET™ project: development of a 2nd generation high-performance small animal PET scanner," *Nuclear Inst. and Methods in Physics Research, A*, vol. 537, pp. 307–311, 2005.

[63] S. Surti, J. S. Karp, A. E. Perkins, C. A. Cardi, M. E. Daube-Witherspoon, A. Kuhn, and G. Muehllehner, "Imaging performance of A-PET: a small animal PET camera," *IEEE transactions on medical imaging*, vol. 24, pp. 844–852, 2005.

[64] J. Missimer, Z. Madi, M. Honer, C. Keller, A. Schubiger, and S. M. Ametamey, "Performance evaluation of the 16-module quad-HIDAC small animal PET camera," *Physics in Medicine and Biology*, vol. 49, pp. 2069–2081, 2004.

[65] Y. Yang, Y.-C. Tai, S. Siegel, D. F. Newport, B. Bai, Q. Li, R. M. Leahy, and S. R. Cherry, "Optimization and performance evaluation of the microPET II scanner for in vivo small-animal imaging," *Physics in Medicine and Biology*, vol. 49, pp. 2527-2545, 2004.

[66] S. R. Cherry, Y. Shao, R. W. Silverman, K. Meadors, S. Siegel, A. Chatziioannou, J. W. Young, W. Jones, J. C. Moyers, D. Newport, and others, "MicroPET: a high resolution PET scanner for imaging small animals," *IEEE Transactions on Nuclear Science*, vol. 44, pp. 1161–1166, 1997.

[67] E. P. Visser, J. A. Disselhorst, M. Brom, P. Laverman, M. Gotthardt, W. J. G. Oyen, and O. C. Boerman, "Spatial Resolution and Sensitivity of the Inveon Small-Animal PET Scanner," *J Nucl Med*, vol. 50, pp. 139-147, 2009.

[68] Y. Wang, J. Seidel, B. M. W. Tsui, J. J. Vaquero, and M. G. Pomper, "Performance evaluation of the GE healthcare eXplore VISTA dual-ring small-animal PET scanner," *Journal of Nuclear Medicine*, vol. 47, pp. 1891, 2006.

[69] X. Shuping, R. Ramirez, L. Yaqiang, X. Tao, J. Uribe, L. Hongdi, W. Yu, H. Baghaei, K. Soonseok, and W. Wai-Hoi, "A pentagon photomultiplier-quadrant-sharing BGO detector for a rodent research PET (RRPET)," *Nuclear Science, IEEE Transactions on*, vol. 52, pp. 210-216, 2005.

[70] J. Uribe, H. Baghaei, H. Li, S. Yokoyama, N. Zhang, J. Wang, F. R. Dobbs, and W. H. Wang, "Basic imaging performance characteristics of a variable field ofview PET camera using quadrant sharing detector design," *IEEE Transactions on Nuclear Science*, vol. 46, pp. 491–497, 1999.

[71] P. Bérard, M. Bergeron, C. M. Pepin, J. Cadorette, M.-A. Tétrault, N. Viscogliosi, R. Fontaine, H. Dautet, M. Davies, P. Deschamps, and R. Lecomte, "Development of a 64-channel APD detector module with individual pixel readout for submillimetre spatial resolution in PET," *Nuclear Instruments and Methods in Physics Research Section A: Accelerators, Spectrometers, Detectors and Associated Equipment*, vol. 610, pp. 20-23 %U http://www.sciencedirect.com/science/article/B6TJM-4WB3N75-M/2/a0e5a08d449dd208376ec801bbadc41a, 2009.

[72] M. Bergeron, J. Cadorette, J. F. Beaudoin, M. D. Lepage, G. Robert, V. Selivanov, M. A. Tetrault, N. Viscogliosi, J. P. Norenberg, R. Fontaine, and R. Lecomte, "Performance Evaluation of the LabPET APD-Based Digital PET Scanner," *Nuclear Science, IEEE Transactions on*, vol. 56, pp. 10-16, 2009.

[73] S. Shokouhi, P. Vaska, S. Southekal, D. Schlyer, M. Purschke, V. Dzordzhadze, C. Woody, S. Stoll, D. L. Alexoff, and D. Rubins, "Statistical 3D image reconstruction for the RatCAP PET tomograph using a physically accurate, Monte Carlo based system matrix," in *2004 IEEE Nuclear Science Symposium Conference Record*, 2004.

[74] M. Rafecas, G. Boning, B. J. Pichler, E. Lorenz, M. Schwaiger, and S. I. Ziegler, "A Monte Carlo study of high-resolution PET with granulated dual-layer detectors," *Nuclear Science, IEEE Transactions on*, vol. 48, pp. 1490-1495, 2001.

[75] J. S. Huber and W. W. Moses, "Conceptual design of a high-sensitivity small animal PET camera with 4π coverage," *Nuclear Science, IEEE Transactions on*, vol. 46, pp. 498-502, 1999.

[76] J. W. Beck, R. J. Jaszczak, R. E. Coleman, C. F. Starmer, and L. W. Nolte, "Analysis of SPECT including Scatter and Attenuation Using Sophisticated Monte Carlo Modeling Methods," *Nuclear Science, IEEE Transactions on*, vol. 29, pp. 506-511, 1982.

[77] C. S. Levin, A. M. K. Foudray, and F. Habte, "Impact of high energy resolution detectors on the performance of a PET system dedicated to breast cancer imaging," *Physica Medica*, vol. 21, pp. 28-34 %U http://www.sciencedirect.com/science/article/B8G3S-4P8SCVM-D/2/76ac797184fa9aacf06a2a918c08b9df, 2006.

[78] C. Levin, M. Dahlbom, and E. Hoffman, "A Monte Carlo correction for the effect of Compton scattering in 3D PET brain imaging," *IEEE Trans Nuc Sci*, vol. 42, pp. 1181-1185, 1995.

[79] S. Staelens and I. Lemahieu, "Monte Carlo Based Image Reconstruction in Emission Tom ography," *Computational Intelligence in Medical Imaging: Techniques and Applications*, pp. 407, 2009.

[80] G. Boning, B. J. Pichler, M. Rafecas, E. Lorenz, M. Schwaiger, and S. I. Ziegler, *Implementation of Monte Carlo coincident aperture functions in image generation of a high-resolution animal positron tomograph*, 2001.

[81] M. A. Kropholler, R. Boellaard, A. Schuitemaker, B. N. M. van Berckel, G. Luurtsema, A. D. Windhorst, and A. A. Lammertsma, "Development of a tracer kinetic plasma input model for (R)-[11C] PK11195 brain studies," *Journal of Cerebral Blood Flow & Metabolism*, vol. 25, pp. 842–851, 2005.

[82] G. P. Estes and W. M. Taylor, *Computational radiology and imaging with the MCNP Monte Carlo code*, 1995.

[83] J. Allison, K. Amako, J. Apostolakis, H. Araujo, P. A. Dubois, M. Asai, G. Barrand, R. Capra, S. Chauvie, R. Chytracek, G. A. P. Cirrone, G. Cooperman, G. Cosmo, G. Cuttone, G. G. Daquino, M. Donszelmann, M. Dressel, G. Folger, F. Foppiano, J. Generowicz, V. Grichine, S. Guatelli, P. Gumplinger, A. Heikkinen, I. Hrivnacova, A. Howard, S. Incerti, V. Ivanchenko, T. Johnson, F. Jones, T. Koi, R. Kokoulin, M. Kossov, H. Kurashige, V. Lara, S. Larsson, F. Lei, O. Link, F. Longo, M. Maire, A. Mantero, B. Mascialino, I. McLaren, P. M. Lorenzo, K. Minamimoto, K. Murakami, P. Nieminen, L. Pandola, S. Parlati, L. Peralta, J. Perl, A. Pfeiffer, M. G. Pia, A. Ribon, P. Rodrigues, G. Russo, S. Sadilov, G. Santin, T. Sasaki, D. Smith, N. Starkov, S. Tanaka, E. Tcherniaev, B. Tome, A. Trindade, P. Truscott, L. Urban, M. Verderi, A. Walkden, J. P. Wellisch, D. C. Williams, D. Wright, and H. Yoshida, "Geant4 developments and applications," *Nuclear Science, IEEE Transactions on*, vol. 53, pp. 270-278, 2006.

[84] R. L. H. T. K. Lewellen, and S. Vannoy *The SimSET program*. Bristol, UK: Inst. Physics, 1998.

[85] S. Jan, G. Santin, D. Strul, S. Staelens, K. Assie, D. Autret, S. Avner, R. Barbier, M. Bardies, P. M. Bloomfield, D. Brasse, V. Breton, P. Bruyndonckx, I. Buvat, A. F. Chatziioannou, Y. Choi, Y. H. Chung, C. Comtat, D. Donnarieix, L. Ferrer, S. J. Glick, C. J. Groiselle, D. Guez, P. F. Honore, S. Kerhoas-Cavata, A. S. Kirov, V. Kohli, M. Koole, M. Krieguer, D. J. v. d. Laan, F. Lamare, G. Largeron, C. Lartizien, D. Lazaro, M. C. Maas,

L. Maigne, F. Mayet, F. Melot, C. Merheb, E. Pennacchio, J. Perez, U. Pietrzyk, F. R. Rannou, M. Rey, D. R. Schaart, C. R. Schmidtlein, L. Simon, T. Y. Song, J. M. Vieira, D. Visvikis, R. V. d. Walle, E. Wieers, and C. Morel, "GATE: a simulation toolkit for PET and SPECT," *Physics in Medicine and Biology*, vol. 49, pp. 4543-4561, 2004.

[86] R. H. Huesman, G. J. Klein, W. W. Moses, J. Qi, B. W. Reutter, and P. R. G. Virador, "List-mode maximum-likelihood reconstruction applied to positron emission mammography(PEM) with irregular sampling," *IEEE transactions on medical imaging*, vol. 19, pp. 532–537, 2000.

[87] T. E. Nichols, J. Qi, E. Asma, and R. M. Leahy, "Spatiotemporal reconstruction of list mode PET data," *IEEE Trans. Med. Imaging*, vol. 21, pp. 396–404, 2002.

[88] L. Parra and H. H. Barrett, "List-mode likelihood: EM algorithm and image quality estimation demonstrated on 2-D PET," *IEEE transactions on medical imaging*, vol. 17, pp. 228–235, 1998.

[89] F. Fahey, "Data Acquisition in PET Imaging," PET Center, Wake Forest University School of Medicine, Winston-Salem, North Carolina.

[90] R. A. Brooks, V. J. Sank, A. J. Talbert, and G. Di Chiro, "Sampling requirements and detector motion for positron emission tomography," *IEEE Transactions on Nuclear Science*, vol. 26, pp. 2760–2763, 1979.

[91] Y. C. Tai, A. Ruangma, D. Rowland, S. Siegel, D. F. Newport, P. L. Chow, and R. Laforest, "Performance evaluation of the microPET focus: a third-generation microPET scanner dedicated to animal imaging," *Journal of Nuclear Medicine*, vol. 46, pp. 455, 2005.

[92] E. Asma, D. W. Shattuck, and R. M. Leahy, "Lossless compression of list-mode 3D PET data," *Complexity*, vol. 1010, pp. 1011.

[93] K. Wienhard, M. Schmand, M. E. Casey, K. Baker, J. Bao, L. Eriksson, W. F. Jones, C. Knoess, M. Lenox, M. Lercher, P. Luk, C. Michel, J. H. Reed, N. Richerzhagen, J. Treffert, S. Vollmar, J. W. Young, W. D. Heiss, and R. Nutt, "The ECAT HRRT: performance and first clinical application of the new high resolution research tomograph," in *Nuclear Science Symposium Conference Record, 2000 IEEE*, 2000.

[94] M. E. Daube-Witherspoon and G. Muehllehner, "Treatment of Axial Data in Three-Dimensional PET," *J Nucl Med*, vol. 28, pp. 1717-1724, 1987.

[95] R. M. Lewitt, G. Muehllehner, and J. S. Karp, "Three-dimensional image reconstruction for PET by multi-slice rebinning and axial image filtering," *Physics in Medicine and Biology*, vol. 39, pp. 321-339, 1994.

[96] M. Defrise, "A factorization method for the 3D X-ray transform," *Inverse Problems*, vol. 11, pp. 983–983, 1995.

[97] S. Matej, J. S. Karp, R. M. Lewitt, and A. J. Becher, "Performance of the Fourier rebinning algorithm for PET with large acceptance angles," *Physics in medicine & biology(Print)*, vol. 43, pp. 787–795, 1998.

[98] M. E. Daube-Witherspoon, S. Matej, J. S. Karp, and R. M. Lewitt, "Application of the row action maximum likelihood algorithm withspherical basis functions to clinical PET imaging," *IEEE Transactions on Nuclear Science*, vol. 48, pp. 24–30, 2001.

[99] C. W. Stearns and J. A. Fessler, "3D PET reconstruction with FORE and WLS-OS-EM," in *Proc. IEEE Nuc. Sci. Symp. Med. Im. Conf*, 2002.

[100] H. Stark, J. Woods, I. Paul, and R. Hingorani, "Direct Fourier reconstruction in computer tomography," *Acoustics, Speech and Signal Processing, IEEE Transactions on*, vol. 29, pp. 237-245, 1981.

[101] H. Baghaei, W. H. Wong, H. Li, J. Uribe, Y. Wang, M. Aykac, Y. Liu, and T. Xing, "Evaluation of filter function for volume PET imaging using the 3DRP algorithm," in *2001 IEEE Nuclear Science Symposium Conference Record*, vol. 3, 2001.

[102] C. Labbe, H. Zaidi, C. Morel, and K. Thielemans, "The STIR implementation of FBP 3DRP %U stir.sourceforge.net/documentation/STIR-FBP3DRP.pdf."

[103] P. E. Kinahan and J. G. Rogers, "Analytic 3D image reconstruction using all detected events," *Nuclear Science, IEEE Transactions on*, vol. 36, pp. 964-968, 1989.

[104] M. Defrise, P. E. Kinahan, D. W. Townsend, C. Michel, M. Sibomana, and D. F. Newport, "Exact and approximate rebinning algorithms for 3-D PET data," *Medical Imaging, IEEE Transactions on*, vol. 16, pp. 145-158, 1997.

[105] H. Zaidi, "Comparative evaluation of scatter correction techniques in 3D positron emission tomography," *European Journal of Nuclear Medicine and Molecular Imaging*, vol. 27, pp. 1813-1826, 2000.

[106] R. Gordon, R. Bender, and G. T. Herman, "Algebraic reconstruction techniques (ART) for three-dimensional electron microscopy and x-ray photography," *Journal of theoretical Biology*, vol. 29, pp. 471, 1970.

[107] L. Shepp and Y. Vardi, "Maximum Likelihood Reconstruction in Positron Emission Tomography," *IEEE Trans Med Imaging*, vol. 1, pp. 113-122, 1982.

[108] K. Lange and R. Carson, "EM reconstruction algorithms for emission and transmission tomography," *Journal of Computer Assisted Tomography*, vol. 8, pp. 306-316 %U http://www.ncbi.nlm.nih.gov/pubmed/6608535, 1984.

[109] S. Matej and R. M. Lewitt, "Practical considerations for 3-D image reconstruction using spherically symmetric volume elements," *Medical Imaging, IEEE Transactions on*, vol. 15, pp. 68-78, 1996.

[110] H. Yu-Lung, G. T. Gullberg, G. L. Zeng, and R. H. Huesman, "Image reconstruction using a generalized natural pixel basis," *Nuclear Science, IEEE Transactions on*, vol. 43, pp. 2306-2319, 1996.

[111] T. Frese, N. C. Rouze, C. A. Bouman, K. Sauer, and G. D. Hutchins, "Quantitative comparison of FBP, EM, and Bayesian reconstruction algorithms, including the impact of accurate system modeling, for the IndyPET scanner," in *Nuclear Science Symposium Conference Record, 2001 IEEE*, 2001.

[112] E. Asma, T. E. Nichols, Q. Jinyi, and R. M. Leahy, "4D PET image reconstruction from list mode data," in *Nuclear Science Symposium Conference Record, 2000 IEEE*, 2000.

[113] T. E. Nichols, Q. Jinyi, E. Asma, and R. M. Leahy, "Spatiotemporal reconstruction of list-mode PET data," *Medical Imaging, IEEE Transactions on*, vol. 21, pp. 396-404, 2002.

[114] A. J. Reader, F. C. Sureau, C. Comtat, R. Trébossen, and I. Buvat, "Joint estimation of dynamic PET images and temporal basis functions using fully 4D ML-EM," *Physics in Medicine and Biology*, vol. 51, pp. 5455–5474, 2006.

[115] C. A. Johnson, Y. Yuchen, R. E. Carson, R. L. Martino, and M. E. Daube-Witherspoon, "A system for the 3D reconstruction of retracted-septa PET data using the EM algorithm," *Nuclear Science, IEEE Transactions on*, vol. 42, pp. 1223-1227, 1995.

[116] R. L. Siddon, "Fast calculation of the exact radiological path for a three-dimensional CT array," *Medical Physics*, vol. 12, pp. 252-255, 1985.

[117] J. M. Ollinger and A. S. Goggin, "Maximum likelihood reconstruction in fully 3D PET via the SAGE algorithm," in *Nuclear Science Symposium, 1996. Conference Record., 1996 IEEE*, 1996.

[118] J. Qi, R. M. Leahy, S. R. Cherry, A. Chatziioannou, and T. H. Farquhar, "High-resolution 3D Bayesian image reconstruction using the microPET small-animal scanner," *Phys. Med. Biol*, vol. 43, pp. 1001 1013, 1998.

[119] E. Ü. Mumcuoglu, R. M. Leahy, and S. R. Cherry, "Bayesian reconstruction of PET images: methodology and performance analysis," *Physics in Medicine and Biology*, vol. 41, pp. 1777-1807, 1996.

[120] V. Y. Panin, F. Kehren, C. Michel, and M. Casey, "Fully 3-D PET reconstruction with system matrix derived from point source measurements," *Medical Imaging, IEEE Transactions on*, vol. 25, pp. 907-921, 2006.

[121] S. Shokouhi, P. Vaska, D. J. Schlyer, S. P. Stoll, A. Villanueva Jr, A. Kriplani, and C. L. Woody, "System performance simulations of the RatCAP awake rat brain scanner," *IEEE Transactions on Nuclear Science*, vol. 52, pp. 1305-1310, 2005.

[122] S. Southekal, M. Purschke, D. Schlyer, C. Woody, and P. Vaska, "Quantitative PET Imaging Using a Comprehensive Monte Carlo System Model," *Phys Med Biol*, vol. submitted, 2009.

[123] M. Rafecas, B. Mosler, M. Dietz, M. Pogl, A. Stamatakis, D. P. McElroy, and S. I. Ziegler, "Use of a Monte Carlo-based probability matrix for 3-D iterative reconstruction of MADPET-II data," *Nuclear Science, IEEE Transactions on*, vol. 51, pp. 2597-2605, 2004.

[124] S. S. Southekal, M. Purschke, S. J. Park, S. S. Junnarkar, J. F. Pratte, S. P. Stoll, D. J. Schlyer, C. L. Woody, and P. Vaska, "Quantitative Image Reconstruction for the RatCAP PET Tomograph," in *IEEE Nuclear Science Symposium Conference Record, 2006*, vol. 5, 2006.

[125] H. Barrett, D. Wilson, and B. Tsui, "Noise properties of the EM algorithm. I. Theory," *Phys Med Biol*, vol. 39, pp. 833-846, 1994.

[126] J. A. Fessler and L. W. Rogers, "Spatial Resolution Properties of Penalized-Likelihood Methods Image Reconstruction: Space Invariant Tomographs," *IEEE Trans Img Process*, vol. 5, pp. 1346-1358, 1996.

[127] G. Gindi, M. Lee, A. Rangarajan, and I. G. Zubal, "Bayesian reconstruction of functional images using anatomical information as priors," *Medical Imaging, IEEE Transactions on*, vol. 12, pp. 670-680, 1993.

[128] J. Nuyts and J. A. Fessler, "A penalized-likelihood image reconstruction method for emission tomography, compared to postsmoothed maximum-likelihood with matched spatial resolution," *IEEE Trans Med Imaging*, vol. 22, pp. 1042-52, 2003.

[129] J. A. Fessler, "Penalized weighted least-squares image reconstruction for positron emission tomography," *Medical Imaging, IEEE Transactions on*, vol. 13, pp. 290-300, 1994.

[130] J. Beutel, M. Sonka, and J. M. Fitzpatrick, *Handbook of medical imaging*: SPIE Press, 2000.

[131] R. M. Leahy and J. Qi, "Statistical approaches in quantitative positron emission tomography," *Statistics and Computing*, vol. 10, pp. 147–165, 2000.

[132] J. Qi and R. M. Leahy, "Iterative reconstruction techniques in emission computed tomography," *Phys. Med. Biol*, vol. 51, pp. R541 R578, 2006.

[133] H. M. Hudson and R. S. Larkin, "Accelerated image reconstruction using ordered subsets of projection data," *IEEE Transactions on Medical Imaging*, vol. 13, pp. 601 609, 1994.

[134] I. T. Hsiao, A. Rangarajan, P. Khurd, and G. Gindi, "An accelerated convergent ordered subsets algorithm for emission tomography," *Physics in Medicine and Biology*, vol. 49, pp. 2145–2156, 2004.

[135] S. Ahn and J. A. Fessler, "Globally convergent image reconstruction for emission tomography using relaxed ordered subsets algorithms," *IEEE Trans Med Imaging*, vol. 22, pp. 613-26, 2003.

[136] D. Wilson, B. Tsui, and H. Barrett, "Noise properties of the EM algorithm. II. Monte Carlo Simulations," *Phys Med Biol*, vol. 39, pp. 847-871, 1994.

[137] V. Johnson, "A Note on Stopping Rules in EM-ML Reconstructions of ECT Images," *IEEE TRANS. MED. IMAG., CORRESPONDENCE*, vol. 13, pp. 569–571 %U http://citeseerx.ist.psu.edu/viewdoc/summary?doi=10.1.1.30.7899, 1994.

[138] D. L. Snyder and M. I. Miller, "The Use of Sieves to Stabilize Images Produced with the EM Algorithm for Emission Tomography," *Nuclear Science, IEEE Transactions on*, vol. 32, pp. 3864-3872, 1985.

[139] M. Jacobson, R. Levkovitz, A. Ben-Tal, K. Thielemans, T. Spinks, D. Belluzzo, E. Pagani, V. Bettinardi, M. C. Gilardi, A. Zverovich, and others, "Enhanced 3D PET OSEM reconstruction using inter-update Metz filtering," *Physics in Medicine and Biology*, vol. 45, pp. 2417 2439, 2000.

[140] J. A. Fessler and A. O. Hero, "Penalized maximum-likelihood image reconstruction using space-alternating generalized EM algorithms," *IEEE Transactions on Image Processing*, vol. 4, pp. 1417-1429 %U http://adsabs.harvard.edu/abs/1995ITIP....4.1417F, 1995.

[141] J. W. Stayman and J. A. Fessler, "Regularization for uniform spatial resolution properties in penalized-likelihood image reconstruction," *Medical Imaging, IEEE Transactions on*, vol. 19, pp. 601-615, 2000.

[142] R. Myers, "The biological application of small animal PET imaging," *Nuclear medicine and biology*, vol. 28, pp. 585 593, 2001.

[143] S. P. Hume, A. A. Lammertsma, R. Myers, S. Rajeswaran, P. M. Bloomfield, S. Ashworth, R. A. Fricker, E. M. Torres, I. Watson, and T. Jones, "The potential of high-resolution positron emission tomography to monitor striatal dopaminergic function in rat models of disease," *Journal of neuroscience methods*, vol. 67, pp. 103 112, 1996.

[144] S. Surti, A. Kuhn, M. E. Werner, A. E. Perkins, J. Kolthammer, and J. S. Karp, "Performance of Philips Gemini TF PET/CT scanner with special consideration for its time-of-flight imaging capabilities," *Journal of Nuclear Medicine*, vol. 48, pp. 471, 2007.

[145] M. Conti, B. Bendriem, M. Casey, M. Chen, F. Kehren, C. Michel, and V. Panin, "First experimental results of time-of-flight reconstruction on an LSO PET scanner," *Physics in Medicine and Biology*, vol. 50, pp. 4507–4526, 2005.

[146] A. Kuhn, S. Surti, J. S. Karp, P. S. Raby, K. S. Shah, A. E. Perkins, and G. Muehllehner, "Design of a lanthanum bromide detector for time-of-flight PET," *IEEE Transactions on Nuclear Science*, vol. 51, pp. 2550–2557, 2004.

[147] W. H. Wong, N. A. Mullani, E. A. Philippe, R. Hartz, and K. L. Gould, *Image improvement and design optimization of the time-of-flight PET*, vol. 24: Soc Nuclear Med, 1983.

[148] J. S. Karp, G. Muehllehner, D. A. Mankoff, C. E. Ordonez, J. M. Ollinger, M. E. Daube-Witherspoon, A. T. Haigh, and D. J. Beerbohm, "Continuous-Slice PENN-PET: A Positron Tomograph with Volume Imaging Capability," *J Nucl Med*, vol. 31, pp. 617-627, 1990.

[149] R. D. Badawi, M. P. Miller, D. L. Bailey, and P. K. Marsden, "Randoms variance reduction in 3D PET," *Physics in Medicine and Biology*, vol. 44, pp. 941-954 %U http://www.iop.org/EJ/abstract/0031-9155/44/4/010/, 1999.

[150] M. E. Casey and E. J. Hoffman, "Quantitation in positron emission computed tomography: 7. A technique to reduce noise in accidental coincidence measurements and coincidence efficiency calibration," *Journal of Computer Assisted Tomography*, vol. 10, pp. 845-850 %U http://www.ncbi.nlm.nih.gov/pubmed/3489018, 1986.

[151] D. Brasse, P. E. Kinahan, C. Lartizien, C. Comtat, M. Casey, and C. Michel, "Correction Methods for Random Coincidences in Fully 3D Whole-Body PET: Impact on Data and Image Quality," *J Nucl Med*, vol. 46, pp. 859-867, 2005.

[152] M. Yavuz and J. A. Fessler, "Statistical image reconstruction methods for randoms-precorrected PET scans," *Med Image Anal*, vol. 2, pp. 369-78, 1998.

[153] D. G. Politte and D. L. Snyder, "Corrections for accidental coincidences and attenuation in maximum-likelihood image reconstruction for positron-emission tomography," *Medical Imaging, IEEE Transactions on*, vol. 10, pp. 82-89, 1991.

[154] O. Okitta, M. Casey, K. Weinhard, and U. Pietrzyk, "Random Correction for Positron Emission Tomography using Singles Count Rates," presented at Nuclear Science Symposium, IEEE, Lyon, France, 2000.

[155] H. Zaidi and K. F. Koral, "Scatter modelling and compensation in emission tomography," *European Journal of Nuclear Medicine and Molecular Imaging*, vol. 31, pp. 761-782, 2004.

[156] S. R. Cherry and S. C. Huang, "Effects of scatter on model parameter estimates in 3D PET studiesof the human brain," *IEEE Transactions on Nuclear Science*, vol. 42, pp. 1174–1179, 1995.

[157] M. A. King, G. J. Hademenos, and S. J. Glick, *A dual-photopeak window method for scatter correction*, vol. 33: Soc Nuclear Med, 1992.

[158] S. Grootoonk, T. J. Spinks, D. Sashin, N. M. Spyrou, and T. Jones, "Correction for scatter in 3D brain PET using a dual energy window method," *Physics in Medicine and Biology*, vol. 41, pp. 2757–2774, 1996.

[159] L. Shao, R. Freifelder, and J. S. Karp, "Triple energy window scatter correction technique in PET," *IEEE transactions on medical imaging*, vol. 13, pp. 641 648, 1994.

[160] C. J. Thompson, "The problem of scatter correction in positron volume imaging," *IEEE transactions on medical imaging*, vol. 12, pp. 124–132, 1993.

[161] B. Bendriem, R. Trebossen, V. Frouin, and A. Syrota, "A PET scatter correction using simultaneous acquisitions with low and high lower energy thresholds," in *Nuclear Science Symposium and Medical Imaging Conference, 1993., 1993 IEEE Conference Record.*, 1993.

[162] M. Bentourkia, P. Msaki, J. Cadorette, and R. Lecomte, "Energy dependence of scatter components in multispectral PETimaging," *IEEE transactions on medical imaging*, vol. 14, pp. 138–145, 1995.

[163] M. Bergström, L. Eriksson, C. Bohm, G. Blomqvist, and J. Litton, "Correction for scattered radiation in a ring detector positron camera by integral transformation of the projections," *Journal of Computer Assisted Tomography*, vol. 7, pp. 42-50, 1983.

[164] L. Shao and J. S. Karp, "Cross-plane scattering correction-point source deconvolution in PET," *Medical Imaging, IEEE Transactions on*, vol. 10, pp. 234-239, 1991.

[165] D. L. Bailey and S. R. Meikle, "A convolution-subtraction scatter correction method for 3D PET," *Physics in Medicine and Biology*, vol. 39, pp. 411-424 %U http://www.iop.org/EJ/abstract/0031-9155/39/3/009, 1994.

[166] C. H. Holdsworth, C. S. Levin, M. Janecek, M. Dahlbom, and E. J. Hoffman, "Performance analysis of an improved 3-D PET Monte Carlo simulation and scatter correction," *Nuclear Science, IEEE Transactions on*, vol. 49, pp. 83-89, 2002.

[167] C. C. Watson, D. Newport, M. E. Casey, R. A. deKemp, R. S. Beanlands, and M. Schmand, "Evaluation of simulation-based scatter correction for 3-D PET cardiac imaging," *Nuclear Science, IEEE Transactions on*, vol. 44, pp. 90-97, 1997.

[168] O. Klein and Y. Nishina, "The scattering of light by free electrons according to Dirac's new relativistic dynamics," *Nature*, vol. 122, pp. 398–399, 1928.

[169] A. S. Goggin and J. M. Ollinger, "A model for multiple scatters in fully 3D PET Conf," in *Rec. 1994 IEEE Medical Imaging Conf.(Norfolk, 1994)*, 1995.

[170] J. S. Barney, J. G. Rogers, R. Harrop, H. Hoverath, and V. Triumf, "Object shape dependent scatter simulations for PET," *IEEE Transactions on Nuclear Science*, vol. 38, pp. 719–725, 1991.

[171] C. C. Watson, "New, faster, image-based scatter correction for 3D PET," in *Nuclear Science Symposium, 1999. Conference Record. 1999 IEEE*, vol. 3, 1999, pp. 1637-1641 vol.3.

[172] A. Werling, O. Bublitz, J. Doll, L. E. Adam, and G. Brix, "Fast implementation of the single scatter simulation algorithm and its use in iterative image reconstruction of PET data," *Physics in Medicine and Biology*, vol. 47, pp. 2947–2960, 2002.

[173] T. Yuan-Chuan and L. Richard, *INSTRUMENTATION ASPECTS OF ANIMAL PET*, 2005.

[174] P. Chow, F. Rannou, and A. Chatziioannou, "Attenuation correction for small animal PET tomographs," *Phys Med Biol*, vol. 50, pp. 13, 2005.

[175] R. A. deKemp and C. Nahmias, "Attenuation correction in PET using single photon transmission measurement," *Medical Physics*, vol. 21, pp. 771-778, 1994.

[176] P. E. Kinahan, D. W. Townsend, T. Beyer, and D. Sashin, "Attenuation correction for a combined 3D PET/CT scanner," *Medical Physics*, vol. 25, pp. 2046-2053 %U http://link.aip.org/link/?MPH/25/2046/1, 1998.

[177] R. Hustinx, R. J. Dolin, F. Bénard, A. Bhatnagar, D. Chakraborty, R. J. Smith, S. Jang, and A. Alavi, "Impact of attenuation correction on the accuracy of FDG-PET in patients with abdominal tumors: a free-response ROC analysis," *European Journal of Nuclear Medicine and Molecular Imaging*, vol. 27, pp. 1365-1371, 2000.

[178] S. C. Huang, E. J. Hoffman, M. E. Phelps, and D. E. Kuhl, "Quantitation in positron emission computed tomography: 2. Effects of inaccurate attenuation correction," *Journal of Computer Assisted Tomography*, vol. 3, pp. 804–hyhen, 1979.

[179] M. Dahlbom and E. J. Hoffman, "Problems in Signal-to-Noise Ratio for Attenuation Correction in High Resolution PET," *Nuclear Science, IEEE Transactions on*, vol. 34, pp. 288-293, 1987.

[180] L. R. Carroll, P. Kretz, and G. Orcutt, "The orbiting rod source: Improving performance in PET transmission correction scans," *Emission Computed Tomography: Current Trends, Esser, editor*, pp. 235–247.

[181] J. S. Karp, G. Muehllehner, H. Qu, and X. H. Yan, "Singles transmission in volume-imaging PET with a 137Cs source," *Physics in Medicine and Biology*, vol. 40, pp. 929–944, 1995.

[182] S. K. Yu and C. Nahmias, "Single-photon transmission measurements in positron tomography using 137Cs," *Physics in Medicine and Biology*, vol. 40, pp. 1255–1266, 1995.

[183] C. J. Thompson, N. Ranger, A. C. Evans, and A. Gjedde, *Validation of simultaneous PET emission and transmission scans*, vol. 32: Soc Nuclear Med, 1991.

[184] R. E. Carson, M. E. Daube-Witherspoon, and M. V. Green, *A method for postinjection PET transmission measurements with a rotating source*, vol. 29: Soc Nuclear Med, 1988.

[185] C. Riddell, P. Brigger, R. E. Carson, and S. L. Bacharach, "The watershed algorithm: a method to segment noisy PET transmission images," *IEEE Transactions on Nuclear Science*, vol. 46, pp. 713–719, 1999.

[186] V. Bettinardi, E. Pagani, M. C. Gilardi, C. Landoni, C. Riddell, G. Rizzo, I. Castiglioni, D. Belluzzo, G. Lucignani, S. Schubert, and others, "An automatic classification technique for attenuation correction in positron emission tomography," *European Journal of Nuclear Medicine and Molecular Imaging*, vol. 26, pp. 447–458, 1999.

[187] P. E. Kinahan, A. M. Alessio, and J. A. Fessler, "Dual energy CT attenuation correction methods for quantitative assessment of response to cancer therapy with PET/CT imaging," *Technology in Cancer Research and Treatment*, vol. 5, pp. 319, 2006.

[188] P. L. Chow, D. B. Stout, E. Komisopoulou, and A. F. Chatziioannou, "A method of image registration for small animal, multi-modality imaging," *Physics in Medicine and Biology*, vol. 51, pp. 379–390, 2006.

[189] K. L. Gould, T. Pan, C. Loghin, N. P. Johnson, A. Guha, and S. Sdringola, "Frequent Diagnostic Errors in Cardiac PET/CT Due to Misregistration of CT Attenuation and Emission PET Images: A Definitive Analysis of Causes, Consequences, and Corrections," *J Nucl Med*, vol. 48, pp. 1112-1121, 2007.

[190] H. Zaidi, M.-L. Montandon, and D. O. Slosman, "Magnetic resonance imaging-guided attenuation and scatter corrections in three-dimensional brain positron emission tomography," *Medical Physics*, vol. 30, pp. 937-948, 2003.

[191] M. E. Daube-Witherspoon and R. E. Carson, "Unified deadtime correction model for PET," *IEEE transactions on medical imaging*, vol. 10, pp. 267–275, 1991.

[192] S. Yamamoto, M. Amano, S. Miura, H. Iida, and I. Kanno, *Deadtime correction method using random coincidence for PET*, vol. 27: Soc Nuclear Med, 1986.

[193] M. Defrise, D. W. Townsend, D. Bailey, A. M. C. Geissbuhler, and T. Jones, "A normalization technique for 3D PET data," *Physics in Medicine and Biology*, vol. 36, pp. 939-952 %U http://www.iop.org/EJ/abstract/0031-9155/36/7/003, 1991.

[194] M. E. Casey, H. Gadagkar, and D. Newport, "A component based method for normalization in volume PET," in *3rd International Meeting on fully 3D Reconstruction in Nuclear Medicine and Radiology, Aix-les-Bains*, 1995, pp. 67 71.

[195] D. L. Bailey, D. W. Townsend, P. E. Kinahan, S. Grootoonk, and T. Jones, "An investigation of factors affecting detector and geometriccorrection in normalization of 3-D PET data," *IEEE Transactions on Nuclear Science*, vol. 43, pp. 3300–3307, 1996.

[196] P. E. Kinahan, D. W. Townsend, D. L. Bailey, D. Sashin, F. Jadali, and M. A. Mintun, "Efficiency normalization techniques for 3D PET data," in *1995 IEEE Nuclear Science Symposium and Medical Imaging Conference Record, 1995.*, 1995.

[197] J. S. Liow and S. C. Strother, "Normalization using rotating rods for 3D PET," in *Proc. 3rd Int. Meeting Fully Three-Dimensional Image Reconstruction in Radiology and Nuclear Medicine*.

[198] J. M. Ollinger, "Detector efficiency and Compton scatter in fully 3D PET," *IEEE Transactions on Nuclear Science*, vol. 42, pp. 1168–1173, 1995.

[199] E. J. Hoffman, T. M. Guerrero, G. Germano, W. M. Digby, and M. Dahlbom, "PET system calibrations and corrections for quantitative and spatially accurate images," *Nuclear Science, IEEE Transactions on*, vol. 36, pp. 1108-1112, 1989.

[200] W. Wang, Z. Hu, D. Gagnon, P. M. Syst, and H. Heights, "A new component approach to efficiency normalization for 3D PET," *IEEE Transactions on Nuclear Science*, vol. 54, pp. 92–99, 2007.

[201] E. P. Visser, J. A. Disselhorst, P. Laverman, M. Gotthardt, W. J. G. Oyen, and O. C. Boerman, "Contribution of normalization to image noise for the Siemens Inveon small-animal PET scanner," *Nuclear Instruments and Methods in Physics Research Section A: Accelerators, Spectrometers, Detectors and Associated Equipment*, vol. 605, pp. 433-435, 2009.

[202] B. Bai, Q. Li, C. H. Holdsworth, E. Asma, Y. C. Tai, A. Chatziioannou, and R. M. Leahy, "Model-based normalization for iterative 3D PET image reconstruction," *Physics in Medicine and Biology*, vol. 47, pp. 2773–2784, 2002.

[203] K. Thielemans, C. Morel, M. W. Jacobson, J. H. Kaempf, and S. Mustafovic, "Normalisation of Histogrammed List Mode Data," *Nuclear Science, IEEE Transactions on*, vol. 55, pp. 543-551, 2008.

[204] J. F. Pratte, S. Junnarkar, G. Deptuch, J. Fried, P. O'Connor, V. Radeka, P. Vaska, C. Woody, D. Schlyer, and S. Stoll, "The RatCAP front-end ASIC," in *IEEE Nuclear Science Symposium Conference Record, 2007. NSS'07*, vol. 1, 2007.

[205] S. S. Junnarkar, J. Fried, S. Southekal, J. F. Pratte, P. O'Connor, V. Radeka, P. Vaska, M. Purschke, D. Tomasi, C. Woody, and R. Fontaine, "Next Generation of Real Time Data Acquisition, Calibration and Control System for the RatCAP Scanner," *Nuclear Science, IEEE Transactions on*, vol. 55, pp. 220-224, 2008.

[206] S. S. Junnarkar, M. Purschke, J. F. Pratte, S. J. Park, P. O'Connor, and R. Fontaine, "An FPGA-based, 12-channel TDC and digital signal processing module for the RatCAP scanner," in *2005 IEEE Nuclear Science Symposium Conference Record*, vol. 2, 2005.

[207] S. Shokouhi, P. Vaska, S. Southekal, D. Schlyer, M. Purschke, V. Dzordzhadze, C. Woody, S. Stoll, D. L. Alexoff, and D. Rubins, "Statistical 3D image reconstruction for the RatCAP PET tomograph using a physically accurate, Monte Carlo based system matrix," in *2004 IEEE Nuclear Science Symposium Conference Record*, vol. 6, 2004.

[208] P. Vaska, S. P. Stoll, C. L. Woody, D. J. Schlyer, and S. Shokouhi, "Effects of intercrystal crosstalk on multielement LSO/APD PET detectors," *Nuclear Science, IEEE Transactions on*, vol. 50, pp. 362-366, 2003.

[209] C.-L. Chen, Y. Wang, J. J. S. Lee, and B. M. W. Tsui, "Integration of SimSET photon history generator in GATE for efficient Monte Carlo simulations of pinhole SPECT," *Medical Physics*, vol. 35, pp. 3278-3284, 2008.

[210] M. Shilov, E. Frey, P. Segars, J. Xu, and B. Tsui, "Improved Monte-Carlo simulations for dynamic PET," *J NUCL MED MEETING ABSTRACTS*, vol. 47, pp. 197P, 2006.

[211] P. Vaska, C. Woody, D. Schlyer, J. F. Pratte, S. Junnarkar, S. Southekal, S. Stoll, D. Schulz, W. Schiffer, and D. Alexoff, "The Design and Performance of the 2nd-Generation RatCAP Awake Brain PET System," in *Proc. IEEE Nuclear Science Symposium and Medical Imaging Conference, Honolulu*, 2007, pp. 4181 4184.

[212] S. J. Park, S. Southekal, M. Purschke, S. S. Junnarkar, J. F. Pratte, S. P. Stoll, C. L. Woody, D. J. Schlyer, and P. Vaska, "Digital coincidence processing for the RatCAP conscious rat brain PET scanner," *IEEE Transactions on Nuclear Science*, vol. 55, pp. 510-515, 2008.

[213] T. Küstner, J. Weidendorfer, J. Schirmer, T. Klug, C. Trinitis, and S. Ziegler, "Parallel MLEM on Multicore Architectures," in *Computational Science – ICCS 2009*, 2009, pp. 491-500.

[214] G. Pratx, G. Chinn, F. Habte, P. Olcott, and C. Levin, "Fully 3-D List-Mode OSEM Accelerated by Graphics Processing Units," in *Nuclear Science Symposium Conference Record, 2006. IEEE*, 2006.

[215] X. Fang and K. Mueller, "Accelerating popular tomographic reconstruction algorithms on commodity PC graphics hardware," *Nuclear Science, IEEE Transactions on*, vol. 52, pp. 654-663, 2005.

[216] D. Rubins, "Development of an anatomical atlas-based method for quantitative analysis of positron emission tomography (PET) images of the rat brain.," in *Biomedical Physics*, vol. PhD. Los Angeles: University of California, Los Angeles, CA, 2002.

[217] K. Ishiwata, N. Hayakawa, N. Ogi, K. Oda, H. Toyama, K. Endo, A. Tanaka, and M. Senda, "Comparison of three PET dopamine D2-like receptor ligands, [11C]raclopride, [11C]nemonapride and [11C]N-methylspiperone, in rats," *Annals of Nuclear Medicine*, vol. 13, pp. 161-167, 1999.

[218] F. R. Rannou and A. F. Chatziioannou, "Noise study in Monte Carlo estimated system matrix for OPET," in *IEEE Nuclear Science Symposium Conference Record, 2006*, 2006.

[219] J. Nuyts, "On Estimating the Variance of Smoothed MLEM Images," *IEEE Trans Nuc Sci*, vol. 49, pp. 714-721, 2002.

[220] "Performance Measurements for Small Animal Positron Emission Tomographs," NEMA Standards Publication NU4-2008 ed: National Electrical Manufacturers Association, 2008.

[221] R. Lecomte, "Technology challenges in small animal PET imaging," *Nuclear Instruments and Methods in Physics Research Section A: Accelerators, Spectrometers, Detectors and Associated Equipment*, vol. 527, pp. 157-165, 2004.

[222] C. Knoess, S. Siegel, A. Smith, D. Newport, N. Richerzhagen, A. Winkeler, A. Jacobs, R. N. Goble, R. Graf, K. Wienhard, and W.-D. Heiss, "Performance evaluation of the microPET R4 PET scanner for rodents," *European Journal of Nuclear Medicine and Molecular Imaging*, vol. 30, pp. 737-747, 2003.

[223] J. Logan, J. S. Fowler, N. D. Volkow, G. J. Wang, Y. S. Ding, and D. L. Alexoff, "Distribution volume ratios without blood sampling from graphical analysis of PET data," *Journal of Cerebral Blood Flow and Metabolism*, vol. 16, pp. 834–840, 1996.

[224] J. Logan, "Graphical analysis of PET data applied to reversible and irreversible tracers," *MED BIOL*, vol. 27, pp. 661–670, 2000.

[225] J. Logan, J. S. Fowler, N. D. Volkow, A. P. Wolf, S. L. Dewey, D. J. Schlyer, R. R. MacGregor, R. Hitzemann, B. Bendriem, and S. J. Gatley, "Graphical analysis of reversible radioligand binding from time-activity measurements applied to [N-11C-methyl]-⊚-cocaine PET studies in human subjects," *Journal of cerebral blood flow and metabolism: official journal of the International Society of Cerebral Blood Flow and Metabolism*, vol. 10, pp. 740, 1990.

[226] R. E. Carson, A. Breier, A. de Bartolomeis, R. C. Saunders, T. P. Su, B. Schmall, M. G. Der, D. Pickar, and W. C. Eckelman, "Quantification of Amphetamine-Induced Changes in [11C] Raclopride Binding with Continuous Infusion," *J Cereb Blood Flow Metab*, vol. 17, pp. 437-447 %U http://dx.doi.org/10.1097/00004647-199704000-00009, 1997.

[227] I. Buvat, "A non-parametric bootstrap approach for analysing the statistical properties of SPECT and PET images," *Physics in Medicine and Biology*, vol. 47, pp. 1761-1775 %U http://www.iop.org/EJ/abstract/0031-9155/47/10/311/, 2002.

[228] D. R. Haynor and S. D. Woods, "Resampling estimates of precision in emission tomography," *Medical Imaging, IEEE Transactions on*, vol. 8, pp. 337-343, 1989.

[229] M. Dahlbom, "Estimation of image noise in PET using the bootstrap method," *Nuclear Science, IEEE Transactions on*, vol. 49, pp. 2062-2066, 2002.

[230] E. Asma, T. E. Nichols, Q. Jinyi, and R. M. Leahy, "4D PET image reconstruction from list mode data," in *Nuclear Science Symposium Conference Record, 2000 IEEE*, vol. 2, 2000, pp. 15/57-15/65 vol.2.

[231] A. J. Reader, J. C. Matthews, F. C. Sureau, C. Comtat, R. Trebossen, and I. Buvat, "Iterative kinetic parameter estimation within fully 4D PET image reconstruction," in *IEEE Nuclear Science Symposium Conference Record, 2006*, vol. 3, 2006.